ANALYTICAL AND NUMERICAL MODELING OF CRYSTALLINE AND AMORPHOUS SILICON SOLAR CELLS AND ALLIED DEVICES

BY

KONSTANTINOS MISIAKOS

A DISSERTATION PRESENTED TO THE GRADUATE SCHOOL OF
THE UNIVERSITY OF FLORIDA IN
PARTIAL FULFILLMENT OF THE REQUIREMENTS
FOR THE DEGREE OF DOCTOR OF PHILOSOPHY

UNIVERSITY OF FLORIDA

1987

TO MY PARENTS

ACKNOWLEDGMENTS

I wish to express my gratitude to Professor Lindholm, chairman of my supervisory committee, for all his help, support and for his open mind in guiding this work. I would also like to extend my thanks to Professor Neugroschel, cochairman of my supervisory committee, for his help especially in the experimental part of this research.

I am indebted to Professors Peter T. Landsberg, Samuel B. Trickey and Sheng S. Li for serving in my supervisory committee and to Dr. Jong-Sik Park for helpful discussions.

The financial support of the Jet Propulsion Laboratory and the Solar Energy Research Institute is gratefully acknowledged.

TABLE OF CONTENTS

Page

ACKNOWLEDGMENTS......iii

ABSTRACT......vi

CHAPTER

ONE INTRODUCTION......1

TWO RECIPROCITY THEOREM AND SOLUTION OF THREE-DIMENSIONAL TRANSPORT PROBLEMS USING ONE-DIMENSIONAL MODELS

- 2.1 Introduction......4
- 2.2 Generalized Reciprocity Theorem for Semiconductor Devices......5
- 2.3 Exact Solution of Three-Dimensional Transport Problems Using One-Dimensional Models......11
  - 2.3.1 Solution of the Continuity Equation in Planar Symmetry Cases......13
  - 2.3.2 Photoluminescence Decay Response......16
  - 2.3.3 Transit Time and Transport Factor in Planar Devices......21
  - 2.3.4 Base Recombination Currents in Three-Dimensional Photovoltaic Devices......31
  - 2.3.5 Open-Circuit Voltage and Reciprocity Relation in Planar Photovoltaic Devices...... 33
  - 2.3.6 Arbitrary Boundaries...... 40
- 2.4 Conclusions......42

THREE SYSTEMATIC DESIGN THEORY FOR SILICON SOLAR CELLS USING OPTIMIZATION TECHNIQUES......43

- 3.1 Introduction......43
- 3.2 Lower Bounds of Dark Recombination Current in Quasi-Neutral Regions......44
- 3.3 Optimization of $R(x,R_s)$......54

3.4 Relation of the Present Model with the Transparent and Quasi-Equilibrium Models and Optimization of the Short-Circuit Current....66
3.5 Optimum Design....72
3.6 Concluding Remarks....81

FOUR LIFETIME AND DIFFUSIVITY DETERMINATION FROM FREQUENCY-DOMAIN TRANSIENT ANALYSIS....83

4.1 Introduction....83
4.2 Analytical Formulation....84
4.3 Demonstration of the Method and Discussion....86
4.4 Conclusions....93

FIVE NUMERICAL SOLUTIONS, PHYSICAL INTERPRETATIONS, AND ANALYTICAL MODELS FOR AMORPHOUS SILICON P/I/N SOLAR CELLS...95

5.1 Introduction....95
5.2 Numerical Modeling....96
5.3 Interpretation of the Numerical Results....102
5.4 Analytical Modeling....116
  5.4.1 Definition of Photocollected Currents....116
  5.4.2 Analytical Solutions for Strongly Absorbed light....121
  5.4.3 Analytical Solutions for Uniformly Absorbed light....123
5.5 Discussion and Critical Review of the Literature....128
5.6 Conclusions....132

SIX CRYSTALLINE VERSUS AMORPHOUS SILICON: PHYSICS AND MODELING....133

6.1 Introduction....133
6.2 Charge Transport in Crystalline and Amorphous Silicon Devices....134
6.3 Modeling Aspects of Crystalline and Amorphous Silicon Solar Cells....137
6.4 Conclusions....140

SEVEN SUMMARY....141

APPENDIX

A PROOF OF (3.18) AND (3.19)....144

B DERIVATION OF PHOTOCURRENT RELATIONS....146

C MINORITY-CARRIER ACCUMULATION AT THE BASE EDGE OF A JUNCTION SPACE-CHARGE REGION UNDER SHORT-CIRCUIT CONDITIONS....149

REFERENCES..155

BIOGRAPHICAL SKETCH...159

Abstract of Dissertation Presented to the Graduate School
of the University of Florida in Partial Fulfillment of the
Requirements for the Degree of Doctor of Philosophy

ANALYTICAL AND NUMERICAL MODELING OF CRYSTALLINE AND AMORPHOUS SILICON SOLAR CELLS AND ALLIED DEVICES

By

Konstantinos Misiakos

August 1987

Chairman: Fredrik A. Lindholm
Cochairman: Arnost Neugroschel
Major Department: Electrical Engineering

This work deals with the analytical and numerical modeling of two different types of solar cells: solar cells made of crystalline silicon and thin-film single-junction amorphous silicon solar cells. The modeling work on crystalline silicon solar cells is done by deriving optimum design principles for high conversion efficiency. Optimization of the performance through minimization of the recombination losses is emphasized. The effect of certain three-dimensional geometries on the operation of crystalline silicon solar cells, and other bipolar devices, is analyzed. A reciprocity theorem is presented that relates the current of the device under illumination with the normalized minority-carrier density under bias in the dark. In the same context, an experimental technique is described and demonstrated that allows measuring the minority-carrier lifetime and diffusivity in the base of a solar cell.

The modeling of amorphous silicon solar cells emphasizes the interpretation of numerical solutions for the device operating in the steady state under optical and terminal excitation. These solutions are obtained through a computer program that solves the Poisson and the current continuity equations. Based on this interpretation we propose an equivalent-circuit model for a-Si:H solar cells. This model clarifies the concept of the limiting carrier and enables derivation of analytical formulas for the cell photocurrent under strongly and weakly absorbed light.

Finally, we compare the physics and the modeling of crystalline and amorphous silicon solar cells focusing on transient experiments and on steady-state recombination.

CHAPTER ONE
INTRODUCTION

This dissertation mainly deals with the analytical and numerical modeling of crystalline and amorphous silicon solar cells, although some results are general enough for application to bipolar transistors, optical detectors and other allied devices. It consists of two parts. The first part, which treats crystalline silicon, develops optimized modeling and consequent design principles for high efficiency solar cells and emphasizes minimization of recombination losses. The first part also provides solutions for several three-dimensional transport problems in crystalline silicon that have implications for device characterization and that enable extension of the optimum design principles to three dimensional-solar cells. In addition, an experimental technique is presented and demonstrated that allows characterization of silicon solar cells by measuring the minority-carrier lifetime and diffusion coefficient in the principal region of the device.

The second part is on the modeling of thin film amorphous silicon (a-Si:H) p/i/n solar cells. To enable this modeling, a computer program is developed that solves numerically the complete system of Shockley equations. These solutions are treated as computer experiments designed to reveal the physical mechanisms controlling charge transport and quantum efficiency. Based on the physical interpretation of the numerical solutions we propose analytical models for the terminal current-voltage and photocurrent-voltage relations. Uniformly absorbed, strongly absorbed, and AM1.5 light are studied. The interdependencies among such internal variables as electric field, recombination rate, and carrier densities are discussed. A major point in the analysis of a-Si:H solar cells is the separation of currents into photogenerated and back-injected components. This separation clarifies the concept of the limiting carrier and helps in understanding the physical mechanisms constraining the quantum efficiency. It also enables the derivation of an equivalent-circuit model that qualitatively accounts for the dependence of internal variables on optical and terminal excitation. Finally, we compare the physics and modeling of single crystal and amorphous silicon solar cells. We discuss the differences in the physical mechanisms that control charge transport in the two devices and the applicability to amorphous silicon solar cells of concepts, like minority-carrier and low-level injection, borrowed from silicon devices.

The work that follows is presented in five chapters. Chapter two contains a reciprocity theorem and topics in three-dimensional transport in silicon devices. Chapter three is on the optimized modeling of silicon solar cells. In Chapter four a new experimental method is demonstrated that allows measuring minority-carrier lifetime and the diffusion coefficient in the base of a silicon solar cell. In Chapter five numerical and analytical results on a-Si:H solar cells are presented. In Chapter six we compare the physics and the modeling of crystalline silicon and amorphous silicon solar cells. Chapter seven summarizes the conclusions reached in this dissertation. Appendices treat particular problems arising in the development of the various chapters. Each chapter provides references to the literature of previous related work.

CHAPTER TWO
RECIPROCITY THEOREM AND SOLUTION OF THREE-DIMENSIONAL TRANSPORT PROBLEMS USING ONE-DIMENSIONAL MODELS

2.1 Introduction

This chapter shows that in certain three-dimensional devices a number of output parameters can be determined or related to the input without solving the actual boundary value problem. These results are derived by exploiting the symmetry of the structures involved as well as existing solutions for related one-dimensional problems. Several conclusions follow, regarding the modeling and the characterization of devices, which are three-dimensional either by construction (bipolar transistors, diodes) or by intention to improve performance (solar cells, detectors).

The work is presented in two sections. Section 2.2 presents a reciprocity theorem that allows calculation of the internal quantum efficiency of an illuminated p-n junction by using the solution of the transport equations of the same device in the dark. This theorem is used in Section 2.3 which treats transport in planar devices having mixed boundary conditions at one surface. The transit time and transport factor of shallow planar transistors and diodes are found to be the same as in their one-dimensional counterparts. With respect to solar cells and photodiodes we conclude that texturizing the cell surface to increase the effective absorbance leaves the base bulk recombination unchanged. Finally, partitioning the emitter to reduce its area and recombination losses results in the same open-circuit voltage as of the one-dimensional base-limited solar cell having the same base and a continuous emitter.

2.2 Generalized Reciprocity Theorem For Semiconductor Devices

Here we present a reciprocity theorem that relates the device short-circuit current induced by a carrier generation source to the minority-carrier quasi-Fermi level in the dark. This theorem is an extension of Donolato's [1] reciprocity relation for the photogenerated charge collection by a p-n junction. His proof was restricted to regions where only the lifetime was allowed to vary with position. We extend this proof to p-n junction devices having three-dimensional space dependencies of all material parameters. In addition, we prove that reciprocity holds also for transients and state another form of reciprocity relating quasi-Fermi levels and point generation in a quasineutral region under low injection conditions.

The conventional reciprocity theorem relating input voltages and output currents in the base of a transistor was proven by W. Shockley, M. Sparks and G. K. Teal [2] in one of the early papers on p-n junction transistors. Here we use Shockley's procedure and properly generalize in order to prove reciprocity for charge collection.

The principal quasineutral region of the diode, where carrier generation and recombination takes place, is bounded by the junction S_J and the rest of the surface S_L (lateral and back surface) characterized by a position dependent surface recombination velocity s'. The region is assumed to be p-type in low injection. Extension to n-type is straightforward. The space charge region edge S_J is assumed bias independent. Later in this section we will elaborate on the validity of this assumption. Two different excitation cases are considered. In case 1 the junction is forward biased by a voltage V in the dark. In case 2 the junction is short circuited and a point generation source of strength G is applied at point r'. If J, n and J',n' are the minority (electron) current density and excess minority carrier concentration for cases 1 and 2 respectively, then the boundary conditions for each case are

$$\frac{n(r_J)}{n_o(r_J)} = \exp(eV/kT)-1 , \qquad n'(r_J) = 0, \tag{2.1}$$

where $\mathbf{r}_J$ is a point on the junction edge S_J and n_o is the equilibrium minority-carrier concentration. The continuity equation for cases 1 and 2 is

$$-\frac{1}{e}\nabla\cdot J = -\frac{n}{\tau}, \qquad -\frac{1}{e}\nabla\cdot J' = -\frac{n'}{\tau} + G\delta(r-r'), \tag{2.2}$$

where $\delta(r - r')$ represents a unit point carrier generation source applied at $r = r'$, and τ is the lifetime. Because of low injection, the electric field E, the mobility μ and the lifetime τ are independent of the excitation. The system is linear.

Let vector **A** be defined by the equation

$$\mathbf{A} = \frac{n}{n_o} J' - \frac{n'}{n_o} J. \tag{2.3}$$

The surface integral $\int_{S_L} \mathbf{A}\cdot d\mathbf{s}$ vanishes since on S_L

$$\mathbf{A}\cdot d\mathbf{s} = -e(\frac{nn'}{n_o}\, s' - \frac{n'n}{n_o}\, s')|d\mathbf{s}| = 0. \tag{2.4}$$

From (2.1) this integral on S_J becomes

$$\int_{S_J} \mathbf{A}\cdot d\mathbf{s} = [\exp(eV/kT)-1] \int_{S_J} \mathbf{J}'\cdot d\mathbf{s} = [\exp(eV/kT)-1]\; I', \tag{2.5}$$

where I′ is the current due to the point source ecxiting the p-type region through the junction. Therefore, if S is the entire surface enclosing the quasineutral region, then from (2.4) and (2.5) the total surface integral of **A** becomes

$$\int_{S} \mathbf{A}\cdot d\mathbf{s} = \int_{S_L} \mathbf{A}\cdot d\mathbf{s} + \int_{S_J} \mathbf{A}\cdot d\mathbf{s} = [\exp(eV/kT)-1]\; I'. \tag{2.6}$$

By using (2.2), the Einstein relationship for non-degenerate minority carriers, $D = (kT/e)\mu$, and the expression for the electric field experienced by the minority carriers $\mathbf{E} = -(kT/e)\nabla \ln n_o$, the divergence of **A** can be written as

$$\nabla\cdot\mathbf{A} = \nabla\cdot(\frac{n}{n_o}\,\mathbf{J}') - \nabla\cdot(\frac{n'}{n_o}\,\mathbf{J}) =$$

$$\frac{1}{n_o}\,[\nabla n - n\nabla \ln n_o]\cdot\mathbf{J}' + \frac{n}{n_o}\,\nabla\cdot\mathbf{J}' - \frac{1}{n_o}\,[\nabla n' - n'\nabla \ln n_o]\cdot\mathbf{J} - \frac{n'}{n_o}\,\nabla\cdot\mathbf{J} =$$

$$\frac{1}{n_o}\,(\nabla n + \frac{e}{kT}\, n\mathbf{E})\cdot(e\mu n'\mathbf{E} + eD\nabla n') - e\frac{n}{n_o}\,(-\frac{n'}{\tau} + G\delta(\mathbf{r}-\mathbf{r}'))$$

$$-\frac{1}{n_o}\,(\nabla n' + \frac{e}{kT}\, n'\mathbf{E})\cdot(e\mu n\mathbf{E} + eD\nabla n) + e\frac{n'}{n_o}\,(-\frac{n}{\tau}) =$$

$$\frac{1}{n_o}\mu kT(\nabla n + \frac{e}{kT}nE)\cdot(\frac{e}{kT}n'E + \nabla n') - e\frac{nn'}{n_o\tau} - e\frac{n}{n_o}G\delta(r-r'))$$

$$-\frac{1}{n_o}\mu kT(\nabla n' + \frac{e}{kT}n'E)\cdot(\frac{e}{kT}nE + \nabla n) + e\frac{n'n}{n_o\tau} =$$

$$= - e\frac{n}{n_o}G\delta(r - r'). \qquad (2.7)$$

By using Gauss's theorem and from Eqs. (2.6) and (2.7)

$$\int \mathbf{A}\cdot d\mathbf{s} = \int \nabla\cdot\mathbf{A}\, dv,$$

$$[\exp(eV/kT)-1]I' = - e\int\frac{n}{n_o}G\delta(r-r')dv = -e\frac{n(r')}{n_o(r')}G. \qquad (2.8)$$

In (2.8) the ratio $n(r')/n_o(r')$ is the normalized excess minority-carrier density at $\mathbf{r} = \mathbf{r}'$. Because of the linearity of the system this density is linearly proportional to excess carrier density at the junction edge of the region: $n(r')/n_o(\mathbf{r}') = m_s(r')\,[\exp(eV/kT)-1]$, where $m_s(\mathbf{r}')$ is the saturation value of the normalized excess minority-carrier density at $r=r'$, in the dark. According to (2.8), therefore, the collection probability, C_p, of a carrier generated at point r' is

$$C_p(r') = m_s(r'). \qquad (2.9)$$

Equation (2.9) is similar to Donolato's final expression. It is more general because we include position dependencies of μ, D and n_o.

In a similar manner, one could prove another form of the reciprocity theorem applying to a quasineutral region in low injection: the minority-carrier quasi-Fermi level at point 1 due to a point source applied at point 2 is the same as the minority-carrier quasi-Fermi level at point 2 due to the same source applied at point 1. These theorems also hold for transients. This is proved by replacing n,I and n',I' in (2.2) by their Laplace transforms and $1/\tau$ by $s + 1/\tau$ for zero initial conditions. Here s is the Laplace transform variable. The result is that (2.9) for transients becomes

$$C_p(r',s) = m_s(r',s). \tag{2.10}$$

Equation (2.9) could be useful in solar cell and photodetector theory since it allows the calculation of short-circuit current from the analysis of the device under dark conditions:

$$I_{sc} = \sum_{i=1,2} e \int_i m_s(r)G(r)d^3r, \tag{2.11}$$

where 1,2 represent the quasineutral emitter and base of the cell. Equation (2.11) ignores generation in the space charge region and holds under the same assumptions underlying the proof of the reciprocity theorem. Equation (2.11) was derived on the assumption of a bias independent boundary S_J. In a realistic device S_J' moves with bias. This displacement, however, is of the order of the Debye length and in this transition area the minority carrier Fermi level is flat and $C_p(r) = m_s(r) = 1$. Therefore, the assumption of a bias independent S_J does not restrict the applications of the theorem unless the quasi neutral region thickness is comparable to the Debye length.

The major assumption in deriving (2.8) was low level injection so that the system could be treated as linear. Low injection guarantees linearity of the system even in the presence of the effects of heavy doping or graded chemical composition. In this case, in equation $-\nabla \ln n_o = eE/kT$, E will be the minority carrier field which includes the quasi-fields arising from the position dependent energy gap, electron affinity, and density of states.

Therefore, the original Shockley's proof of reciprocity can be extended to heavily doped three-dimensional base regions to obtain relations between input voltages and output currents. In this sense, Shockley's proof is more general than the recently published [3] proof of reciprocity in one-dimensional transistor base regions which takes into account heavy doping effects.

The practical significance of reciprocity is that it can reduce the number of unknowns in a problem and reduce the amount of calculations needed. As an example, in the recent paper by del Alamo and Swanson [4], the quantum efficiency of an emitter could have been found by using (2.11), since the minority-carrier density as a function of position was already numerically calculated under dark conditions. In addition, their forward and reverse transport factors and saturation currents are related by the equation $a_f J_{of} = a_r J_{or}$. Thus, the present reciprocity theorem can find use in the measurement of such device parameters as the surface recombination velocity at a polycrystalline silicon contact.

Although not discussed here, reciprocity relations enter the physics of many different phenomena, such as heat conduction or thermoelectric effect. These relations are based on fundamental considerations relating to detailed balance under thermal equilibrium and Onsager's principle of microscopic reversibility.

2.3 Exact Solution of Three-Dimensional Transport Problems Using One-Dimensional Models

This section shows that in certain three-dimensional devices a number of output parameters can be determined by exploiting existing solutions for related one-dimensional problems. The devices considered are mainly shallow planar structures, their three-dimensionality arising from mixed boundary conditions or non-uniform excitation. The devices either extend laterally to infinity (Fig. 2.1(a)) or they end at a passivated lateral surfaces of arbitrary shape forming thereby the general orthogonal cylindrical structure shown in Fig. 2.1(b). By passivated, we mean that the surface recombination velocity, S, is zero. The devices have one-dimensional counterparts having the same volume properties but uniform boundary conditions at the front and back planar surfaces. Each device and its one-dimensional counterpart are described by a common transport equation and by the same values of certain parameters, such as, the decay rate time constant, the transit time, the transport factor and the open-circuit photovoltage. Existing closed-form expressions for these parameters for the one-dimensional case, therefore, immediately apply to three-dimensional structures. In addition, we describe analytically certain measures of current and charge for devices having non-planar front and back surfaces. All these results are based on a second order linear differential equation which is derived from the continuity equation and is presented in the next subsection.

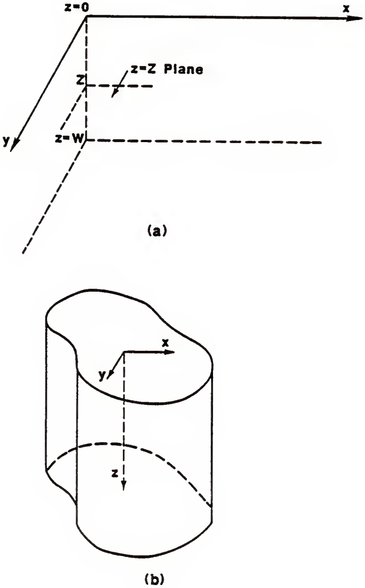

Fig. 2.1. Three-dimensional geometries under study.(a) An infinite slab having two surfaces at z = 0 and z = W and an internal plane at z=Z. (b) A cylindrical structure bounded by a lateral suface orthogonal to front and back surfaces.

2.3.1 Solution of the Continuity Equation in Planar Symmetry Cases

Now we consider that the sample shown in Fig. 2.1(a) is excited by a lazer beam. The laser beam is meant as an example of excitation. The following analysis is, in general, valid for any other type of excitation, for example, thermal generation, and minority-carrier injection over a potential barrier. The sample is n-type (extension to p-type is straightforward).

The continuity equation for the hole density is

$$\frac{\partial P}{\partial t}(x,y,z,t) = -\nabla\cdot J_p(x,y,z,t)+G(x,y,z,t) - U(x,y,z,t), \qquad (2.12)$$

where J_p is the hole flux density and G and U are generation and recombination rates in excess of their thermal equilibrium values. Integration of (2.12) over the $z = Z'$ $(0 < Z' < W)$ plane yields

$$\begin{aligned}\frac{\partial Q}{\partial t}(Z',t) &= -\int_{-\infty}^{\infty}\int_{-\infty}^{\infty}\nabla\cdot J_p\,dxdy + \int_{-\infty}^{\infty}\int_{-\infty}^{\infty}Gdxdy - \int_{-\infty}^{\infty}\int_{-\infty}^{\infty}Udxdy\\ &= -\int_{-\infty}^{\infty}\int_{-\infty}^{\infty}\left(\frac{\partial J_{px}}{\partial x}+\frac{\partial J_{py}}{\partial y}\right)dxdy - \int_{-\infty}^{\infty}\int_{-\infty}^{\infty}\frac{\partial J_{pz}}{\partial z}dxdy +\\ &\quad \int_{-\infty}^{\infty}\int_{-\infty}^{\infty}Gdxdy - \int_{-\infty}^{\infty}\int_{-\infty}^{\infty}Udxdy. \qquad (2.13(a))\end{aligned}$$

Here $Q(Z',t)$ is the number of holes per unit distance on the $z = Z'$ plane, and Jpx, Jpy, Jpz are the components of $J_p = J_{px}\mathbf{x} + J_{py}\mathbf{y} + J_{pz}\mathbf{z}$ ($\mathbf{x},\mathbf{y},\mathbf{z}$ are the unit vectors of the cartesian coordinate system). The above integrals are finite for realistic generation profiles.

By Gauss's theorem,

$$\int_{-\infty}^{\infty}\int_{-\infty}^{\infty}\left(\frac{\partial J_{px}}{\partial x} + \frac{\partial J_{py}}{\partial y}\right) dxdy = \int_{\Gamma_\infty}(J_{px}\mathbf{x} + J_{py}\mathbf{y})\cdot ds, \qquad (2.13(b))$$

where Γ_∞ is the infinite circle on the z=Z′ plane, and ds is the infinitesimal vector normal to Γ_∞. The integral $\int_{\Gamma\infty} (J_{px}\mathbf{x} + J_{py}\mathbf{y})ds$ is the hole flux crossing the infinite circle,per unit distance. This integral is zero for any realistic generation function, since the total flux crossing the entire surface at the infinite is bounded by the total generation rate. Therefore, (2.13(a)) becomes

$$\frac{\partial Q}{\partial t} = -\iint \frac{\partial J_{pz}}{\partial z}\, dxdy + \iint G\, dxdy - \iint U\, dxdy, \qquad (2.14)$$

where from now on we omit the (infinite) limits of integration for brevity. Equation (2.14) is a general equation and relates the total charge and current crossing a plane to the generation-recombination rate on the same plane. We focus now our attention to planar devices in low injection where internal parameters like electric field, E, diffusivity, D, mobility, μ, and lifetime, τ, are functions only of z and are independent of the minority-carrier density. Expressing the minority flux density in terms of drift and diffusion of the excess holes, $P' = P - P_o$, and the recombination rate as $U = P'/\tau$, we can rewrite (2.14) as

$$\frac{\partial Q'}{\partial t} = D\,\frac{\partial^2 Q'}{\partial z^2} + \left(\frac{dD}{dz} - \mu E_z\right)\frac{\partial Q'}{\partial z} - \left(\frac{d(\mu E_z)}{dz} + \frac{1}{\tau}\right) Q' + \iint G\, dxdy, \qquad (2.15)$$

where $Q' = \iint P' dxdy$ is the number, per unit distance, of excess holes on the z=Z′ plane. Equation (2.15) is linear provided that E_z, D, μ and τ are independent of the Q′ because of low injection. The same equation also holds for the device shown in Fig. 2.1(b) since the current crossing the passivated lateral surface is zero.

The recombination velocities S_1, S_2 of the front (z=0) and back (z=W) surface of the sample enter to determine the boundary conditions of Eq. (2.15):

$$S_1\, Q'(t,0) = D\,\frac{\partial Q'}{\partial z}(t,0) \quad , \quad S_2\, Q'(t,\, W) = -D\,\frac{\partial Q'(t,W)}{\partial z} \,. \qquad (2.16)$$

Under such boundary conditions the solution of Eq. (2.15) depends only on the total generation rate on the z = Z′ plane and not on G as a function of x and y. A similar conlusion has been reached in [5]. Knowledge of Q′(z,t) does not, of course, provide P′(x,y,z,t). However, it does provide the total minority current in the z direction, $I_z = -eD\partial Q'/\partial z + e\mu E_z Q'$, and the total number of excess holes on the z=Z′ plane.

Therefore, when one seeks to determine either the total minority current or the number of excess holes, (2.15) suffices, provided only that the transport parameters of the semiconductor do not depend on the injection level and are functions only of z. Equation (2.15) is much more convenient to use in the determination of (measurable) current than is the standard continuity equation. In the following subsections we will apply (2.15) to derive solution for three dimensional transport problems in planar devices.

2.3.2 Photoluminescence Decay Response

Photoluminescence decay is one of the methods used in determining the minority-carrier lifetime in heavily doped silicon [6]. The method consists of exciting a silicon sample by a laser pulse and thus generating excess electron-hole pairs. The lifetime is derived from the decay rate of the excess charge. This decay as a function of time is obtained by monitoring the radiation emitted by the few electron-hole pairs that recombine through radiative recombination. In principle, this method is more reliable than any other methods because it involves no assumptions regarding the band structure and the transport parameters in heavily doped silicon. On the other hand, the method has the drawback that surface recombination prohibits the decay from being purely exponential. Moreover, the effect on the decay rate of the size and shape of the laser beam was not clarified previously. Recent papers [7,8] have investigated the time dependence of the luminescence decay, and in particular the influence of surface recombination on the decay rate for special types of excitation. Ioannou and Gledhill [7] solved the continuity equation analytically for the total excess charge in the case of a finely focused beam, while Tyagi et al. [8] simplified the problem to one dimension by considering uniform excitation. In both cases it is found that the effect of the surface recombination can be minimized by waiting several lifetimes, after the laser is turned off, before measuring the decay rate. Here we extend the analysis for the general case of arbitrary excitation, and prove that the beam size, shape and uniformity does not affect the decay rate. An upper bound for the error due to surface recombination is derived. In agreement with references 6,7,8 the effect of surface recombination is found to be significant only in the initial part of the transient.

We now apply (2.15) to the study of the decay of the excess charge induced by a laser pulse in a semi-infinite ($W = \infty$) sample having position independent doping concentration. For low injection minority carriers flow by diffusion and for D independent of z (2.15) simplifies to

$$\frac{\partial Q'}{\partial t} = D \frac{\partial^2 Q'}{\partial z^2} - \frac{Q'}{\tau} + G_t(t)(1-R)\alpha\, e^{-\alpha z}, \qquad (2.17(a))$$

where $G_t(t)$ is the total photon flux of the laser beam, R is the reflection coefficient, and α is the absorption coefficient.

The boundary conditions are

$$Q'(0,z) = 0,\ Q'(t,\infty) = 0,\ \ Q'(t,0)S = D\,\frac{\partial Q'(t,0)}{\partial t}, \qquad (2.17(b))$$

where S is the surface recombination velocity.

If $G_t(t)$ is the unit impulse function, $G_t(t) = \delta(t)$, then Laplace transformation of (2.17(a)) with time yields

$$D\,\frac{\partial^2 Q'(s,z)}{\partial z^2} - (s + \frac{1}{\tau})\, Q' = -(1-R)\alpha\, e^{-\alpha z}, \qquad (2.18)$$

where s is the Laplace transform operator. The boundary conditions for (2.18) are the Laplace transformation of (2.17(b)). The solution is

$$Q'(s,z) = \frac{\alpha \exp(-\alpha z)(1-R)}{-D\alpha^2+s+1/\tau} - (\Gamma+\alpha)\alpha\sqrt{D}(1-R)$$

$$\times \frac{(\sqrt{s+1/\tau} - \sqrt{D}\Gamma)\exp(-\sqrt{(s+1/\tau)/D}\ z}{(-D\alpha^2+s+1/\tau)(-D\Gamma^2+s+1/\tau)}, \qquad (2.19)$$

where $\Gamma = S/D$.

If $Q'_t(t)$ is the total number of excess carriers and $Q't(s)$ its Laplace transformation, then

$$Q_t'(t) = \int_0^\infty Q'(t,z)\ dz \rightarrow Q_t'(s) = \int_0^\infty Q'(s,z)dz$$

$$= \frac{1-R}{-D\alpha^2+s+1/\tau} - \frac{(1-R)(\Gamma+\alpha)\alpha D(\sqrt{s+1/\tau} - \sqrt{D}\Gamma)}{\sqrt{(s+1/\tau)}(-D\alpha^2+s+1/\tau)(-D\Gamma^2+s+1/\tau)}. \qquad (2.20)$$

Taking the inverse Laplace transform of (2.20), we obtain

$$Q_t'(t) = \Gamma\alpha(1-R)(\Gamma-\alpha)^{-1}\exp(-t/\tau)[\alpha^{-1}\exp(L^2\alpha^2 t/\tau)\text{erfc}(L\alpha\sqrt{t/\tau}) -$$

$$\Gamma^{-1}\exp(L^2\Gamma^2 t/\tau)\text{erfc}(L\Gamma\sqrt{t/\tau})], \qquad (2.21)$$

where $L = \sqrt{D\tau}$ is the hole diffusion length and erfc is the complementary error function. This result holds independently of the beam shape and is the same as Equation (8) of Ioannou and Gledhill [7] derived in the case of a finely focused beam.

If the laser pulse has a flux $N(t)$ that lasts for a finite time T, then the response $Q''_t(t)$ will be the convolution of $N(t)$ with $Q'_t(t)$:

$$Q''_t(t) = \int_0^t N(t')Q'_t(t-t')dt'. \qquad (2.22)$$

If N(t) is a square pulse of amplitude N and width T, then (2.22) yields for $t \geq T$

$$Q''_t(t) = \Gamma\alpha(1-R)(\Gamma-\alpha)^{-1}N\tau\exp(-t/\tau)$$

$$\times \{-(L^2\alpha^2-1)^{-1}\alpha^{-1}\ F(L\alpha,t) + (\Gamma^2L^2-1)^{-1}\Gamma^{-1}\ F(\Gamma L,t)$$

$$+ L[(L^2\alpha^2-1)^{-1} - (L^2\Gamma^2-1)^{-1}]\ F(1,t)\ \}, \qquad (2.23(a))$$

where

$$F(y,t) = \exp(T/\tau)\exp(y^2(t-T)/\tau)\mathrm{erfc}(y\sqrt{(t-T)/\tau}) -$$

$$\exp(y^2t/\tau)\mathrm{erfc}(y\sqrt{t/\tau}).$$

If $S = \Gamma = 0$, (2.23(a)) reduces to

$$Q''_t(t) = N\ \tau\ (1-R)[\exp(T/\tau)\ -1]\ \exp(-t/\tau),\ t \geq T \ (2.23(b))$$

which is a purely exponential function with time constant t.

As a more general statement, if $S = 0$ the decay of the excess charge will be exponential independently of the shape of the surface at which the sample terminates and independently of the presence of internal fields. This can be proved by integrating the continuity equation

$$\frac{\partial P'}{\partial t} = -\nabla \cdot J_p - \frac{P'}{\tau} \qquad (2.23(c))$$

over the volume of the sample and applying the divergence theorem:

$$\frac{dQ'}{dt} = \int_S J_p \cdot ds - \frac{Q'}{\tau} . \qquad (2.23(d))$$

Here Q′ is the excess minority-carrier charge and the integral above is the hole flux at the surface. This vanishes for $S = 0$. Therefore,

$$\frac{dQ'}{dt} = -\frac{Q'}{\tau} \qquad \text{and} \qquad Q'(t) = Q'(0)\exp(-t/\tau). \qquad (2.23(e))$$

When $S > 0$, (2.23(a)) implies that $Q"_t(t)$ is not exponential. A measure of the deviation of $Q"_t$ from the exponential function (Constant $\exp(-t/\tau)$) follows from considering the function:

$$\frac{-d[\ln Q''_t(t)]}{dt} = -\frac{dQ''_t/dt}{Q''_t} = \frac{1}{\tau} + \frac{db(t)/dt}{b(t)}. \qquad (2.24)$$

where b(t) is the negative of the expression in the curly bracket of (2.23(a)). The smaller that $[db(t)/dt)/b(t)]$ is the more accurate the estimation of t by the slope of $\ln Q"t$ is.

One can prove that $[db(t)/dt]/b(t)$ is an increasing function of S and 1/T. As a worst case, we consider infinite recombination velocity and impulse excitation. Then $Q"_t$ becomes

$$Q"_t = N'(1-R)\exp(L^2\alpha^2 t/\tau)\,\mathrm{erfc}(L\alpha\sqrt{t/\tau})\exp(-t/\tau), \qquad (2.25(a))$$

where N′ is the strength of the pulse. In such a case

$$\frac{db(t)/dt}{b(t)} = \frac{1/\sqrt{\pi} - L\alpha\sqrt{t/\tau}\,\exp(L^2\alpha^2 t/\tau)\,\mathrm{erfc}(L\alpha\sqrt{t/\tau})}{\exp(L^2\alpha^2 t/\tau)\,\mathrm{erfc}\sqrt{(L\alpha(t/\tau))}}\,\frac{L\alpha\sqrt{t/\tau}}{t}. \qquad (2.25(b))$$

This ratio is an increasing function of $L\alpha$ and when $L\alpha \to \infty$, then $[db(t)/dt]/b(t) \to 1/2t$. Therefore, in the worst case, by measuring the slope $\ln Q''_t$ at time t, the time constant derived will be $\tau/[1+(\tau/2t)]$ instead of τ. Thus $\tau/2t$ is an upper bound for the error in determining τ. This bound is much lower than the one, $2.47\tau/t$, considered by Tyagi et al [8]. Consequently, the maximum error of Dziewior and Schmid [6] due to surface recombination is approximately $\tau/[2(5\tau)] = 10\%$, since from their data it appears that they waited five lifetimes before measuring the slope. Thus their results are reliable in so far as surface recombination is concerned.

If an accuracy of 20% in the recombination lifetime is required, then $0.8 = 1/[1+(\tau/2t)]$ which implies t=2t. Now the question arises, how can one know when t is equal or greater than 2τ? If $L\alpha(t/\tau)^{1/2}>2$ (2.25(a)) can be simplified:

$$Q''_t(t) \approx Q''_t(0) \frac{\exp(-t/\tau)}{(\pi t/\tau)^{1/2} L\alpha} . \tag{2.26}$$

This implies that $Q''_t(2\tau) \approx 0.05\ Q''_t(0)\ 1/L\alpha$. If L is not known but one can estimate its range, then α can be chosen so that $L\alpha < 5$, implying $Q''_t(2\tau) \geq 0.01\ Q''_t(0)$. Therefore, by waiting until the response drops to 1% of its initial value, t will be greater than 2τ and the error less than 20%.

2.3.3 Transit Time and Transport Factor in Planar Devices

Here we will use (2.15) to show that shallow planar devices have transit times and transport factors that are equal or related to the transit times and transport factors of corresponding one dimensional devices. The devices considered are made on substrates which are infinite or terminate at a passivated (S=0) cylindrical surface orthogonal to x-y plane, as shown in Fig. 2.1. Infinite in this context means that the lateral surface is several diffusion lengths away from the injecting boundary. The device, shown in Fig. 2.2, is homogeneous across planes parallel to x-y planes. The z component of the electric field, E_z, minority-carrier lifetime, τ, and mobility, μ, are functions only of z. The back surface of the diode is characterized by a uniform recombination velocity S_2 while the part of the emitter not occupied by the junction has $S=S_1$. Initially we set S_1 equal to zero. Later we discuss the effect of finite S_1 on the transit time. The emitter is assumed to have zero thickness. To the device shown in Fig. 2.2 corresponds a one-dimensional device bounded by the same planes and having the same mobility, lifetime, and field strength as functions of z, as the device in Fig. 2.2. The two diodes differ only in the boundary conditions at the top surface: the diode in Fig. 2.2 has mixed boundary conditions while its one-dimensional counterpart has uniform boundary conditions. The similarity between the two problems will be used in the following cases to show that certain three-dimensional transport problems can be solved in terms of one-dimensional models and in some cases can have closed form solutions.

The base transit time of the diode of Fig. 2.2. is given by

$$\tau_t = \frac{Q_t}{I_D} = \frac{\int_0^W Q(z)\,dz}{-D(0)dQ(0)/dz + \mu(0)E_z(0)Q(0)}, \qquad (2.27)$$

where Q_t is the total number of excess holes (for convenience holes are taken to be the minority carriers) stored in the base when the

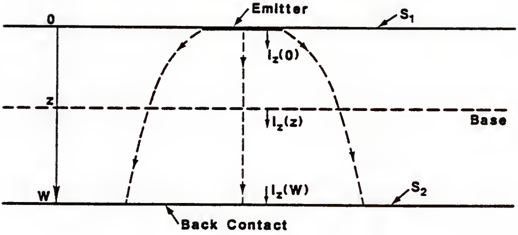

Fig. 2.2 A shallow diode formed on a semiconductor slab. The dashed lines connecting the emitter with the back contact are the minority-carrier flow lines, while the dashed line that is parallel to the front and back surface defines an internal plane.

base minority current is I_D. In (2.27), $I_D = I_z(0) = -D(0)dQ(0)/dz + \mu(0)Ez(0)Q(0)$ because there is no surface recombination since $S_1 = 0$. Here $I_z(z)$ is the total hole flux in the z direction.

In steady state and under no volume excitation (2.15) becomes

$$D(z)\frac{d^2Q}{dz^2} + A(z)\frac{dQ}{dz} + B(z)Q = 0, \qquad (2.28)$$

where $A(z) = dD/dz - \mu E_z$ and $B(z) = -d(\mu E_z)/dz - 1/\tau$. The boundary condition at $z = W$ is

$$\mu(W)E_z(W)Q(W) - D(W)dQ(W)/dz = S_2Q(W). \qquad (2.29)$$

The other boundary condition could involve the total charge on the front surface, Q(0). Knowledge of Q(0) would require a complete solution of the three-dimensional boundary value problem. This is not necessary, however, if only τ_t is to be calculated. Consider the one-dimensional diode having the same $\mu(z)$, $E_z(z)$, $D(z)$, $t(z)$, W and S_2. Here, of course, the junction covers the entire front surface. We will prove that the two diodes have the same transit time. Let $Q'(z)$ be the excess hole density and $J'(z)$ the hole current density of the one dimensional device. The quantity $Q'(z)$ will obey the same differential equation (2.28) and the same boundary condition (2.29), as $Q(z)$ does.

From (2.29)

$$\frac{dQ/dz}{Q} = \frac{dQ'/dz}{Q'} = \frac{\mu(W)E_z(W)-S_2}{D(W)}. \qquad (2.30)$$

Thus, the Wronskian of Q and Q' is zero at z=W and, therefore, is zero everywhere. Consequently, for any qiven bias V the ratio $Q(z)/Q'(z)$ is independent of z and depends only on the geometry of the diode. Thus, for any value of z between 0 and W

$$\frac{Q(z)}{Q'(z)} = \frac{dQ(z)/dz}{dQ'(z)/dz} = \frac{-D(z)dQ(z)/dz + \mu(z)E(z)Q(z)}{-D(z)dQ'(z)/dz + \mu(z)E(z)Q'(z)} = \frac{I_z(z)}{J'(z)}$$

$$= \text{Constant}. \tag{2.31}$$

Therefore,

$$\frac{Q(z)}{Q'(z)} = \frac{\int_0^W Q(z)dz}{\int_0^W Q'(z)dz} = \frac{Q_t}{Q'_t} = \frac{I_z(0)}{J'(0)}, \tag{2.32}$$

where Q_t and Q_t' is the total hole number and total hole number per unit area in the three-dimensional and one-dimensional diode, respectively. Equations (2.31) and (2.32) hold for any values of S. If S=0, then $I_z(0)=I_D$, where I_D is the base recombination current of the three-dimensional diode. Let J′ be the base recombination current density for the corresponding one-dimensional diode. Since $J' = J(0)$, then from (2.32)

$$Q_t'/J' = \tau_t' = \tau_t = Q_t/I_D. \tag{2.33}$$

Therefore, the one-dimensional transit time, τ_t', is the same as the transit time of the shallow junction diode. Since no assumptions were made regarding the shape of the junction, (2.33) holds for any junction morphology if the thickness is very small compared to the diffusion length and base thickness W. Thus, if the base is uniform, closed form expressions are available for τ_t. For example, if $S_2 = \infty$ and $W \ll (D\tau)^{1/2}$, then $\tau_t = W^2/2D$. In the general case, the ordinary differential equation (2.28) would have to be solved by some numerical methods. This is much simpler than solving the three-dimensional boundary value problem.

The derivation of (2.33) was based on the assumption of zero recombination current at the front surface. Allowing for a finite S_1, the hole recombination current becomes

$$I_D = -D(0)\frac{\partial Q(0)}{\partial z} + \mu(0)E\ (0)Q(0) + [Q(0) - A(\exp\frac{eV}{kT} - 1)\ P_o]S_1, \quad (2.34)$$

where A is the junction area, P_o is the equilibrium hole density at z=0 and V the applied voltage. The term in the square bracket in (2.34) is the total hole number, per unit distance, on the uncovered front surface. Since (2.31) is still valid if the charges and the currents involved are replaced by their saturation values, we can write

$$-D(0)\frac{\partial Q(0)}{\partial z} + \mu(0)E_z(0)Q(0) = \frac{Q_o}{P_o} J_o', \quad (2.35)$$

where J_o' is the saturation current density of the corresponding one-dimensional diode, and Q_o is the saturation value (pre-exponential factor) of the number of holes, per unit length, at z=0. Thus, from (2.35) and (2.34) we obtain

$$Q_o = (I_o + S_1 A P_o)/(J'_o/P_o + S_1). \quad (2.36)$$

By combining (2.36) with (2.32) and (2.33) we obtain

$$\frac{\tau_t I_o}{\tau_t' J_o'} = \frac{Q_{to}}{Q_{to}'} = \frac{Q_o}{P_o} = \frac{I_o/P_o + S_1 A}{J_o'/P_o + S_1},$$

$$\frac{\tau_t}{\tau_t'} = \frac{1+S_1 A P_o/I_o}{1+S_1 P_o/J_o'}. \qquad (2.37)$$

Equation (2.37) provides a way of measuring the product $S_1 P_o$ if the ratio τ_t/τ_t' is known.

Going back to the case of the passivated front surface, it is possible to prove that (2.33) holds also for the sinusoidal steady state excitation. Here $\tau_t' = Q_t'/J'$ and $\tau_t = Q_t/I_d$ where Q_t, J_d, Q_t, I_d are the phasor amplitudes of the corresponding quantities, of the one and three-dimensional devices, oscillating around the equilibrium point. For example, $i_D(t) = I_D + I_d \exp(i\omega t)$. It is assumed that the amplitude of the a.c. component of the terminal voltage is very small compared to the thermal voltage. To prove this, it is enough to rewrite (2.38) in the sinusoidal steady state

$$D(z) \frac{d^2Q}{d^2z} + A(z) \frac{dQ}{dz} + [B(z) - i\omega]\, Q = 0 \,. \qquad (2.38)$$

The similarity between (2.28) and (2.38) makes evident that the one and three-dimensional transit times are the same in the sinusoidal steady state, also.

We may think of the device in Fig. 2.2 as a transistor, where emitter and base retain the same position while the collector extends under the base. Now, in the forward active mode the boundary condition at $z = W$ becomes $S_2 = \infty$ or $Q(W) = 0$. If we define the transit time in the base of this transistor as

$$\tau_{tw} = \frac{Q}{I_z(W)} = \frac{Q}{-D(W)\ dQ(W)/dz}, \tag{2.39}$$

then based on the discussion preceding (2.33), one can prove that

$$\tau_{tw} = \tau_{tw}', \tag{2.40}$$

where $\tau_{tw}'$is the transit time of the corresponding one dimensional-transistor. Equation (2.40) is valid for any position dependent recombination velocity in the front surface and any shape of the emitter.

If we remove the assumption of the infinitesimally thin emitter, we can no longer derive closed form expressions for the transit time in the general case. It is possible, however, to place the transit time of the three-dimensional base between upper and lower limits. In Fig. 2.3 a transistor is shown having an emitter of finite thickness. The transit time can be written as

$$\tau_{tw} = \frac{Q_t}{I_z(W)} = \frac{Q_t}{Q_t(W-d)} \frac{Q_t(W-d)}{I_z(W)} > \frac{Q_t(W-d)}{I_z(W)} = \tau_{tw}'(W-d), \tag{2.41}$$

where $Q_t(W-d)$ is the number of excess holes in the region $d < z < W$ and $\tau_{tw}'(W-d)$ is the transit time of the one-dimensional transistor having its base extending from z=d to z=W. We can now imagine the junction to shrink towards plane z=0 in such a way that its original position remains an equipotential surface (potential in the sense of the minority-carrier quasi-Fermi potential). This can be practically done by extrapolating the minority-carrier flow lines in the emitter and drawing the equipotential surfaces that are orthogonal to them.

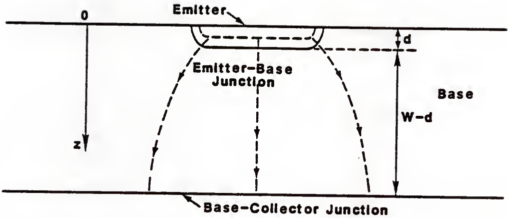

Fig. 2.3 A planar transistor with an emitter of finite thickness.

In the limit, when the emitter will have collapsed on the front surface, the transit time of the new base will be $\tau_{tw}(W)$, the same, according to (2.40), as in the one-dimensional transistor with its base extending from z=0 to z=W. For a given collector current, the charge stored in the base of this hypothetical transistor will be more than that stored in the actual base shown in Fig. 2.3 by the amount of the charge stored in the removed emitter. Thus $\tau_{tw} < \tau_{tw}'(W)$. From this inequality and (2.41) the upper and lower bounds for τ_{tw} become

$$\tau_{tw}'(W-d) < \tau_{tw} < \tau_{tw}'(W). \qquad (2.42)$$

Going back to the transistor with the shallow junction, it can be seen from (2.31) that the base transport factor, B_T, of this transistor is equal to the transport factor, B_T', of the corresponding one-dimensional transistor, if $S_1=0$. If S_1 is finite, then, by the same procedure that led to (2.37), we obtain

$$B_T = B_T' \frac{1+AP_oS_1/I_o}{1+P_oS_1/J_o}, \qquad (2.43)$$

where I_o and J_o are the collector saturation current and current density of the three and one-dimensional transistors respectively, $I_z(W)=I_o[\exp(eV/kT)-1]$. The assumption of a uniform recombination velocity on the base surface is not unrealistic if this surface is covered by a thin polysilicon layer that provides isolation of the active base from the base ohmic contact. Equation (2.43) can in fact be used to determine the product P_oS_1 characterizing this polysilicon layer contact.

2.3.4 Base Recombination Currents in Three-Dimensional Photovoltaic Devices

In Fig. 2.4 is shown a solar cell having a textured emitter to improve its collection efficiency. The saturation value of the hole particle current in the base can be determined without solving the three-dimensional problem, if this assumption can be made: a quasi-equilibrium condition exists in the sense that the minority hole quasi-Fermi level is position independent in the emitter pyramids bounded by the dashed lines from above and by the dashed-dotted line from below. This assumption is good when (a) the dimensions of the pyramids are small compared with an average base diffusion length and (b) either the base thickness is much greater than the diffusion length, or the back surface of the base is passivated for minority-carrier recombination. In many silicon solar cells having texturized front surfaces, these conditions will hold because the dimensions of the pyramids are a few microns whereas the diffusion length and cell thickness are many tens of microns.

This assumption and the same arguments as in the previous section imply a simple determination of the saturation value of the hole recombination rate, I_o, in the region $0 < z < W$. This saturation current of the structure of Fig. 2.4 equals the saturation hole current, I_o', of a related one-dimensional cell having a planar emitter, the same area and a quasi-neutral base extending from $z=0$ to $z=W$ and having the same volume parameters and back surface recombination velocity S_2. For completeness, we can add to I_o the saturation value of the recombination rate in the quasi

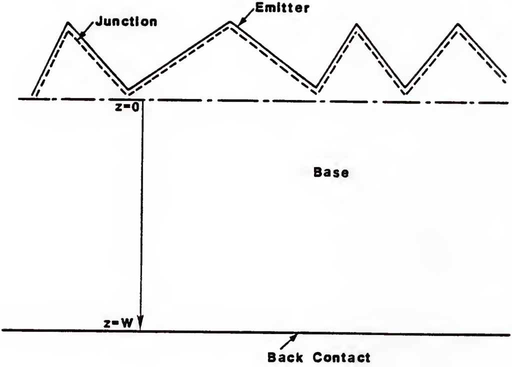

Fig. 2.4 A photovoltaic device with a texturized emitter.

equilibrium pyramids: $\int_{\text{Pyramids}} = [P_o(r)/\tau(r)]d^3r$, where $P_o(r)$ and $\tau(r)$ are the equilibrium hole density and lifetime at point r. Thus the total hole saturation particle current in the entire base can be expressed as

$$I_o = I_o' + \int_{\text{Pyramids}} (P_o/\tau)\ d^3r. \qquad (2.44)$$

2.3.5 Open-Circuit Voltage and Reciprocity Relations in Planar Photovoltaic Devices

In Fig. 2.5 is shown a solar cell, or a photodetector, having a very shallow emitter which covers only part of the front surface. The uncovered front surface of the base is well passivated ($S_1=0$). The emitter may have any shape and area. It can also be a strip or a number of strips. The illumination is assumed independent of x and y and the front-grid coverage negligible, so that the generation rate G is a function only of z: $G=G(z)$. In the absence of emitter recombination, the open-circuit voltage of this cell in low injection will be the same, under the same illumination, as that of the one-dimensional cell having the same base and a uniform emitter covering the entire front surface. To prove this we will use the reciprocity theorem presented in section 2.2 to express the collection probability $P_c(r)$ of a minority carrier generated at point r as $P_c(r)= P_s(r)/P_o(r)$, where P_s is the saturation value of the excess minority-carrier density at r in the dark and P_o is the equilibrium minority-carrier density. Applying this relation to the cell shown in Fig. 2.5 we can write the short-circuit current as

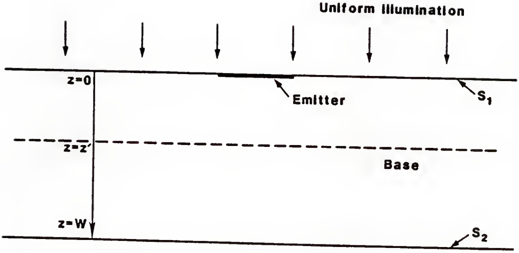

Fig. 2.5 A planar solar cell with a shallow emitter. The illumination is uniform in the x-y plane.

$$I_{SC} = \int_{base} G(r)P_c(r)\, d^3r = \int_0^W G(z')dz' \int_{z=z'} \frac{P_s(x,y,z')}{P_o(x,y,z')}\, dxdy$$

$$= \int_0^W \frac{G(z')Q_s(z')}{P_o(z')}\, dz', \tag{2.45}$$

where $Q_s(z')$ is the saturation value of total number, per unit distance, of excess holes in the $z=z'$ plane in the dark. If Q'_s is equivalent quantity for the corresponding one-dimensional cell, then using (2.32) we can write

$$Q_s(z') = Q_s'(z')I_o/J_o', \tag{2.46}$$

where I_o and J_o are the saturation current and saturation current density of the cell shown in Fig. 2.5 and the one-dimensional cell, respectively. From (2.45) and (2.46),

$$I_{SC} = \frac{I_o}{J_o'} \int_0^W G(z') \frac{Q_s'(z')}{P_o(z')}\, dz' = \frac{I_o}{J_o'} \int_0^W G(z')P_c'(z')dz = \frac{I_o}{J_o'} J_{SC}', \tag{2.47}$$

where J_{SC}' is the short-circuit current density one-dimensional cell. Since the open-circuit voltage is given by $V_{OC} = (kT/e)Ln(I_{SC}/I_o)$ from (2.47) it follows that

$$V_{OC} = (kT/q)Ln(I_{SC}/I_o) = (kT/e)Ln(J_{SC}'/J_o') = V_{OC}' \tag{2.48}$$

If the front surface recombination velocity has a finite value S_1, then by analogy to (2.37), we can prove that

$$\frac{I_{SC}}{I_o} = \frac{J_{SC}'}{J_o'} \frac{1 + AP_oS_1/I_o}{1 + P_oS_1/J_o'}, \tag{2.49}$$

so that the voltage becomes

$$V_{OC} = V'_{OC} - (kT/q)\mathrm{Ln}[(1 + AP_oS_1/I_o)/(1 + P_oS_1/J_o')], \quad (2.50)$$

where P_o is the equilibrium density of holes at the front base surface. Equations (2.49) and (2.50) provide an alternative way of measuring P_oS_1. Equations (2.37), (2.43) and (2.49) show that normalized quantities like the transit time, the transport factor or the ratio I_{SC}/I_o differ from the analogous values of the corresponding one-dimensional diode or transistor by a common factor: $(1+AP_oS_1/I_o)/(1+S_1P_o/J_o)$. Of course, if $S_1=0$ these values become the same. In the particular case where light generates carriers only at the surface, (2.47) implies a result already reached by Holloway, Brailsford and Sander [9,10] through another method. This result states that the fractional increase in the collecting area of a photodiode due to lateral diffusion of photogenerated carriers at the surface is equal to the fractional increase of the diode saturation current compared with that of the one-dimensional diode. Equations (2.48) and (2.49) hold also for the interdigitated [11,12] or point contact [13] cell provided the back diffused contact regions are shallow. In such cells, however, the assumption of low injection could become unrealistic since these cells usually have lightly doped bases and are subjected to high concentration ratios.

The fact that for passivated front surfaces the ratio I_{sc}/I_o is emitter geometry independent has design implications: in a solar cell with partitioned emitter for a given front surface coverage, or back surface in an interdigitated cell, the short-circuit current increases when finer geometries for the emitter lines or point contacts are used. This results because I_o increases due to the more pronounced three-dimensional effects.

Reciprocity can also be used to relate the recombination current of the two different devices shown in Fig. 2.6. Figure 2.6(a) illustrates part of the emitter of a planar solar cell. This emitter is bounded by the front surface which is assumed passivated with $S_1=0$, by the strip ohmic contact and by the injection boundary. The reciprocal diode is shown in Fig. 2.6(b). Here a shallow strip junction replaces the ohmic contact and the boundary at $z=W$ becomes an infinite ohmic contact. In other words, the injecting boundary and the ohmic contact interchange positions from Fig. 2.6(a) to Fig.2.6(b). The bulk properties of the principal regions are the same as well as S_1. Since the diode shown in Fig. 2.6(b) has been, to some extent, analyzed [14] it is of interest to derive reciprocity relations that would express the recombination current of the device in Fig.2.6(a) in terms of that of the diode in Fig. 2.6(b), thus eliminating the need to solve the new boundary value problem.

We introduce again the one-dimensional diode that corresponds to the device shown in Fig. 2.6(b) and has the entire $z = 0$ plane occupied by the shallow junction. Let I_{ao} and I_{bo} be the saturation value of the total particle current in the negative and positive direction of the devices in Fig.2.6(a) and 2.6(b), respectively. By J'_{bo} we denote the current density of the corresponding one-dimensional diode. Using the conventional reciprocity theorem relating voltages and currents in the base of a transistor, we derive

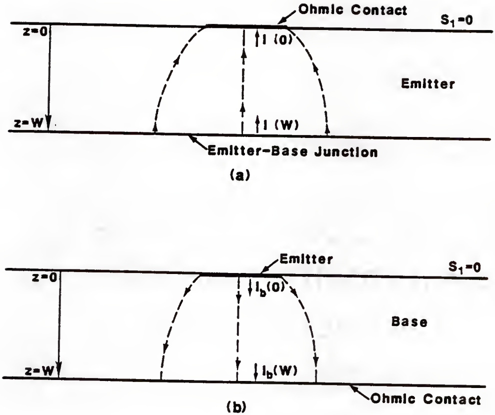

Fig. 2.6 Reciprocal bipolar devices. (a) Part of the emitter of a planar solar cell showing the minority-carrier flow lines and the strip contact. (b) A shallow strip p/n junction on a planar base having an ohmic contact.

the relation

$$I_{ao}(0) = I_{bo}(W). \qquad (2.51)$$

From (2.31) follows

$$I_{bo}(W)/I_{bo}(0) = J_{bo}'(W)/J_{bo}'(0). \qquad (2.52)$$

From (2.51), (2.52) we have

$$I_{ao}(0) = I_{bo}(0)\ [J_{bo}'(W)/J_{bo}'(0)]. \qquad (2.53)$$

The last equation expresses the recombination at the ohmic contact of the emitter of Fig. 2.6(a) in terms of the recombination current of the diode in Fig. 2.6(b) and the recombination currents of the one dimensional diode. Analytical expressions similar to (2.53), though more complicated, can be also obtained for finite S_1. From (2.53), from relations derived in reference [14], and from the reciprocity theorem we can write an approximate formula for the recombination rate under the emitter strip. The relative increase, R, of this rate due to two-dimensional minority-carrier diffussion spreading under the strip, is given by

$$R = (L_c/L')(J_{bo}'(W)/J_{bo}'(0)), \qquad (2.53)$$

where L' is the width of the strip, L_c is a characteristic length, approximately equal to the minimum between an average minority-carrier diffusion length in the emitter and W. In conventional solar cells this ratio is usually negligibly small. In some of today's high efficiency cells, however, especially those made for concentrator modules, R could have non-negligible values.

2.3.6 Arbitrary Boundaries

So far we have discussed planar structures where the only deviation from one-dimensionality was the boundary condition at the planar surface. Equation (2.15), however, may have more general applications. Figure 2.7 shows a quasi-neutral region limited by arbitrary surfaces which can be its external surfaces or the injecting boundaries. The device is either infinite in the x-y direction or terminates at a lateral surface orthogonal to the x-y plane. If the quasineutral region has space-independent transport parameters, then, in the steady state and for a generation profile of the form $G(z)=g \exp(-\alpha z)$, (2.15) becomes

$$D \frac{d^2Q}{dz^2} - \frac{Q}{\tau} = g \exp(-\alpha z). \qquad (2.53)$$

Equation (2.53) has a general solution

$$Q(z) = A\exp(-x/L) + B\exp(x/L) + [g/(D\alpha^2-1/\tau)]\exp(-\alpha z), \qquad (2.54)$$

where A, B are constants and $L=(D\tau)^{1/2}$. In addition

$$I_z(z) = DA\exp(-x/L)/L - DB\exp(x/L)/L + D\alpha[g/(D\alpha^2-1/\tau)]\exp(-\alpha z). \qquad (2.55)$$

To determine A and B the boundary value problem would have to be solved. However, even with A and B undetermined, (2.55) provides an analytical expression of how the charge and the current in the z direction changes with position.

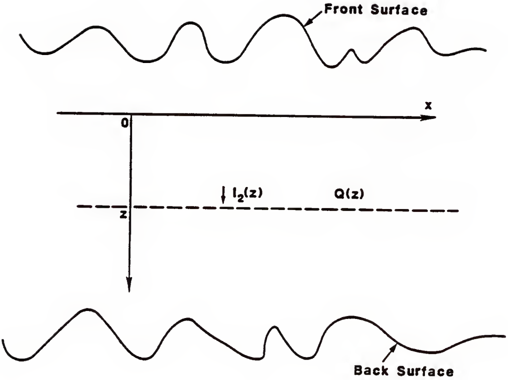

Fig. 2.7 A quasi-neutral region bounded by arbitrary surfaces.

2.4 Conclusions

In the first part of this chapter we presented a reciprocity theorem that equates the collection probability in the base of a photovoltaic device to the normalized excess carrier density under electrical bias in the dark. In the second part we showed that planar devices have the same excess carrier decay rate, transit time, transport factor and open-circuit voltage as the corresponding one-dimensional counterparts, when the front surface recombination velocity is zero. For finite values of the recombination velocity, analytical formulas were derived that can be used when characterizing the front surface. The base recombination rate per unit area of a texturized emitter solar cell is the same as the recombination rate of the same cell with planar emitter. Partitioning the emitter in a base limited cell, to reduce the area and the associated recombination, leaves the open-circuit voltage unchanged. Finer emitter geometries result in higher short-circuit currents. General analytical formulas were also derived for the charge and current of non-planar devices.

CHAPTER THREE
SYSTEMATIC DESIGN THEORY FOR SILICON SOLAR CELLS USING OPTIMIZATION TECHNIQUES

3.1 Introduction

Upper bounds on the open-circuit voltage and efficiency of silicon solar cells can be derived by considering the cell performance as constrained only by detailed balance limitations [15-18]. These bounds are general, in the sense that they are independent of the particular device design and geometry. Such derivations, however, have limited design implications. This work will use a different starting point relating to bounds on solar-cell performance to set up several practical design principles. The analysis to be presented is not based on the thermodynamics of interaction between radiation and matter, and on detailed balance, but rather is focused on the transport of minority carriers in low injection. It is, therefore, less general than treatments based on detailed balance, and it is restricted to one spatial dimension. Our analysis applies, however, for arbitrary doping profiles, drift fields, high-low junctions and includes heavy doping effects; moreover, it provides explicit rules for design.

Design principles follow from three theorems. Two of these, derived here, emphasize recombination in the non-illuminated solar cell. The third is the reciprocity theorem presented in the previous chapter. The theorems exploit linearity. Thus the results hold only under low injection conditions in base and emitter regions. For the most part, the work concentrates on one-dimensional models, but extensions are made to accommodate gridded structures on the back and front surface. In section 3.2, lower bounds on the recombination current are derived as functions of surface and bulk properties. In section 3.3, a theory is presented that allows minimization of the recombination current for any given thickness and (constant) surface recombination velocity. In section 3.4 the model developed is compared with the transparent and quasi-equilibrium models, and bounds on the short-circuit current are derived. The results of the first three sections lead to optimum design principles, presented in section 3.5.

3.2 Lower Bounds of Dark Recombination Current in Quasi-Neutral Regions

In this section we derive upper bounds for the minority-carrier dark recombination current of regions in low injection. These bounds affect the upper limits of the open-circuit voltage and, consequently, of the conversion efficiency. The following analysis focuses on the transport parameters of minority carriers in quasi-neutral regions and derives the absolute bounds on the recombination current by letting the lifetime be limited only by the fundamental recombination mechanisms: radiative and band-band Auger processes. Low injection is assumed throughout this work. This assumption greatly simplifies the problem since the differential equations describing the system become linear.

The analysis presented is valid for any doping profile in one dimension. It accounts for the presence of high-low junctions and of heavy doping effects. Extensions to three dimensions are made when possible. Except where noted, for concreteness we treat n-type silicon; results analogous to those developed below hold for p-type silicon.

The two basic equations, regarding the steady-state minority-carrier (hole) transport and recombination, are

$$J_p = -e\mu P \, dV_p/dx \tag{3.1}$$

$$dJ_p/dx = -e(P - P_o)/\tau . \tag{3.2}$$

In (3.1) V_p is the minority-carrier quasi-Fermi potential referenced to the majority carrier (electron) quasi-Fermi potential (which is assumed independent of position [4]). Also, J_p, P, P_o and τ are the minority current density, carrier density, equilibrium carrier density and lifetime, respectively.

The densities P and P_o are related to V_p by $P = P_o \exp(eV_p/kT)$. Using this equation and setting $u = \exp(eV_p/kT) - 1$, then from (3.1) and (3.2) we can write

$$\frac{d^2u}{dx^2} + \frac{d(DP_o)/dx}{DP_o}\frac{du}{dx} - \frac{u}{L^2} = 0, \tag{3.3}$$

where $L = \sqrt{D\tau}$ is the minority carrier diffusion length. Equation (3.3) holds also in the space-charge region (SCR) of a high-low (H/L) junction since the only assumption used in deriving (3.3) was low injection. This is expected, because, under low injection the electric field there is independent of the voltage across the terminals. Note that u is the fractional excess minority carrier density: $(P-P_o)/P_o$.

In a quasi-neutral region, where the majority electron concentration, N, is equal to the ionized donor concentration, N_{DD}, we characterize P_o in the usual manner:

$$P_o = n_i^2/N_{eff} \tag{3.4}$$

in which

$$N_{eff} = N_{DD} \exp(-\delta E_G/kT). \tag{3.5}$$

In (3.4) n_i is the intrinsic carrier density, while in (3.5) δE_G is the effective band-gap shrinkage (including the degeneracy of majority carriers).

In the SCR of a H/L junction, N(x) (electron density) and $N_{DD}(x)$ are not equal and δE_G is a function of both N(x) and $N_{DD}(x)$, which makes $P_o(x)$ hard to characterize. Additional difficulties enter for compensated material. To overcome this problem, we assume that the SCR is so thin that V_p is nearly flat through it and that the integrated recombination rate through the volume is negligible. This is a realistic assumption since the thickness of the SCR is of the order of the Debye length in the low doped region and is usually a fraction of a micron. Then, we can compress the H/L junction into a point where the coefficients of (3.3) may have step discontinuities. The continuity of u and $DP_o du/dx = -J_p/e$ can serve as boundary conditions connecting the solutions of (3.3) in the quasi-neutral regions on either side of the H/L junction (point). Thus, Po is given by (3.4) except for a number of points equal to the number of H/L junctions. For mathematical simplicity and for other reasons to be discussed, D and τ are also assumed as functions of N_{DD} only. From (3.3) and (3.4) we obtain

$$\frac{d^2u}{dx^2} + \frac{d(D/N_{eff})/dx}{D/N_{eff}} \frac{du}{dx} - \frac{u}{L^2} = 0. \qquad (3.6)$$

Equation (3.6) is the same as the homogeneous part of (13) of del Alamo and Swanson [4]. Note that this equation holds between two successive H/L junctions.

The assumption that, apart from temperature T, D is a function only of N_{DD} is realistic because the ionized impurity scattering is the principal mechanism that determines D; D is a weak function of the fabrication processing at least for dilute doping concentrations. On the other hand, the lifetime depends strongly on fabrication. Since we are mainly concerned here with lower bounds on the recombination current, we focus mainly on fabrication processing that gives the longest lifetimes. Such a lifetime will be a function only of N_{DD}.

If $J_o(x)$ is the saturation value of the recombination current per unit area in the region extending from the surface, located at x=0, to a distance x, as shown in Fig. 3.1, then $J_o(x) = en_i^2R(x)$, where

$$R(x) = \frac{J_o(x)}{en_i^2} = -\frac{1}{en_i^2}\frac{J_p}{u} = \frac{D}{N_{eff}}\frac{du/dx}{u}. \qquad (3.7)$$

Here J_P is positive when it flows in the positive x direction. In words, R(x) is the pre-exponential factor (saturation value) for the

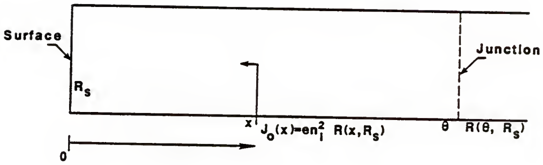

Fig. 3.1 Illustration of the region under study and definition of the function $R(x,R_s)$.

recombination particle current in the interval from 0 to x, normalized with respect to the square of the intrinsic carrier concentration. The introduction of R(x) implies the transport velocity transformation [19], often used in modeling of quasi-neutral regions through the factor, $J_p/u = J_pP_o/(P-P_o)$, where $J_p/(P-P_o)$ is the effective velocity of excess carriers.

Using (3.7) and some manipulation, we transform (3.6) into

$$\frac{dR}{dx} = \frac{1}{D/N_{eff}} - \frac{N_{eff}}{D} R^2, \tag{3.8}$$

which is a first-order nonlinear differential equation of the Riccati form. The boundary condition for (3.8) is

$$R(0) \equiv R_s = -\frac{1}{en_i^2}\frac{J_p(0)}{u(0)} = \frac{1}{n_i^2}\frac{P(0)-P_o(0)}{u(0)} S = \frac{P_o(0)}{n_i^2} S = \frac{S}{N_{eff}(0)}, \tag{3.9}$$

where the subscript s refers to any surface, internal or external, of the solar cell, whose surface recombination velocity is S. The ratio $R_s = [S/N_{eff}]_{x=0}$ completely characterizes the surface for minority-carrier recombination in steady-state. Equation (3.8) strictly holds only in the quasi-neutral regions bounded by H/L junctions. However, because of the previous assumption about the carrier transport in the SCR of H/L junctions, R(x) is a continuous function at the points that define the H/L junction in our model. The continuity of R(x) is important for the analysis that follows.

Our task is to find lower bounds for R(x) and use these bounds to determine the optimum doping profile that minimizes R as a function of R_s and distance from the surface. To do so, a theorem will be presented that derives lower bounds for R(x) as a function of R_s and another bulk parameter R_b, which depends only on N_{eff} and is defined as

$$R_b(x) = \frac{1}{N_{eff}(x)} \left(D(x)/\tau(x)\right)^{1/2} = \frac{D(x)}{N_{eff}(x)L(x)}. \qquad (3.10)$$

Theorem I

$$R(\theta) \geq \min\,[R_b(x), R_s], \quad 0 \leq x \leq \theta \qquad (3.11)$$

where θ is the thickness of the region under study, Fig. 3.1, and the prefix min stands for the greatest lower bound of the set consisting of all values of $R_b(x)$, for $0 \leq x \leq \theta$, plus the value of R_s.

Proof: Let x_m define the point in the closed interval $[0,\theta]$ where R(x) assumes its minimum value. If x_m=0, then $\min[R(x)] = R_s$ and the theorem is proved. If $x_m=\theta$, then using (3.8) and $R(x) \geq 0$, we have

$$\lim_{x\to 0} \frac{dR(x)}{dx} \leq 0 \quad \Leftrightarrow \quad \frac{1}{N_{eff}(\theta)\tau(\theta)} - \frac{N_{eff}(\theta)}{D(\theta)} R^2(\theta) \leq 0$$

$$\Leftrightarrow R(\theta) \geq R_b(\theta) \geq \min[R_b(x)] \geq \min[R_b(x),\, R_s], \quad 0 \leq x \leq \theta.$$

If $0 < x_m < \theta$, then

$$\frac{dR(x_m)}{dx} = 0 \quad \Leftrightarrow \quad \frac{1}{N_{eff}(x_m)\tau(x_m)} - \frac{N_{eff}(x_m)}{D(x_m)} R^2(x_m) = 0 \quad \Leftrightarrow \quad R(x_m) = R_b(x_m).$$

Thus $R(\theta) \geq R(x_m) \geq \min[R_b(x)] \geq \min[R_b(x),\, R_s]$, $0 \leq x \leq \theta$, Q.E.D.

In a similar way one could derive an upper bound for $R(\theta)$:

$$R(\theta) \leq \max[R_b(x),\, R_s], \quad 0 \leq x \leq \theta. \qquad (3.12)$$

In the proof of the above theorem we implicitly assumed the absence of H/L junctions. However, the theorem can be extended to cover any number of such points by using the continuity of $R(x)$ and applying (3.11) and (3.12) to every quasi neutral region between successive H/L junction points.

Theorem I states that if a region terminates ($x=0$) at an ohmic contact, or if $R_s \geq \min[R_b(x)]$, then the minimum value of $R_b(x) = (1/N_{eff})(D/\tau)^{1/2}$ between 0 and θ imposes a lower bound for $R(\theta)$. If $R_s \leq \min[R_b(x)]$, the lower bound becomes R_s. If θ approaches infinity, then theorem I simplifies to $R(\theta) \geq \min[R_b(x)]$ since the condition at the surface has no effect on the recombination current. Theorem I holds for any drift field and H/L junction combination that constitutes the quasi-neutral region of a solar cell. In this sense, the smallest value that R_b can take is a fundamental property of the semiconductor.

We now introduce notation for the extrema of several quantities that will be defined below. Let Y be a parameter that depends only on the doping concentration N_{DD}. Although our main focus in this work will be on the doping concentration, we note that $N = N_{DD}$ in the quasi-neutral region under study, and, for brevity, we use N in the notation that follows to mean the doping concentration as well as the majority carrier concentration. Let Y_m and Y_M be the minimum and maximum values of Y as a function of the doping density. When the letter f is added to the subscript, we mean that the parameter is limited only by fundamental mechanisms (e.g. Auger). Superscripts n and p will denote n-type and p-type material. The value of N corresponding to a particular value, y, of the parameter Y is denoted by N(y). In this notation, R_{bm} is the minimum value of R_b and is larger than or equal to R_{bmf}, which for silicon is limited only by Auger recombination:

$$R_{bfm} = [(DC_A)^{1/2}N/N_{eff}]_m, \tag{1.13}$$

where C_A is the Auger coefficient. The quantity N/N_{eff} is an increasing function of N, while D is a decreasing one. Although there is some disagreement in the literature concerning the actual values of N_{eff} and D as functions of N for $N \geq 10^{18}$ cm^{-3}, the consensual agreement among different models leads to the conclusion that R_{bmf} occurs in the vicinity of $N = 10^{17}$ cm^{-3} for both n and p-type material. For n-type material with $C_A{}^n = 2.8\text{x}10^{-31}$ cm^{6}s^{-1} [20], $R_{bmf}{}^n \approx 1.7\text{x}10^{-15}$ cm^4 s^{-1}. Similarly, for p-type material it turns out that $R_{bmf}{}^p \approx R_{bmf}{}^n \approx 1.7\text{x}10^{-15}$ cm^4 s^{-1}.

In today's silicon cells, where the lifetime for $N < 10^{18}$ cm^{-3} is several times smaller than the Auger limited value, R_{bm} can occur in the vicinity of $N = 10^{18}$ cm^{-3} and have values $R_{bm}{}^n \approx R_{bm}{}^p \approx 3\text{x}10^{-15}$ cm^4 s^{-1} or more.

Applying theorem I to a solar cell having $R_s \geq R_{bmf}{}^n \approx R_{bmf}{}^p$ for the surfaces of both the emitter and the base we derive the following relation for the saturation current

$$J_o \geq en_i{}^2\ (R_{bmf}{}^n + R_{bmf}{}^p) \approx 0.7\text{x}10^{-13}\ \text{A cm}^{-2}, \tag{3.14}$$

holding under any drift or back surface field. In (3.14) and from now on, we take $en_i{}^2 = 20$ A cm^{-6}s (24 °C) to avoid the uncertainty presently existing about effective masses and their temperature dependence. To further reduce J_o, R_s must be reduced below the limiting value of $R_{bmf} \approx 1.7x10^{-15}$ cm^4/s, corresponding to a surface recombination velocity $S = 1700$ cm/sec at $N_{eff} = 10^{18}$ cm^{-3} or $S = 17$ cm/s at Neff $= 10^{16}$ cm^{-3}.

The previous analysis on the lower bounds of R(x) can be extended to three-dimensional quasi-neutral regions under low injection. This is done by replacing J_p in (3.1) and (3.2) with the integrated current density over an equipotential surface (potential in the sense of minority carrier quasi Fermi-potential), at potential V_p. In this case R_b in (3.11) can be replaced by its limiting value

$$A[(1/N_{eff}\tau)_m/(N_{eff}/D)_M]^{1/2} < R_b,$$

where the extrema are taken over an equipotential surface having area A. In the general case these surfaces are not known. Thus, in order to derive practical bounds for R_b, the extrema can be taken over the entire volume of the region under study. The minimum value of A can be inferred either from the morphology of the injecting boundaries or the external surfaces.

Before ending this section, notice that despite the discrepancies in the published data on the band gap-narrowing and minority-carrier diffusivity in heavily doped silicon, the parameter $R_b(x)$, appearing in theorem I, can be determined relatively accurately by experiment, at any doping level. This can be done by measuring the recombination current density, en_iR_b, in a uniformly doped region of thickness much greater than the diffusion length. Similar experiments can also determine the values of the coefficients of the basic equation (3.8),

$1/N_{eff}\tau$ and N_{eff}/D, as was recently pointed out by del Alamo, Swirhun and Swanson [21]. Because of the absence of spatial derivatives of these quantities, we may consider (3.8) to be more useful than its equivalent, (3.6), which requires knowledge of the derivative of the experimentally determined parameter D/N_{eff}.

3.3 Optimization of $R(x, R_s)$

Returning to (3.8), we observe that the right hand side is a single-valued and continuous function of x and R in a quasi-neutral region. Thus, through every point in the (R,x) plane passes only one integral curve [22]. Therefore, by changing only the recombination conditions at the surface from R_{s1} to R_{s2}, leaving the bulk unchanged, we have

$$R(x,R_{s1}) \neq R(x,R_{s2}) \Leftrightarrow R(x,R_{s1}) - R(x,R_{s2}) \neq 0, \qquad 0 \leq x < \infty,$$

where $R(x,R_s)$ is the function $R(x)$ corresponding to surface value of R equal to R_s. Thus,

$$\operatorname{sgn}(R_{s1} - R_{s2}) = \operatorname{sgn}[R(x,R_{s1}) - R(x,R_{s2})] \quad 0 \leq x < \infty, \quad (3.15)$$

where the function sgn is defined by the equation $\operatorname{sgn}(x) = x/|x|$ with x a non-zero real number.

A direct result of Equation (3.15) is the following Lemma.

Lemma 1: If $R(x,R_{s1})$ and $R(x,R_{s2})$ are the normalized recombination currents of the same region having different boundary R values, $R_{s1} > R_{s2}$, then

$$R(x,R_{s1}) > R(x,R_{s2}) \quad , \quad 0 \leq x < R.$$

Using the same arguments as in theorem I, we can extend the above Lemma to a region having any number of H/L junctions. This Lemma leads to the following optimization theorem.

Theorem II: a) Given R_s and θ, the doping profile, $N_{op}(x,R_s)$, that minimizes $R(\theta)$ also minimizes $R(x)$ for $0 < x < \theta$. b) Given R_s, the optimum doping profile, $N_{op}(x,R_s)$, is the one that at any x minimizes dR/dx or, equivalently, $1/N_{eff}\tau - R^2N_{eff}/D$.

From the discussion following theorem I we know that $\lim_{x\to\infty}R_{op}(x,R_s) = R_{bm}$ and $\lim_{x\to\infty}N_{op}(x,R_s) = N(R_{bm})$ for any R_s, where $R_{op}(x,R_s)$ is the minimum value of the normalized recombination current as a function of x and R_s and $N(R_{bm})$ is the doping concentration corresponding to R_{bm}. Also, from theorem II and Equation (3.8) written in the form $dR/dx = (1/N_{eff}t)(1 - R^2/R_b)$,it follows that when $dR_{op}/dx\to 0$, then $R_{op} \to R_{bm}$ and vice versa. Therefore, $R_{op}(x,R_s)$ is a decreasing function of x if $R_s > R_{bm}$, an increasing function of x if $R_s < R_{bm}$, and, for large x, approaches the bulk-limited value R_{bm} (Fig. 3.2). If $R_s = R_{bm}$, then $R_{op}(x,R_{bm}) = R_{bm} =$ constant and $N_{op}(x,R_{bm}) = N(R_{bm})$. Knowledge of $R_{op}(x,R_s=0)$ and $R_{op}(x,R_s=\infty)$, combined with the first part of theorem II yields $R_{op}(x,R_s)$ for any R_s. If $R_s > R_{bm}$, the function $R_{op}(x,R_s)$ is the same as $R_{op}(x,R_s=\infty)$ shifted to the left until it intersects the R axis at R_s (Fig. 3.2). In more analytical terms $R_{op}(x,R_s) = R_{op}(x+x_s,R_s=\infty)$ where $R_{op}(x_s,R_s=\infty) = R_s$. If $R_s < R_{bm}$, the shifting applies to $R_{op}(x,R_s=0)$. To derive the optimum doping profiles for finite values of R_s, we can apply the same translational procedure to the optimum doping profiles $N_{op}(x,R_s=\infty)$ and $N_{op}(x,R_s=0)$, as shown in Fig. 3.3.

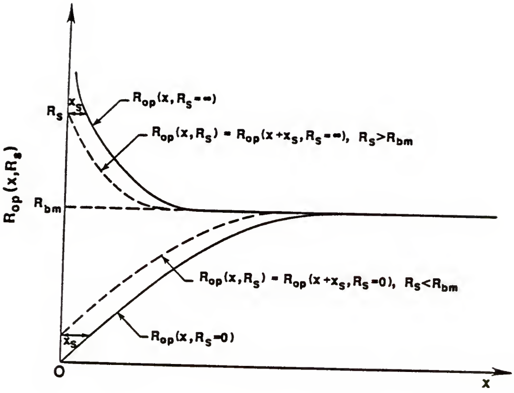

Fig. 3.2 Minimum normalized recombination currents for $R_s = 0$ and $R_s = \infty$ and their relation to $R_{op}(x,R_s)$ for any R_s.

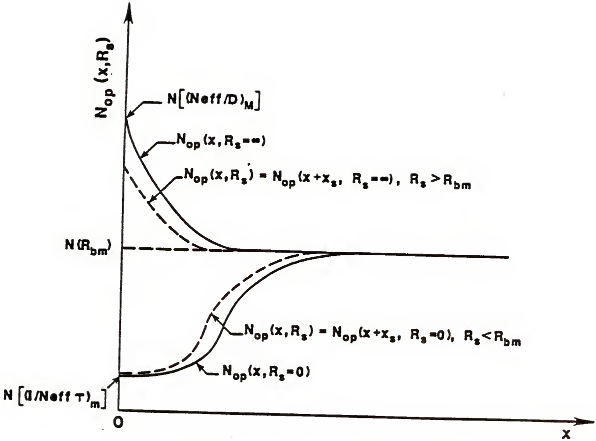
$N_{op}(x,R_s)$
$N[(Neff/D)_M]$
$N_{op}(x,R_s=\infty)$
$N_{op}(x,R_s) = N_{op}(x+x_s,\ R_s=\infty),\ R_s>R_{bm}$
$N(R_{bm})$
$N_{op}(x,R_s) = N_{op}(x+x_s,\ R_s=0),\ R_s<R_{bm}$
$N_{op}(x,R_s=0)$
$N[(1/Neff\ \tau)_m]$
0
x

Fig. 3.3 Optimum doping profiles for $R_s = 0$ and $R_s = \infty$ and their relation to $N_{op}(x,R_s)$ for any R_s.

The second part of theorem II provides a way to obtain $R_{op}(x,R_s)$ and $N_{op}(x,R_s)$. To each value of R corresponds a doping density, $N_{op}(R)$, which minimizes $1/N_{eff}\tau - R^2N_{eff}/D = f(N,R)$. The minimum of $f(N,R)$ over all values of N at a given R will be a function only of R: $f(N_{op}(R), R) = F(R)$. Thus, the differential equation for R_{op} is

$$\frac{dR_{op}}{dx} = F(R_{op}). \tag{3.16}$$

Solution of (3.16) provides $R_{op}(x)$, while $N_{op}(x)$ can be obtained from the function $N_{op}(R)$. A practical way of obtaining R_{op} is to use a finite element method and divide the region by a sequence of points, x_n, into short segments, each of which can be assumed uniformly doped (Fig. 3.4). We obtain the optimum doping, $N_{op}(R_s)$, of the first segment by minimizing $f(N,R_s)$. The boundary condition for the second segment is $R_1 = R_{op}(x_1,R_s)$ which can be obtained from analytical expressions available for uniform regions. Again the optimum doping segment 2, $N_{op}(R_1)$, is obtained by minimizing $(1/\tau N_{eff}) - R_1{}^2(N_{eff}/D)$. Repeating this process yields $N_{op}(R_n)$ as the optimum doping of the (n+1)th segment. From now on we will implicitly use the relation,

$$N[(1/N_{eff}\tau)_m] < N(R_{bm}) < N[(N_{eff})/D)_M].$$

This inequality is realistic for silicon. All published data on band-gap narrowing and mobility indicate that N_{eff}/D is an increasing function of N, at least for N as high as 10^{19} cm^{-3} [4]. On the other hand, several different models for the lifetime imply that $1/N_{eff}\tau$ decreases as N decreases at least for N as low as 10^{17} cm^{-3} [23,24]. Thus $N[(1/N_{eff}\tau)_m] < [(N_{eff})/D)_M]$. From this and from the equality

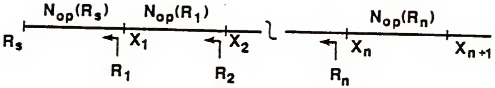

Fig. 3.4 Finite element method for obtaining $N_{op}(x,R_s)$ and $R_{op}(x,R_s)$.

$R_b = [(1/N_{eff}\tau)/(N_{eff}/D)]^{1/2}$, it follows that the value of N that minimizes R_b lies between the value that minimizes $1/N_{eff}\tau$ and the one that maximizes N_{eff}/D.

The discussion following theorem II implies that it is important to know $R_{op}(x,R_s{=}\infty)$, $R_{op}(x,R_s{=}0)$ and the corresponding functions $N_{op}(x,R_s{=}\infty)$, $N_{op}(x,Rs{=}0)$. Dealing first with the case of an ohmic contact, we see that if $R_s{=}\infty$, then minimizing $dR/dx = 1/N_{eff}\tau - R^2N_{eff}/D$ is equivalent to maximizing N_{eff}/D. There is experimental evidence that N_{eff}/D is an increasing function of N, at least for n-type silicon, up to a doping density of 10^{20} cm^{-3} [4]. Therefore, in order to minimize the recombination rates of a region terminated at an ohmic contact, the doping of the layer adjacent to the contact should be high, approaching the solid solubility limit. This could account for the passivation effects of heavily doped polysilicon layers between single crystal silicon and a metal contact. The optimum profile $N_{op}(x,R_s{=}\infty)$ is a continuous and decreasing function of x since, when N drops, $1/N_{eff}\tau$ decreases much faster than does N_{eff}/D, provided $N > N(R_{bm})$. As explained before, $R_{op}(x,R_s{=}\infty)$ is also a decreasing function of x. The same is true from any $R(x,R_s{=}\infty)$ resulting from any doping profile provided the doping is a decreasing function of x and greater than $N(R_{bm})$. This is a consequence of theorem I and of the fact that R_b is an increasing function of N for N $> N(R_{bm})$. Thus, for a doping profile obeying the conditions stated,

$$\frac{dR}{dx} = \frac{1}{N_{eff}\tau} - R^2\frac{N_{eff}}{D} = \frac{1}{N_{eff}\tau}\left(1 - \frac{R^2}{{R_b}^2}\right) < 0. \qquad (3.17)$$

This observation leads to the conclusion that, to minimize recombination currents, a diffusion underneath an ohmic contact should be made deep and should have a surface concentration higher than $N(R_{bm})$.

Consider now a completely passivated surface. Because $R_s = 0$, (3.8) implies that the optimum doping density at the surface is apparently the density that minimizes $1/N_{eff}\tau$: $N_{op}(R_s=0) = N[(1/N_{eff}\tau)_m]$. Note, however, that this doping concentration will not in general produce $R_s = 0$. Rather, this will be some other doping concentration N_s. Thus the optimum doping profile near the surface will consist of a thin layer of concentration N_s followed abruptly by the optimum doping concentration stated above. There is a disagreement in the literature on the value of $N_{op}(R_s=0)$. Rohatgi and Rai-Choudhury [23] locate this doping in the range, 10^{16} - 10^{17} cm^{-3}. For such an $N_{op}(R_s=0)$ the optimum doping and $R_{op}(x,0)$ are derived as previously described. As shown in Fig. 3.3, the doping density increases from $N[(1/N_{eff}\tau)_m]$ to $N(R_{bm})$. This optimum doping profile as an increasing function of x creates a field that pushes minority carriers towards the surface, which is reasonable because near the passivated surface the carriers recombine at a lower rate than that in the bulk. The direction of the field remains unchanged as long as $R_s < R_{bm}$. This should be contrasted with the conventional drift field that pushes minority carriers away from a surface having a high recombination rate, such as an ohmic contact. According to other sources [24], $1/N_{eff}\tau$ is a increasing function of N, at least for doping densities as low as 10^{16} cm^{-3}. Thus $N_{op}(R_s=0)$ will have a small value yielding a material which will be driven into high injection. In this sense, the above analysis, about $N_{op}(R_s=0)$, becomes unrealistic although it is still valid from a mathematical viewpoint. Even in this case, however, the doping near the surface should be kept low to provide good matching between the passivated surface and the semiconductor bulk characterized by R_{bm}. Note that if the lifetime is limited only by radiative and Auger processes, then $1/N_{eff}\tau$ decreases as N decreases and saturates at $[1/N_{eff}\tau]_{mf} = R_a$ for $N < 10^{16}$ cm^{-3}. Here R_a is the radiative recombination constant which for silicon is $R_a = 2.1x10^{-15}$ cm^3/s [18].

In Figs. 3.5 and 3.6 the functions R_{op} and N_{op} are shown, numerically calculated from data provided by Rohatgi and Rai-Choudhury for n-type silicon [23]. From these figures it is seen that $N_{op}(x,R_s=0)$ stays almost constant at $N[(1/N_{eff}\tau)_m]$ until $R_{op}(x,R_s=0)$ approaches R_{bm} and then it sharply increases to values close to $N(R_{bm})$. The same behavior of $N_{op}(x,R_s=0)$ is observed for many different functional dependencies of τ on N. As an implication of this, a practical way of obtaining optimum profiles, when $R_s < R_{bm}$, is to keep N constant and equal to $N[(1/N_{eff}\tau)_m]$ from the surface to a depth where R will become R_{bm}. At this point the doping density abruptly changes to $N(R_{bm})$ (H/L junction) guaranteeing that R will not further increase beyond R_{bm}. In the case of an ohmic contact, both functions R_{op} and N_{op} were calculated by taking R_s as the ratio of the kinetic limit velocity, $S \approx 10^7$ cm/s, and $N_{eff} \approx 10^{18}$ cm^{-3}. The values of R_{op}, N_{op} corresponding to such an R_s are practically the same as $R_{op}(x,R_s=\infty)$ and $N_{op}(x,R_s=\infty)$ which result from setting $R_s = \infty$.

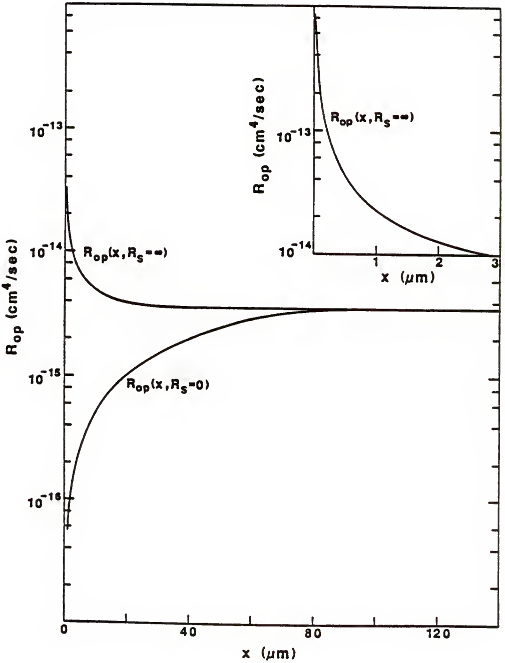

Fig. 3.5 Numerical results for the minimum value of $R(x,R_S)$. The inset emphasizes the behavior near the surface for $R_S = \infty$.

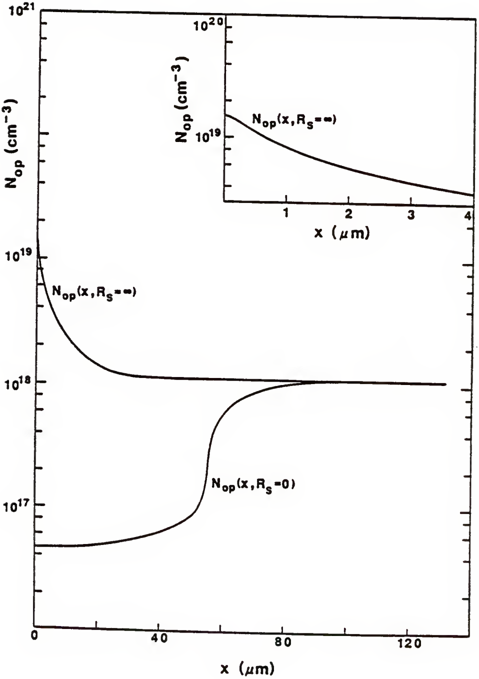

Fig. 3.6 Numerical results for the optimum doping density. The inset emphasizes the behavior near the surface for $R_S = \infty$.

Note that in Fig. 3.6 the optimum doping adjacent to an ohmic contact, which maximizes N_{eff}/D, is approximately $1.5X10^{19}$ cm^{-3}, according to the data of Ref. 23. This is substantially lower than the value of $N_{op}(R_s=\infty) \approx 10^{20}$ cm^{-3}, indicated by del Alamo and Swanson [4].

It is of interest to have analytical expressions that will constrain both $R_{op}(x,R_s=0)$ and $R_{op}(x,R_s=\infty)$ and can be used as closed-form bounds for any $R(x,R_s)$. Starting with $R_s=0$, we show in Appendix A that

$$R_{bm}\tanh(x/l_m) < R_{op}(x,R_s=0) < \min[R_b(N_1)\tanh(x/L(N_1)), R_{bm}\tanh(x/L(N_2))], \qquad (3.18)$$

where l_m is $R_{bm}/(1/N_{eff}\tau)_m$, $L(N_1)$ is the diffusion length when $N = N_1 = N[(1/N_{eff}\tau)_m]$ and $N_2 = N(R_{bm})$.

The lower bound, $R_{bm}\tanh(x/l_m)$ is absolute in the sense that the saturation current, in low injection, of an one-dimensional region having thickness x is greater than or equal to $en_iR_{bm}\tanh(x/l_m)$ for any R_s. The length l_m indicates how fast $R_{op}(x,R_s=0)$ saturates to its bulk-limited value R_{bm}. Using data by Rohatgi and Rai-Choudhury [23] for n-type silicon, $R_{bm} = 3.6x10^{-15}$ cm^4/s, $[1/N_{eff}\tau]_m = 5.1x10^{-13}$ cm^3/s so that $l_m \approx 70\mu m$. A solar cell base made of such a material and having a passivated back surface requires a thickness much less than 70 μm to yield an optimized saturation current less than $en_iR_{bm} \approx 0.7x10^{-13}$ A/cm.

For an ohmic contact $R_{op}(x,R_s=\infty)$ obeys the relation

$$R_{bm}\coth(x/l'_m) < R_{op}(x,R_s=\infty) < \min[R_b(N_3)\coth(x/L(N_3)), R_{bm}\coth(x/L(N_2))], \qquad (3.19)$$

where $l'_m = [(N_{eff}/D)_M R_{bm}]^{-1}$ and $N_3 = N[(N_{eff}/D)_M]$. The length l'_m is the least thickness required to isolate an ohmic contact from the bulk and limit $R_{op}(x,R_s{=}\infty)$ to near R_{bm}. Typical values of l_m' vary from 3 to 10 μm. The bounds derived above can accommodate any R_s by using the translational relation between $R_{op}(x,R_s{=}0)$, $R_{op}(x,R_s{=}\infty)$ and a given $R_{op}(x,R_s)$.

3.4 Relation of the Present Model with the Transparent and Quasi-Equilibrium Models and Optimization of the Short-Circuit Current

Among the approximate models used in the literature to derive analytical expressions for $J_o(x) = en_iR(x)$, two particular models are related with the previous analysis and can themselves yield bounds for the recombination current and internal quantum efficiency.

The transparent model [25], based on the assumption that the minority-current density is independent of position, can be derived from the basic equation (3.8), $dR/dx = 1/(N_{eff}\tau) - R^2(N_{eff}/D)$, by setting $R^2N_{eff}/D >> 1/N_{eff}\tau$ (negligible bulk recombination):

$$\frac{dR}{dx} = -R^2\frac{N_{eff}}{D} \Leftrightarrow -\frac{dR}{R^2} = \frac{N_{eff}}{D}dx \Leftrightarrow \int_{R_s}^{R(x)} d(1/R) = \int_0^x \frac{N_{eff}}{D}dx \Leftrightarrow$$

$$R(x)= \frac{1}{\int_0^x (N_{eff}/D)\ dx' + 1/R_s}. \qquad (3.20)$$

The quasi-equilibrium model [26], based on the assumption that the minority-carrier quasi-Fermi potential V_p is constant, can be derived from (3.8) by setting $1/N_{eff}\tau >> R^2N_{eff}/D$:

$$\frac{dR}{dx} = \frac{1}{N_{eff}\tau} \Leftrightarrow R(x) = \int_0^x \frac{1}{N_{eff}\tau}\, dx' + R_s . \qquad (3.21)$$

This rederivation of both models demonstrates that the transparency assumption underestimates R while the quasi-equilibrium assumption overestimates R. Therefore, the expressions for R derived in the quasi-transparent and quasi-equilibrium model can be used as lower and upper bound for R, respectively:

$$\frac{1}{\displaystyle\int_0^x \frac{N_{eff}}{D}\, dx' + R_s} < R(x) < \int_0^x \frac{1}{N_{eff}\tau}\, dx + R_s . \qquad (3.22)$$

From the discussion in the previous section it follows that the transparent model is accurate only if $x \ll l'_m$ and $R_s > R_{bm}$. This model predicts an optimum doping $N_{op} = N[(N_{eff}/D)_M)]$, which maximizes N_{eff}/D, independently of R_s and x. This was shown to be true for thin regions having ohmic contacts. On the other hand the quasi-equilibrium model is accurate if $x \ll l_m$ and $R_s < R_{bm}$. This model predicts an optimum doping $N_{op} = N[(1/N_{eff}\tau)_m]$, which was shown to be the case for a thin region having a passivated surface. Therefore, these two models converge to the accurate model developed in the previous section for limiting cases.

The transparent model can be used to derive upper bounds for the internal quantum efficiency of a region in low injection. This derivation is based on the reciprocity theorem of Chapter two. Let $m_s(x)$ be the saturation value of the normalized excess minority-carrier density. Because the transparent model underestimates the current, (3.1) implies that the $m_s(x)$ predicted by the transparent model, $m_s^{tr}(x)$, is higher than the actual one.

Thus using (2.9)

$$I_{sc} = e \int_0^\theta C_p(x)\ G(x)\ dx \le e \int_0^\theta m_s^{tr}(x)\ G(x)\ dx \le$$

$$e \int_0^\theta \frac{\int_0^x N_{eff}/D)dx' + 1/R_s}{\int_0^\theta (N_{eff}/D)dx + 1/R_s}\ G(x)\ dx, \qquad (3.23)$$

where G(x) is the generation rate. Relation (3.23) in the form of an equation, instead of an inequality, was used by del Alamo and Swanson [4] in deriving the internal quantum efficiency of a transparent emitter. Here we have shown that the same expression serves as an upper bound for the internal quantum efficiency of any region.

Correspondingly, a first-order quasi-equilibrium model can yield a lower bound for the short-circuit current:

$$I_{sc} = e \int_0^\theta C_p(x)\ G(x)\ dx \ge$$

$$e \int_0^\theta [1 - \int_x^\theta \frac{N_{eff}(x')}{D(x')} \left(\int_0^{x'} \frac{dx''}{N_{eff}\tau} + R_s\right) dx']G(x)dx. \qquad (2.24)$$

From the reciprocity theorem, the zeroth order quasi equilibrium model predicts 100% internal quantum efficiency, which is the same as saying that in a region having a flat V_p from the injecting boundary to the surface, all the photogenerated minority carriers are collected by the junction. Therefore, the flatness of V_p (that is, $dV_p/dx = 0$) is the criterion for optimizing a region with respect to current collection, under low injection conditions. Since lower recombination currents help keep the V_p flat, one could expect that a region having minimized recombination losses, $R(x,R_s) = R_{op}(x,R_s)$, would also have a high internal quantum efficiency. However, optimization of the short-circuit current for a given excitation is a separate problem which leads to a solution different from the one that optimizes $R(x,R_s)$.

The optimum doping concentration for maximum current collection depends on the optical generation profile. If the generation is confined between 0 (injecting boundary) and a point x', then, based on the previous discussion, the optimum doping between the surface (x=0, Fig. 3.1) and x' is the same as $N_{op}(x,R_s)$, $0 < x \le x'$, the doping minimizing $R(x',R_s)$. For the case where the generation function is a delta function applied at x', $G(x) = \delta(x-x')$, the optimum doping between x' and 0 is zero (intrinsic material) if both N_{eff}/D and $1/N_{eff}\tau$ are increasing functions of N. This conclusion is based on the reciprocity theorem previously mentioned. It becomes unrealistic because of the high injection condition that would prevail in such an intrinsic material. Even in high injection, however, low doping concentration would increase the collection probability at x' because of long diffusion lengths. This is all the more true when the field created by the redistribution of the electron-hole plasma helps in separating the photogenerated carriers. Such a low doping concentration could be expected to be optimal if G(x) is uniform between 0 and x. In a base region subjected to solar illumination the generation near the injection boundary (x=0) is much higher than in the bulk. To maximize the current, a drift field towards $x = \theta$ could become necessary. Such a field, though, could conflict with the optimization of $R(x,R_s)$, as presented in the previous section. An optimized combination of these two opposing tendencies will be presented in the last section of this chapter.

In the literature [18] the short-circuit current is usually believed to be an increasing function of the base thickness. This is true for a hypothetical base having unity collection probability at any point. It is also true for any actual uniformly doped base having $R_s \geq R_b$. However, for a base with a passivated back contact, there is an optimum thickness that maximizes the current collection. Let α be the absorption coefficient of monochromatic light, L the diffusion length of the uniformly doped base and R_s=0; then for one optical pass this optimum thickness, θ_{op}, is given, within a good accuracy, by the approximate expression

$$\frac{\theta_{op}'}{L} \approx \frac{1}{1 - L\alpha} \, \mathrm{Ln} \, \frac{2}{L\alpha + (L\alpha)^2} \, . \tag{2.25}$$

This optimum thickness also exists for typical AM spectral conditions and is function only of L [27]. Figure 3.7 shows the ratio θ_{op}/L for an AM2 spectrum and a uniform base having $R_s = 0$. For L in a range of practical interest, θ_{op}/L varies from 1 to 0.85 for one optical pass, and from 0.6 to 0.8 for two optical passes. In the same figure the maximum short circuit current, $(I_{sc})_M$, at the optimum thickness is shown, normalized with respect to the short-circuit current, $(I_{sc})_{un}$, of a uniform base having infinite thickness and the same doping. As

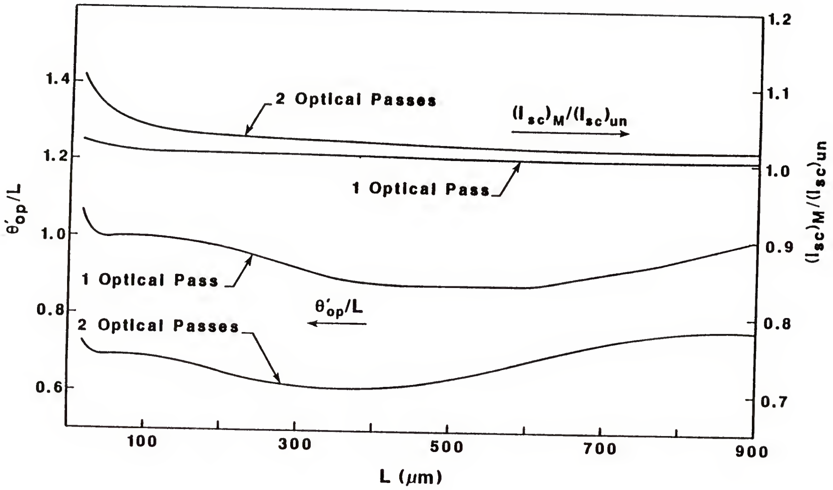

Fig. 3.7 The ratio θ_{op}'/L and the optimized optimum current as functions of the diffusion lenght L for AM2 light and for R_s - 0.

Fig. 3.7 illustrates, use of the optimum thicknesses improves the short circuit current from 4 to 2% for two optical passes, and from 1 to 0.4% for one optical pass, this improvement being a slowly decreasing function of the diffusion length. These are marginal improvements considering the fact that they correspond to completely passivated surfaces ($R_s = 0$). Texturizing the front surface is a more effective way of improving I_{sc} as has been pointed out by the recent developments in high efficiency Si solar cells [28,29]. The design implications of the analysis presented in the last two sections are discussed in the next section.

3.5 Optimum Design

As noted previously, if on both the front and back surface of the cell $R_s = [S/N_{Deff}$ or $S/N_{Aeff}] > R_{bm}{}^n$, $R_{bm}{}^p$, then the saturation current of the cell will be more than $J_o = en_i{}^2\ (R_{bmf}{}^n + R_{bmf}{}^p) \approx 0.7\text{x}10^{-13}$ A cm^{-2}, where this value of J_o and a short-circuit current of 36-40 mA correspond to an open-circuit voltage $V_{oc} \approx 700$ mV. In order for the efficiency to approach theoretical limits [30], V_{oc} should be no less than 750 mV. Such an increase in V_{oc} would require values of R_s much less than R_{bmf} and thicknesses substantially less than the diffusion lengths. This can be done in a shallow diffused emitter by growing quality thermal oxides on the uncovered regions. For such an emitter, the base generation and recombination determine both I_{sc} and V_{oc}.

For a base region, theorem I implies that the conventional back-surface-field system (terminating in an ohmic contact) cannot reduce the base recombination saturation current, $en_i^2R(\theta)$, below $en_i^2R_{bm}$. This condition holds also for a thick base region, by which we mean thickness $\theta > l_m$, independently of the doping profile and of the back surface recombination velocity. Thus, to reduce J_o below its bulk-limited value, $J_o \approx en_i^2R_{bmf} \approx 3.4\times10^{-14}$ A/cm^2, R_s should be less than $R_{bmf} \approx 1.7\times10^{-15}$ cm^4/s and the thickness θ should be less than $l_m = R_{bm}/(1/N_{eff}\tau)_m$. The commonly accepted principle that thinner bases result in lower recombination rates applies to an optimized cell only if $R_s < R_{bm}$. Otherwise, the optimum $R(x,R_s)$ is a decreasing function of x, which implies that the base should be made thick to increase both V_{oc} and I_{sc}.

As noted previously, for bases with well passivated back surfaces, optimization of the saturation current requires a drift field pushing minority carriers to the surface. This field, however, could deteriorate the internal quantum efficiency. Therefore, it is not recommended in the emitter region having high generation rates, or near the junction edge of the base. A good choice for the doping concentration of a base region having $\theta < l_m$ and a well passivated back surface ($R_s \ll R_{bm}$) follows from our previous considerations. This doping concentration, $N[(1/N_{eff}\tau)_m]$, is the one that minimizes $(1/N_{eff}\tau)$. Such a doping concentration would minimize the recombination current and would probably be low enough to result in a long diffusion length and thus high internal quantum efficiency.

For regions on which an electrical contact should be made, three solutions are applicable: ohmic contact, polysilicon (or SIPOS) contact, or a thin tunneling oxide between metal and silicon. If an ohmic contact is chosen, the diffusion under the metal should be made deep and the surface concentration high to maximize the ratio N_{eff}/D. As mentioned earlier, the junction depth needed to reduce $R(x,R_s=\infty)$ near R_{bm} is approximately $[(N_{eff}/D)_M R_{bm}]^{-1} = 3 - 10\ \mu m$. This is in agreement with numerical results of del Alamo and Swanson on Gaussian-profile emitters [4]. The deep diffusion under the ohmic contact provides the added benefit of increasing the reliability by decreasing the possibility of metal spikes penetrating into the base [31]. Moreover, the high doping density near the silicon-metal interface would minimize contact resistance. In contrast to the doping profile under the metal contact, the doping in the uncovered and passivated emitter regions should be lighter and the junction shallow to reduce recombination losses and maximize current collection. Series resistance constraints place a lower limit on emitter doping, so that the optimum doping of the uncovered emitter lies in the range $10^{18} - 10^{19}\ cm^{-3}$. Such an optimized emitter having step discontinuities in doping density and junction thickness is shown in Fig. 3.8.

Polysilicon contacts have shown small values of $R_s (\approx 1.5 \times 10^{-15}\ cm^4/s)$ [32]. This value is almost the same as R_{bmf} and smaller than its present values. Thus, as explained earlier, this contact should be placed as close to the junction as possible. The other option, thin tunneling oxides, has also been used to decrease surface recombination [32]. Since there are no data on the ratio S/N_{eff} characterizing this contact, its use will not be further discussed here. A grid contact and a passivating oxide can also be incorporated

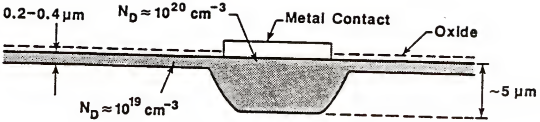
0.2–0.4 μm
$N_D \approx 10^{20}$ cm^{-3}
Metal Contact
Oxide
~5 μm
$N_D \approx 10^{19}$ cm^{-3}

Fig. 3.8 Step geometry of an optimized emitter having doping density discontinuities at the boundaries between the metal-covered and uncovered regions and deeper junctions under the ohmic contacts.

at the back contact of a thin base [34] to reduce the recombination below the bulk limited values. Again, a deep diffusion or a polysilicon contact should isolate the metal at the contact regions from the bulk in order to minimize the overall effective recombination velocity at the back surface.

High collection efficiency demands that care be taken to assure that the minority-carrier quasi-Fermi potential $V_p(x)$ is flat in regions having high generation rates. By flat we mean that the variation across the region must be small relative to kT/e. This condition can be satisfied for shallow emitter regions having doping concentrations in the range, $1\text{-}5\text{x}10^{19}/\text{cm}^3$. As an example, we consider n-type emitters having thicknesses $\approx 0.2\ \mu\text{m}$, constant doping concentration $N_{DD} \approx 5\text{x}10^{19}\ \text{cm}^{-3}$ and $R_s = 3\text{x}10^{-15}\ \text{cm}^4/\text{s}$. Taking $N_{eff}/D = 5\text{x}10^{17}\ \text{cm}^{-5}\ \text{s}$, $\tau = (2.8\text{x}10^{-31}N_{DD})^{-1}$ s, $N_{eff} = 10^{18}\ \text{cm}^{-3}$ and applying the quantum efficiency lower bounds derived in the previous section, we find that the collection probability at the surface is higher than 90%, yielding an overall internal efficiency for the emitter very close to unity. If the doping concentration were $10^{20}\ \text{cm}^{-3}$, the collection probability at the surface would drop to nearly 50%. In an optimized emitter the quasi-equilibrium condition $(dV_p/dx \approx 0)$ should be combined with the requirement that its recombination current, J_{oe}, is much less than the base recombination current, J_{ob}:

$$J_{oe} = en_i^2 \left[\int_0^{x_j} \left(\frac{1}{N_{eff}\tau} \right) dx + R_s \right] < J_{ob},$$

where x_j is the thickness of the quasi-neutral emitter not under metal. This relation implies that, in order to reduce the total cell recombination current below $en_i^2R_{bmf}$, an emitter in quasi-equilibrium having a thickness of 0.2 μm and $N_{eff} \approx 10^{18}/cm^3$ should have $N < 10^{19}$ cm^{-3} and $R_s < 10^{-15}$ cm^4/s.

The requirement for low emitter doping is not necessarily satisfied by assuring that the average value of N_{AA} or N_{DD} is low. In a quasi-equilibrium emitter having an average value of N_{DD} or N_{AA} of 10^{19} cm^{-3} and a surface concentration in excess of 10^{20} cm^{-3}, the recombination at the thin highly doped surface layer can be much higher than the recombination rate in the rest of the emitter because of the quadratic dependence of Auger lifetime on majority carrier concentration. A practical solution for a diffused or implanted emitter would be a rather square profile with surface concentration no more than 10^{19} cm^{-3}.

This doping concentration of the uncovered emitter is consistent with the step geometry of the deep diffusion under the metal shown in Fig. 3.8. If the conventional planar emitter geometry were incorporated, an emitter doping concentration of the order of 10^{19} cm^{-3} could result in a rectifying metal contact. On the other hand, a surface concentration in the uncovered regions in excess of 10^{20} cm^{-3} could make it hard to suppress R_s below 10^{-15} cm^4/s even if quality thermal oxides were grown.

An indication of whether the emitter satisfies the quasi-equilibrium condition is offered by the limit of the internal quantum efficiency at low wavelengths. This is a result of the reciprocity theorem presented in the previous section. Recent data on high efficiency cells indicate that this limit is around 60-70% even with passivating oxides present [35]. The losses thus implied could result from the high surface impurity concentration characterizing the emitters of these cells. This observation points to the direction of low doping in the uncovered emitter regions.

As was mentioned in the previous section, for a base with a passivated back surface there is an optimum thickness, θ_{op}', that maximizes the collected current. Let θ_{op} be the thickness that maximizes the product $V_{oc}I_{sc}$. If the emitter recombination exceeds that of the base, then $\theta_{op} = \theta_{op}'$. This is the case because when $5x10^{-13} < J_o < 5x10^{-14}$ A/cm^2 and Isc ≈ 36-40 mA/cm2, then the product $V_{oc}xI_{sc}$ is about 27 times more sensitive to I_{sc} than it is to $J_o = J_{oe} + J_{ob}$, and the sensitivity of J_{ob} to a change $\delta\theta$ in the uniform base thickness is at most $\delta\theta/\theta$%. However, in a cell with an optimized emitter, where the base determines both J_o and I_{sc}, θ_{op} could be significantly less than θ_{op}'. Figure 3.9 presents the ratio θ_{op}/L for a uniform base having $R_s = 0$ and two different values of R_b, at AM2 spectral conditions. As shown, this ratio is a decreasing function of L, the number of optical passes and it is relatively insensitive to R_b. As expected $\theta_{op} < \theta_{op}'$. Figure 3.10 illustrates the maximum value, $(V_{oc}I_{sc})_M$, that the product $V_{oc}I_{sc}$ assumes at θ_{op}. This maximum is shown normalized with respect to the product, $(V_{oc}I_{sc})_{un}$, of a uniform and infinitely thick base having the same doping. As can be seen, for L > 70 μm the normalized $(V_{oc}I_{sc})_M$ is almost independent of L and R_b; in other words, it is almost independent of the doping density. This observation leads to the conclusion that the problem of

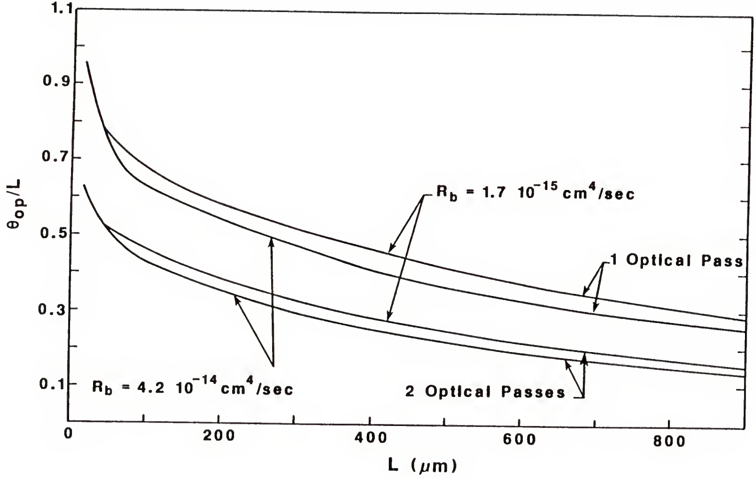

Fig. 3.9 The ratio θ_{op} as a function of L for two values of R_b and for R_s =0 (AM2 light).

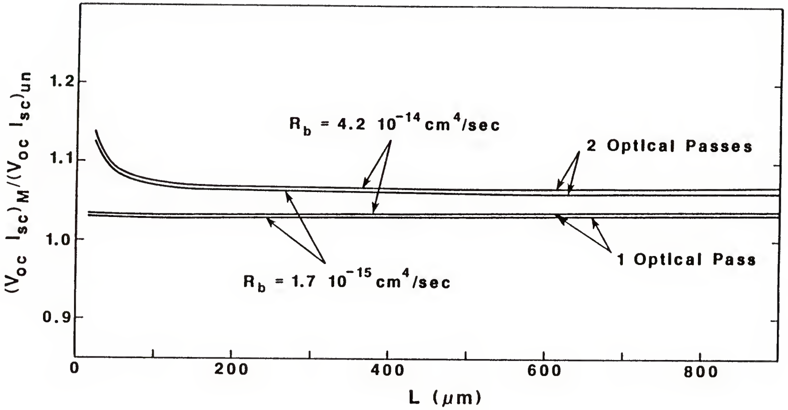

Fig. 3.10 The normalized optimum value of the product V_{oc} I_{sc} as a function of L for two values of R_b and for R_s = 0 and AM2 light.

finding the optimum doping and thickness which will maximize $V_{oc}I_{sc}$, for a uniform base, consists of two autonomous problems. First, optimum doping is determined by requiring that $V_{oc}I_{sc}$ be maximized for a uniform and infinite base, and then the optimum thickness can be inferred from Fig. 3.9. Figure 3.10 also shows that the presence of a back reflector and a passivated back contact will improve the efficiency by about 6% (or at least 1% absolute) if the right thickness, θ_{op}, is chosen. The data by Rohatgi and Rai-Choudury [23] for n-type silicon imply an optimum doping, 2.3×10^{16} cm^{-3} and an optimum thickness $\theta_{op} \approx 150$ μm for one optical pass, or $\theta \approx 100$ μm for two optical passes.

So far in this analysis the derivation of the limiting recombination losses was restricted to one-dimensional regions. In the previous chapter, however, we pointed out that in shallow junction structures, especially in those having passivated surface, the base recombination current per unit area is about the same as the recombination current density in the one-dimensional counterpart. Therefore, the conclusions regarding minimization of recombination losses also hold for three-dimensional solar cells, like the ones with texturized front surface to enhance light absorption [28, 29].

3.6 Concluding Remarks

The optimization theory presented was based on three parameters that determine the ultimate performance of the cell. These parameters are R_s, θ, and $1/N_{eff}\tau$, the first two of which are characterized by two limiting values, R_{bm} and l_m. It was shown that in order to reduce the saturation current below $en_i^2R_{bm}$, R_s should be much less than R_{bm} and θ less than l_m. If these conditions are satisfied, the optimum doping lies in the vicinity of $N[(1/N_{eff}\tau)_m]$. The fundamentally minimum value of the parameter $1/N_{eff}\tau$ sets the upper bound on efficiency. The dependence of the fundamental limit minority-carrier lifetime on the doping concentration is still debated in the literature. For $N > 10^{17}$ cm^{-3}, this limit is probably determined by Auger recombination. For lighter doping, however, unavoidable defects induced by processing and the addition of impurities can lower the lifetime well below the value limited only by Auger and radiative mechanisms [36]. Of the same importance is the lowest possible value of the parameter $R_s = S/N_{eff}$ characterizing the surface. Further research is needed to investigate the fundamental mechanisms, if any, that limit the value of this parameter.

CHAPTER FOUR
LIFETIME AND DIFFUSIVITY DETERMINATION FROM FREQUENCY-DOMAIN TRANSIENT ANALYSIS

4.1 Introduction

In this chapter we propose a new method to measure the minority-carrier lifetime and diffusion coefficient in the base of a solar cell. We also point out that several time-domain experiments used to extract device parameters like lifetime, diffusion coefficient and recombination velocity, can be viewed from a different than the conventional perspective. In methods such as the electrical short-circuit current decay [37] and photocurrent decay [38] the lifetime is determined by waiting until the response drops well below its initial value and then observing the almost exponential decay of the signal. In the Haynes-Shockley experiment the carrier lifetime and diffusivity are determined by monitoring the time dependence of the peak value and the width of the minority-carrier pocket injected by light. Here we demonstrate that in these experiments we can exploit the full response instead of focusing on a particular part or point of the curve. This is done by taking the Fourier transform of the pulse response of the device and then comparing it to closed form expressions (transfer functions) relating input and output in the frequency domain. By fitting the entire curve for the amplitude and the phase of the Fourier transform with available analytical expressions we increase the accuracy and reliability of the method. The next two sections demonstrate the technique applied on the pulsed photocurrent and a variation of the Haynes-Shockley experiment. Throughout this work we assume low-injection conditions so that input and output are linearly related and Fourier transform can be applied to derive the frequency response of the device.

4.2 Analytical Formulation

Consider a one-dimensional diode where the quasi-neutral base is much longer compared with emitter and space-charge region combined and is excited by uniformly absorbed light pulses. As shown in Appendix B, the short-circuit current in the frequency domain is $J_{sc}(\omega) = e\, G(\omega)\, F(\omega)$, where $G(\omega)$ is the spatially uniform generation rate in the frequency domain, and $F(\omega)$ is given by

$$F(\omega) = \frac{L' \,[\sinh(W/L')+(SL'/D)\cosh(W/L')-SL'/D]}{\cosh(W/L')+(SL'/D)\sinh(W/L')} \,. \qquad (4.1)$$

In (4.1) L' is the complex diffusion length $L'=L/(1+j\omega\tau)^{1/2}$, L is the static diffusion length $L=(D\tau)^{1/2}$, D is the diffusion coefficient, τ is the lifetime, S is the back surface recombination velocity, W is the base thickness and e is the elementary charge. Therefore, when a very narrow pulse of uniformly absorbed light excites the cell ($G(t)=\delta(t)$ or $G(\omega)$=constant), the Fourier transform of the short-circuit pulse response current $J_{sc}(t)$ is the same function of the frequency as $F(\omega)$ in (4.1). If $G(t)$ is not a delta function, then to obtain $F(\omega)$ we have to normalize the Fourier transform of the current by dividing $J_{sc}(\omega)$ by the Fourier transform of the input $G(\omega)$. For a long base diode, $W/L > 4$, $J_{sc}(\omega)$ is proportional to $(1+j\omega\tau)^{-1/2}$ and the plot of $F(\omega)$ in a log-log scale is frequency-independent for $\omega < 1/\tau$, a straight line with a slope of -1/2 for $\omega >> 1/\tau$ and the intercept of the two lines is the corner frequency which depends only on the lifetime, $\omega_c=1/\tau$. If the base is not long enough, additional measurements are needed to extract τ, D and S. However, for $W/L > 1.5$ the intercept depends primarily on the lifetime and can still be used for a first approximation of τ.

An alternative experiment is to excite the device using strongly absorbed light pulses striking from the back (after opening a window in the back contact) and then monitor the current collected by the shallow front emitter junction. This is a variation of the well known Haynes-Shockley experiment the difference being that the minority carriers move vertically and in one dimension, instead of laterally. If G' is the generation rate, per unit area at the back surface, then, as shown in Appendix B, the solution of the continuity equation is $J_{sc}(\omega) = e\, G'(\omega)\, F'(\omega)$, where

$$F'(\omega) = \frac{1}{\cosh(W/L') + (SL'/D)\sinh(W/L')} \quad . \qquad (4.2)$$

From (4.2) we see that when $\exp(-2W/L) << 1$ and $S < D/L$ then $F'(\omega)$ is proportional to $\exp(-W/L')$. Thus, if we plot the logarithm amplitude of $F'(\omega)$ versus $\omega^{1/2}$, for $\omega >> 2/\tau$ we obtain a straight line with a slope equal to $-W(2D)^{-1/2}$ and an intercept with the low-frequency limit at $(\omega_c')^{1/2} = (2/\tau)^{1/2}$. The same is true also for the slope of the phase plotted versus $\omega^{1/2}$. Note that D and τ are independently calculated by observing different portions of the plot of $F'(\omega)$ vs ω. For higher values of S the slope and the intercept will slightly change, but they still depend primarily on D and τ and can still be used for a first estimate of D and τ.

For a more accurate determination of τ, D and S one can combine the uniformly absorbed light and strongly absorbed light measurements. First, from the corner frequency of the amplitude of $J_{sc}(\omega)$, for the uniformly absorbed light, we derive an approximate value for τ. Then, from the slope of the amplitude and the phase of $J_{sc}(\omega)$, for the strongly absorbed light, we derive a first approximation for D. To derive S we can measure the quantum efficiency of the device for strongly absorbed light shining from the back surface. This quantum efficiency is a sensitive function of S and is given by $F'(0)$. After having made a first approximation for τ, D, and S, a more accurate determination can be obtained by fitting $J_{sc}(\omega)$ for the uniformly and the strongly absorbed light with the analytical expressions for $F(\omega)$ and $F'(\omega)$ as given by (4.1) and (4.2).

4.3 Demonstration of the Method and Discussion

A p-type base Si cell was mounted, with the emitter facing down, on a TO-5 header after its back contact was removed except for a small dot near the edge to bond a wire. The cell was cut from a 2 x 2 cm^2 cell with base resistivity of 0.16 ohm-cm. The base doping, as measured by the capacitance method, was $1.22 \pm 0.04 \times 10^{17}$ cm^{-3}. The base thickness was 309 ± 2 μm. The short-circuit current in the time domain was measured by monitoring the voltage across a 50-ohm resistor connected in series with the cell, through the Tektronix 7D20 digitizer. The Fourier transform was performed on the digital output of the digitizer. As a light source the GR 1531-AB stroboscope was used. Long-pass ($\lambda \geq 1.1$ μm) and low-pass ($\lambda \leq 0.6$ μm) optical filters were used to create the uniformly absorbed and strongly absorbed light pulses. The light pulses were also measured with a p-i-n Si detector for the strongly absorbed light and with a Ge detector for the uniformly absorbed light. To normalize the response, the Fourier transform of the short-circuit current was divided by the Fourier transform of the light pulses. The amplitude and the phase of the normalized frequency domain response are shown in Figs. 4.1 and 4.2 for the uniformly absorbed light, and in Figs. 4.3 and 4.4 for the strongly absorbed light. The quantum efficiency for the strongly absorbed light shining from the back contact, as measured using a He-Ne laser, was about 0.7 %. Using the procedure described in the previous section the best fit in Figs. 4.1 and 4.2 was found for τ_n = 12 ± 1 μs, the best fit in Figs. 4.3 and 4.4 was found for D_n = 17 ± 1 cm^2/s, and from the quantum efficiency $S=3.5\times10^4 \pm 5\times10^3$ cm/s. The exact value of S is not important for determining τ_n and D_n since a change in S from 3×10^4 to 4×10^4 cm/s has a negligible effect on the ratios $F(\omega)/F(0)$ and $F'(\omega)/F'(0)$. The effect of the lifetime varying from 11 to 12 μs is also negligible in the determination of D_n.

We believe that the value of the minority-carrier diffusion coefficient derived above is a reliable one. This is supported by the good agreement between the experimental results and theoretical expressions for the strongly absorbed light and by the fact that the

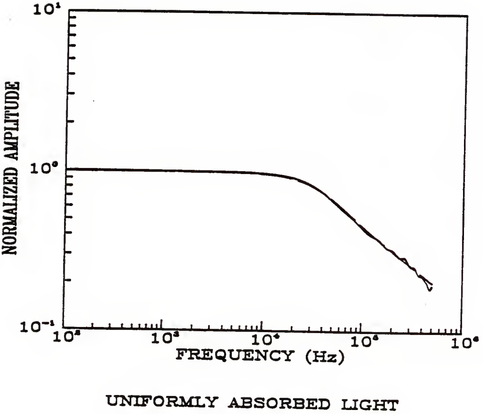

Fig. 4.1 Normalized amplitude of the frequency-domain response for uniformly absorbed light. The solid line is the amplitude of the measured current in the frequency domain. The broken line is the amplitude of the ratio $F(\omega)/F(0)$ for $\tau_n = 12\mu s$, $D_n = 17\ cm^2/s$ and $S = 3.5x10^4\ cm/s$.

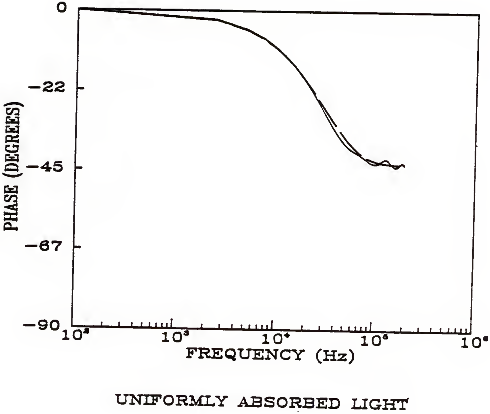

Fig. 4.2 Phase of the normalized frequency-domain response for uniformly absorbed light. The solid line is the phase of the measured current in the frequency domain. The broken line is the phase of the ratio $F(\omega)/F(0)$ for $\tau_n = 12\mu s$, $D_n = 17$ cm^2/s and $S = 3.5\text{x}10^4$ cm/s.

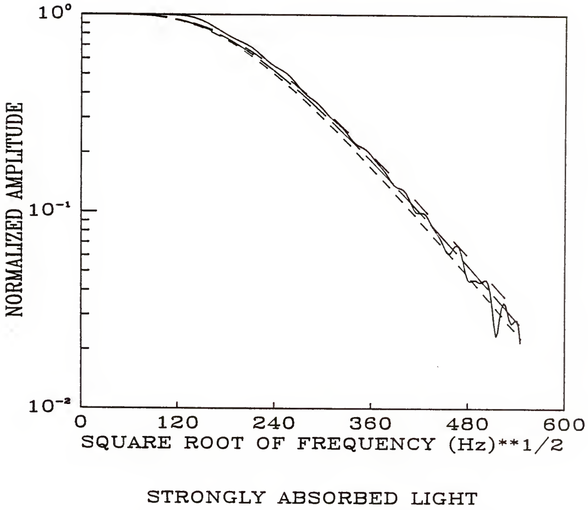

Fig. 4.3 Normalized amplitude of the frequency-domain response for strongly absorbed light shining from the back. The solid line is the amplitude of the measured current in the frequency domain. The broken lines are the amplitude of the ratio $F'(\omega)/F'(0)$ for $D_n = 17$ (– – –), $D_n = 18$ (—— —— ——) and $D_n = 19\ cm^2/s$ (— — —). Here τ_n was set at 12 μs and S at 3.5×10^4 cm/s.

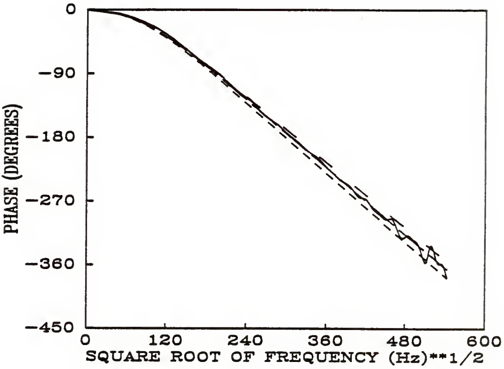

STRONGLY ABSORBED LIGHT

Fig. 4.4 Phase of the normalized frequency-domain response for strongly absorbed light shining from the back. The solid line is the phase of the measured current in the frequency domain. The broken lines are the phase of the ratio F'(ω)/F'(0) for D_n = 16 (– – –), D_n = 17 (—— —— ——) and D_n = 18 cm^2/s (— — —). Here τ_n was set at 12 μs and S at $3.5x10^4$ cm/s.

phase and the amplitude yield values for D_n less than 10 % apart. Also the corner frequency ω_c' in Fig. 4.3 corresponds to a lifetime $\tau_n \approx 2/\omega_c'$ which is about the same as the lifetime derived from Fig. 4.1. The value $D_n = 17 \pm 1$ cm^2/s or $\mu_n = 666 \pm 39$ cm^2/Vs at 23 °C for minority electrons and a doping density $N_A = 1.22 \times 10^{17}$ cm^{-3} , is within experimental error equal to the majority electron mobility of 696 cm^2/Vs for the same donor doping density as reported by Thurber et al [39]. This verifies the results reported by Dziewior and Silber [40] and by Neugroschel [41].

The frequency-domain transient analysis method can also be used to characterize bulk wafers by depositing a Schottky contact on the front surface and a gridded ohmic contact on the back surface and then shining both the strongly and the uniformly absorbed pulsed light from the back surface. It can also be used in dark devices by using electrical pulses, as in the electrical short-circuit current decay. In Si devices, however, the turn-on part of the response is determined by space charge region, emitter, and series resistance parasitics. Therefore, only the turn-off of the response can be considered, which corresponds to exciting the device by a step input. The amplitude of the Fourier transform of the step function drops as $1/\omega$ and, consequently, the input might not have enough power to excite higher modes in the device, thus, reducing the sensitivity of the method at high frequencies. This also points out the advantage of using light pulses for excitation since there are no, at least for some frequency range, space-charge region and resistance limitations, and narrow pulsed light sources are readily available.

The lifetime and the diffusion coefficient could also be extracted from the Haynes-Shockley experiment by fitting the time-domain response with theoretical expressions. The effect of τ and D, however, spreads over the entire time-domain pulse response and the fit would be a two parameter fit. In the method demonstrated here τ and D affect different parts of the curve and the two parameters can be separated. An additional drawback of the time-domain fitting is mathematical complexity: the pulse response of the system would involve an infinite series of analytical functions which would have to be convoluted with the input pulse.

The Fourier transform method introduced here can be applied to several other transient techniques such as photoluminescence decay or light induced open-circuit voltage decay. In the latter, care should be taken that the terminal voltage is low enough to assure linearity between input and output, and that the capacitance and recombination in the space charge region is taken into consideration.

So far in Chapters two, three and four we implicitly assumed that when a p/n junction is short-circuited and illuminated the minority-carrier density at the space-charge region edge of the base is zero. The validity of this assumption is discussed in Appendix C.

4.4 Conclusions

In conclusion we have proposed and demonstrated a new method, frequency-domain transient analysis (FDTA), for measuring lifetimes and diffusion coefficients. The method utilizes the whole time-domain transient response and through Fourier transform gives the frequency response of the device. We showed that FDTA is more plausible and accurate than other time-domain techniques. The diffusion coefficient and lifetime in a p-type 0.16 ohm-cm base were measured and found to be 17 ± 1 cm^2/s and 12 μs, respectively. The method can be applied to characterize solar cells, photodetectors or bulk wafers. Extension to devices operating in the dark is possible although problems arising from emitter or space-charge-region parasitics can reduce the sensitivity of the method at high frequencies.

CHAPTER 5
NUMERICAL SOLUTIONS, PHYSICAL INTERPRETATIONS, AND ANALYTICAL MODELS FOR AMORPHOUS SILICON P/I/N SOLAR CELLS

5.1 Introduction

This chapter presents contact-to-contact computer solutions of the a-Si:H p/i/n solar cell and treats these as computer experiments designed to reveal the approximations and insight needed for the development of analytical models. A FORTRAN 77 program was written based on the Poisson equation and the hole and electron continuity and current equations. We ran this program on a Harris 800 computer, studying many aspects of internal variables such as electric field, carrier densities, current densities, and recombination rates versus position, terminal voltage and photon flux density. Strongly absorbed, weakly absorbed and AM1.5 light were studied to gain the insight needed for the analytical modeling. Based on our physical interpretation of the computer experiments, we propose analytical and equivalent-circuit models which support each other and which help explain the physical origin of interdependencies among such variables as quantum efficiency, electric-field and recombination-rate nonuniformities and their relations to the current-voltage characteristic. We mathematically treat the concept of the limiting carrier by separating the current into photocollected and back-injection components and conclude that the limiting carrier is the carrier with the smaller photocollected current. This concept is also treated in our critical review of the literature where we employ reasoning in the time domain.

This Chapter consists of five sections. Section 2 presents the parameters and assumptions used for the numerical simulations. In section 3 the numerical solutions are interpreted, the concept of the limiting carrier is emphasized and a new equivalent-circuit model is developed. Section 4 proposes analytical models that express current,voltages and recombination rates as functions of material properties such as lifetime, mobility and absorption coefficients. In the last section, we review selected papers concerning the modeling of amorphous p/i/n devices.

All numerical and analytical modeling is done for the steady state.

5.2 Numerical Modeling

Following Hack and Shur [42] we assume an exponential distribution for acceptor, $g_A(E)$, and donor, $g_D(E)$, type states in the mobility gap, as shown in Fig. 5.1:

$$g_A(E) = g_A \exp[(E-E_{mc})/E_A] \tag{5.1(a)}$$

$$g_D(E) = g_D \exp[-(E-E_{mc})/E_D]. \tag{5.1(b)}$$

In (5.1), E_A and E_D are the characteristic energies of the acceptor and donor type traps. In amorphous silicon the dominant recombination mechanism is Shockley-Read-Hall (SRH) recombination through the gap states [43]. Assuming a and zero temperature distribution function for the trapped carriers (this assumption is

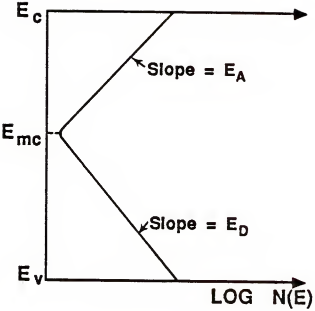

Fig. 5.1 Defect states spectrum of an a-Si:H solar cell.

justified since E_A and E_D are several times the thermal voltage kT) we derive the following closed form expression for the recombination rate:

$$R = (pn-n_i^2)\ C\ U_{th}\ \sigma_n\ \{g_A\ E_A\ [N_c^{-1}\exp((E_c-E_{mc})/E_A)((n+Cp)/N_c)^{kT/E_A-1} -$$
$$\exp((E_v-E_{mc})/E_A)\ C^{kT/E_A} + g_D E_D\ [N_v^{-1}\exp((E_{mc}E_v)/E_D)((n+Cp)/N_v)^{kT/E_D-1}$$
$$\exp((-E_c+E_{mc})/E_D)\ C^{\ kT/E_D}\ N_c^{-1}((p+nC)/N_c)^{-kT/E_D-1}]\}. \tag{5.2}$$

Here, U_{th} is the thermal velocity of an electron, σ_n is the capture cross section of a neutral trap and C is the ratio σ_c/σ_n where, σ_c is the cross section of a charged trap. Further, n and p are the carrier densities and N_c and N_v the effective density of states for electrons and holes respectively. The intrinsic carrier density is given by $n_i = [N_c\ N_v\ \exp(-E_g/kT)]^{1/2}$ where Eg is the band gap. Under the same assumptions regarding density of states and occupation statistics, the expression for the trapped electron density becomes

$$n_t = g_A\ E_A\ [\exp((E_c-E_{mc})/E_A)(n/N_c)((n+Cp)/N_c)^{kT/E_A-1} +$$
$$+ \exp(-(E_{mc}-E_v)/E_A)(C_p/(n+Cp))((p+n/C)/N_v)^{-kT/E_A}\ ], \tag{5.3(a)}$$

while for the trapped holes becomes

$$p_t = g_D\ E_D\ [(p/N_v)\exp((E_{mc}-E_v)/E_D)((n+Cp)/N_v)^{kT/E_D-1} +$$
$$\exp((-E_c+E_{mc})/E_D)(nC/(nC+p))((n+p/C)/N_c)^{-kT/E_D}]\}. \tag{5.3(b)}$$

The expression for the total charge density is

$$Q(n,p) = e(p_t - n_t + N_D - N_A), \tag{5.4}$$

where e is the elementary charge, and N_D - N_A is the net ionized doping density.

The cell, Fig. 5.2, is assumed to have an overall thickness of 0.6 μm. The doped layers have a thickness of 100 Å and the light enters through the P^+ layer. The boundary condition at the ohmic contact on the P^+ layer is that the majority carrier (hole) density remains constant at $p(0) = 4.6\mathrm{x}10^{12}$ cm^{-3} while the minority carriers (electrons) see the contact as a surface characterized by a recombination velocity equal to $S_n = 5\mathrm{x}10^6$ cm/s (kinetic limit velocity for electron in single-crystal silicon). Similarly the boundary condition at the N^+ layer is that the electron density stays constant at $N(W) = 10^{16}$ cm^{-3} while holes see a recombination velocity of $S_p = 2\mathrm{x}10^6$ cm/s. To correlate the doping density, the trap density and the majority carrier density at the ohmic contacts, we have assumed that in equilibrium the net charge density at the ohmic contact is zero. Taking the density of ionized dopants in the heavily doped layers to be 10^{19} cm^{-1} forces g_D in the P^+ layer to be $g^+ = 2.5\mathrm{x}10^{16}$ cm^{-3} eV^{-1}. In the N^+ layer $g_A = g^+ = 4.2\mathrm{x}10^{16}$ cm^{-3} eV^{-1}. In the intrinsic layer the values of g_A and g_D were $g_A = g_D = 0.2\mathrm{x}10^{16}$ cm^{-3} eV^{-1}.

Two cases of optical monochromatic excitation are considered. In the first, the absorption coefficient $\alpha = \alpha(\lambda)$ is high ($\alpha = 2\mathrm{x}10^5$ cm^{-1}) and the light is strongly absorbed near the front surface. In the second case the absorption coefficient is small ($\alpha = 2\mathrm{x}10^3$ cm^{-1}), the light is reflected once on the back surface. The reflection coefficient is 0.8, and the generation rate is almost uniform

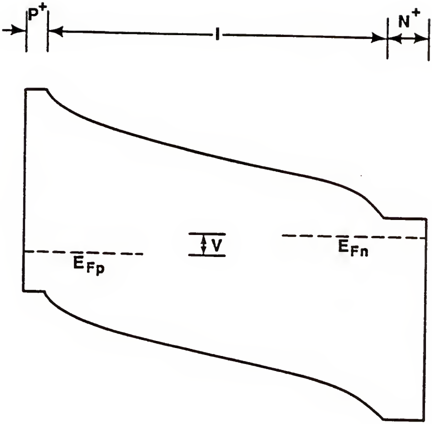

Fig. 5.2 Band diagram of an a-Si:H solar cell.

throughout the cell. In addition, the effect of AM1.5 light shining through the P^+ layer is studied and related to the monochromatic excitations. The equations used in the numerical simulation were:

$$J_n = \mu_n\, n\, (dF_n/dx) \qquad (5.5)$$

$$J_p = \mu_p\, p\, (dF_p/dx) \qquad (5.6)$$

$$dJ_n/dx = -\, e(G - R) \qquad (5.7)$$

$$dJ_p/dx = e(G - R) \qquad (5.8)$$

$$dE/dx = Q/\epsilon \qquad (5.9)$$

$$d(E_i/e)/dx = E. \qquad (5.10)$$

Equations (5.5) and (5.6) express the electron and the hole current in terms of the gradient of the respective quasi-Fermi levels. Equations (5.7) and (5.8) are the continuity equations for electrons and holes, (5.9) is the Poisson's equation and (5.10) expresses the electric field as the gradient of the electrostatic potential on the electron energy scale. The standard relations, $n = n_i \exp((F_n - E_i)/kT)$ and $p = n_i \exp((E_i - F_p)/kT)$, connect F_n and F_p with the rest of the equations.

The system of equations (5.5)-(5.10) was solved using Newton's method. The results appear in the next section. We conclude this section by presenting a list of the parameters used in the numerical simulation.

Table 1.
List of Parameters Used in Numerical Modeling

Electron mobility	$\mu_n = 10\ cm^2/(Vs)$
Hole mobility	$\mu_p = 1\ cm^2/(Vs)$
Acceptor states preexponential factor	$g_A = 0.2x10^{16}\ cm^{-3}eV^{-1}$
Donor states preexponential factor	$g_D = 0.2x10^{16}\ cm^{-3}eV^{-1}$
Acceptor states characteristic energy	$E_A = 0.053\ eV$
Donor states characteristic energies	$E_D = 0.088\ eV$
Energy of gap states minimum	$E_{mc} = 0.65\ eV$
Mobility gap	$E_g = 1.72\ eV$
Effective density of states	$N_c = N_v = 10^{19}\ cm^{-3}$
Capture cross section x thermal velocity (neutral trap)	$= 10^{-11}\ cm^3s^{-1}$
Capture cross section x thermal velocity (charged trap)	$= 10^{-9}\ cm^3s^{-1}$

5.3 Interpretation of the Numerical Results

Figure 5.3(a,b) presents the numerical results on the electric field magnitude profiles at short-circuit conditions as a function of the photon flux density of strongly and weakly absorbed light. We can see that the field is much more disturbed from its equilibrium value for uniform absorption than it is for strong absorption. For weakly absorbed light the field has a deep minimum near the N^+ layer, while for strongly absorbed light the field is relatively uniform with its minimum shifted towards the P^+ contact. Figure 5.4(a,b) shows the effect an applied forward bias has on the field profile. For strong absorption the applied voltage reduces the field mainly in the

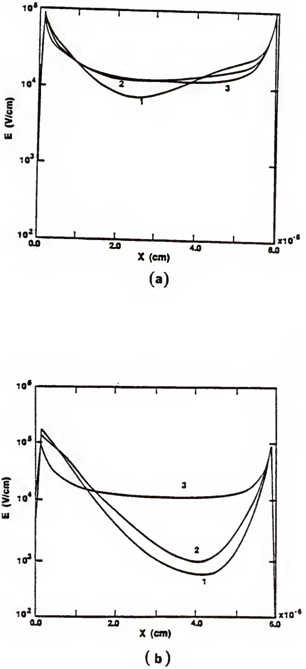

Fig. 5.3 Electric field profiles at short circuit as functions of the photon flux density. (a) Strongly absorbed light, curves 1, 2, 3 correspond to F = 10^{17}, 10^{16}, 0 cm^{-2}s^{-1}, respectively. (b) Uniformly absorbed light, curves 1, 2, 3 correspond to F = 10^{18}, 10^{17}, 0 cm^{-2}s^{-1}, respectively.

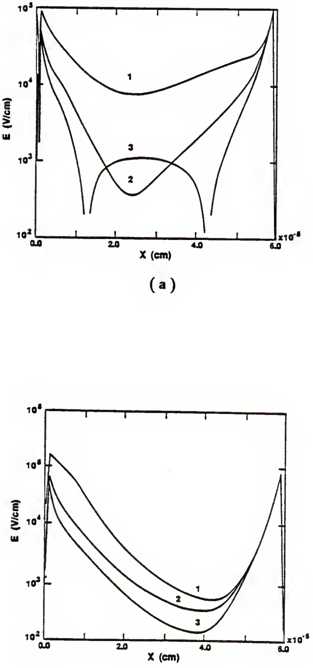

(a)

(b)

Fig. 5.4 Electric field profiles as functions of forward bias at short-circuit, 1, maximum-power, 2, and open-circuit, 3. (a) Strongly absorbed light, $F = 10^{17}$ $cm^{-2}s^{-1}$, V = 0, 0.725, 0.927 Volts (1, 2, 3, respectively.). (b) Uniformly absorbed light, $F = 10^{18}$ $cm^{-2}s^{-1}$, V = 0, 0.760, 0.918 Volts (1,2,3 respectively).

intrinsic layer; large voltages reverse the direction of the field in the bulk of the i-layer. For uniform absorption the field drops mainly at the p/i interface and its minimum value is only slightly affected. In both cases the position of the minimum is relatively bias independent.

To understand the effect the generation profile has on the electric field, we have to take into account the difference between the electron and the hole collection length ($l_c = E\mu\tau$). In this model electrons have higher mobility ($\mu_n = 10$ cm^2/Vs) than holes ($\mu_p = 1$ cm^2/Vs). In addition, the electron lifetime is higher than the hole lifetime because there are more hole traps than electron traps ($E_A < E_D$). Because of the longer electron collection length and under uniform excitation, more photogenerated electrons arrive at the electron ohmic contact than holes at the hole ohmic contact. Since in one dimension the total current must be position independent, the electric field is distorted to forward bias the i/n interface and to cause the subsequent electron back-injection current compensating for the difference between the two photocurrents.

This is shown in the equivalent-circuit model of Fig. 5.5. The current sources I_1 and I_2 are the electron and hole photocollected current (defined in the next section). Diodes D_1 and D_2 represent the p/i and i/n interfaces, respectively, while D_3 accounts for the carrier injection caused by the terminal voltage. The limiting carrier is the carrier with the least photocollected current. For uniform excitation $I_2 \gg I_1$, holes are the limiting carriers and D_1 is reverse biased while D_2 is forward biased under short-circuit conditions. This

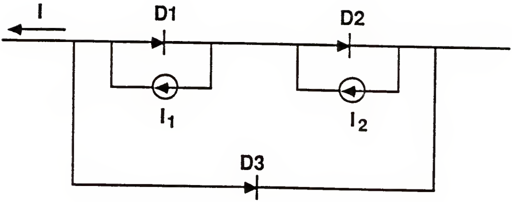

Fig. 5.5 Equivalent-circuit model for an a-Si:H solar cell.

explains the high field density at the p/i interface and the deep minimum near the i/n interface shown in Fig. 5.3(b). The equivalent circuit of Fig. 5.5 also explains why the strongly absorbed light only slightly perturbs the electric field,as shown in Fig. 5.3(a): almost all carriers are generated near the P^+ layer and this compensates for the shorter hole collection length and makes electrons the limiting carriers. Thus I_1 is only slightly larger than I_2 and the bias across D_1 and D_2 is low.

When a terminal voltage is applied, under uniform excitation this voltage drops almost entirely across D_1 since a very small voltage drop across the forward biased D_2 can accommodate any difference in the terminal current. This accounts for the sharp drop of the field with increased bias at the p/i interface and the minor dependence of the minimum value of the field on terminal bias (Fig. 5.4(b)). In the case of strong absorption the applied voltage is nearly evenly divided between D_1 and D_2. Field changes in the i-layer sustain the applied voltage and the field minimum becomes sensitive to the external bias (Fig. 5.4(a)).

The previous analysis about the dependence of the voltage across D_1 and D_2 on excitation can explain the recombination profiles shown in Fig. 5.6(a,b). For uniform excitation the large difference between currents I_1 and I_2 circulates through D_2 and creates the high recombination rate near the i/n interface (Fig. 5.6(b)). At this interface the recombination rate is almost terminal bias independent because the voltage across D_2 is nearly terminal bias independent. For strong absorption the recombination rate at short circuit is higher

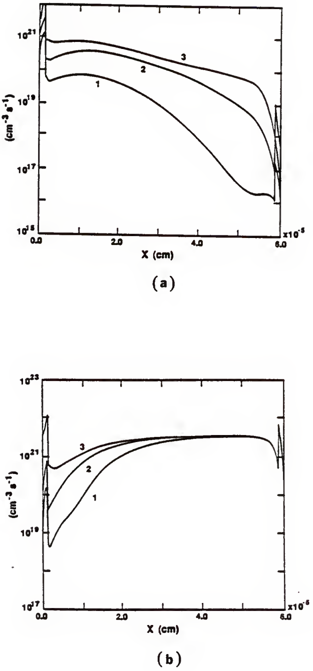

Fig. 5.6 Recombination rate profiles as functions of the forward terminal bias. (a) Strongly absorbed light. (b) Uniformly absorbed light. Curves 1, 2, 3 correspond to short-circuit, maximum-power and open-circuit conditions, respectively.

near the p/i interface than it is in the rest of the device because of the slight forward bias across D_1. For higher terminal voltages the pn product depends more on the terminal bias and less on the generation profile resulting in flatter recombination profiles as shown in Fig. 5.6(a).

Now we shift our attention to AM1.5 light. The recombination rate (Fig. 5.7) is higher near the N^+ layer (especially at low applied voltages) since electrons have higher photocollected current and the recombination current through D_2 is higher than through D_1 (Fig. 5.5). Figure 5.7 also shows the generation rate profile which is shown to be higher than the recombination rate in the front part of the device even at open circuit. The difference between bulk generation and recombination is compensated by the electron surface recombination at the P^+ ohmic contact. This surface recombination, caused primarily by the low hole density in the P^+ layer and the subsequent high electron injection in this layer, is the major loss mechanism for the device under study. Another aspect of Fig. 5.7 is that AM1.5 light results in a recombination profile having the same qualitative features as the recombination profile of the strongly absorbed light.

In Fig. 5.8 the electric field profile is shown at short-circuit maximum-power and open-circuit conditions. We see that it combines features from both the strongly absorbed and the uniformly absorbed light field profiles (Fig. 5.4(a,b)). This indicates that the concept of the limiting carrier is not so well defined under AM1.5 light as it is for strongly and/or uniformly absorbed light. Fig. 5.9 shows the electron and hole current profiles. The sharp increase of the electron

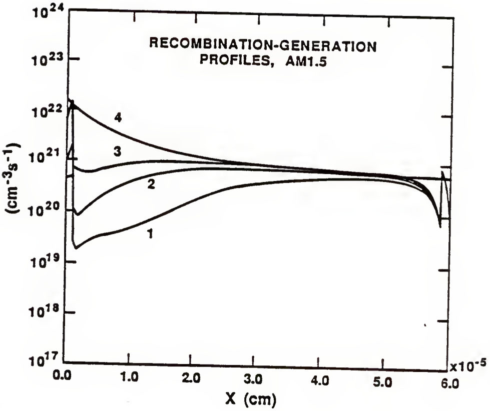

Fig. 5.7 Recombination profiles as functions of the applied forward bias for AM1.5 light. Curves 1, 2, 3 correspond to V = 0 (short-circuit), 0.740 (maximum-power) and 0.922 Volts (open-circuit), respectively. Curve 4 is the generation profile.

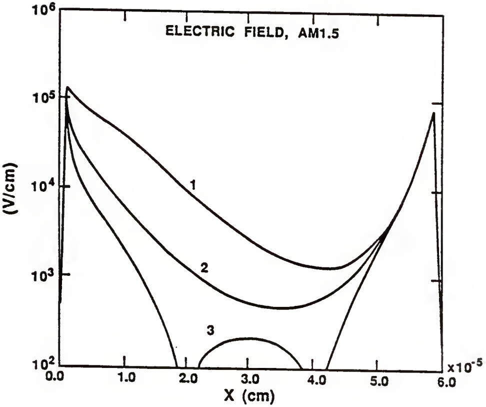

Fig. 5.8 Electric field profiles as functions of the applied forward bias for AM1.5 light. Curves 1, 2, 3 correspond to V = 0 (short-circuit), 0.740 (maximum-power) and 0.922 Volts (open-circuit), respectively.

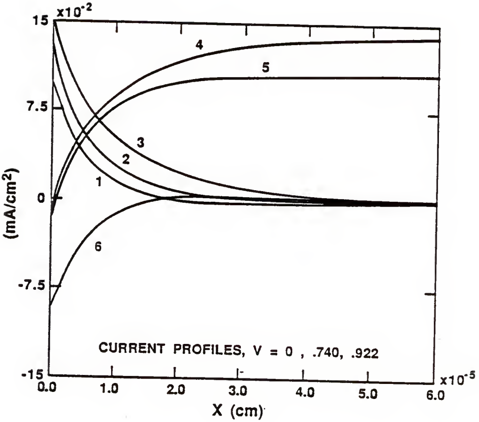

Fig. 5.9 Electron and hole current profiles as functions of the applied forward bias for AM1.5 light. Curves 3, 2, 1 (hole current) and 4, 5, 6 (electron current) correspond to V = 0 (short-circuit), 0.740 (maximum-power) and 0.922 Volts (open-circuit), respectively.

current near the P^+ contact is due to the high generation rate at this contact. For voltages near the open-circuit voltage the electron current drastically decreases with bias and reverses sign at the front part of the cell because of the back-injection into the P^+ layer. Figures 5.10 (a,b) present the carrier density profiles. The carrier density near the p/i interface is more sensitive to forward voltage because the applied voltage mainly drops in the reverse biased D_1 diode of the equivalent-circuit model of Fig. 5.5. From Fig. 5.8, 5.9 and 5.10 one concludes that the order of magnitude of the electron density in the i-layer can be expressed by the drift only approximation as $n = J_n/(q\ \mu_n\ E)$. A similar relation holds for holes. The approximation is better for low forward voltages where the field is still high in the i-layer.

The carrier lifetimes, defined as the ratio of the carrier densities over the recombination rate, are shown in Fig. 5.11 (a,b). Near the N^+ layer the carrier lifetimes are basically bias independent because the applied voltage drops almost entirely on D_1. As a result the hole lifetime decreases with forward voltage near the p/i interface. At the same interface the electron lifetime increases because the electron density increases faster than the recombination rate with forward bias. In the heavily doped layers the carrier lifetime is bias independent because, there, the minority-carrier density and recombination rate are linearly proportional to each other. This linear relation can be derived from (5.2) when $p \gg n$ or $n \gg p$.

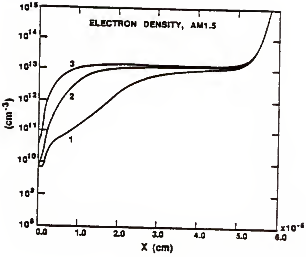

(a)

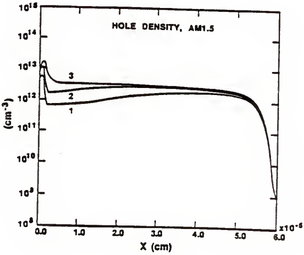

(b)

Fig. 5.10 Free carrier density profiles as functions of the applied forward bias for AM1.5 light. (a) Electron density. (b) Hole density. Curves 1, 2, 3 correspond to V = 0 (short-circuit), 0.740 (maximum-power) and 0.922 Volts (open-circuit), respectively.

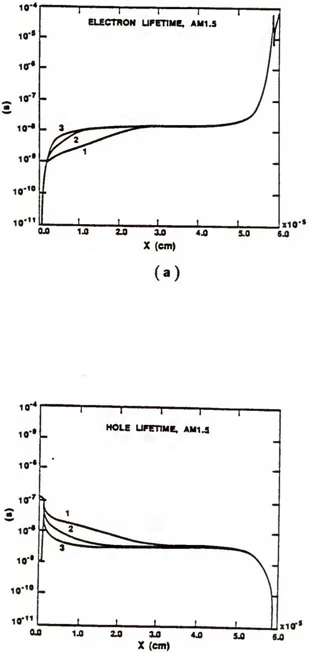

(a)

(b)

Fig. 5.11 Free carrier lifetime profiles as functions of the applied forward bias for AM1.5 light. (a) Electron lifetime. (b) Hole lifetime. Curves 1, 2, 3 correspond to V = 0 (short-circuit), 0.740 (maximum-power) and 0.922 Volts (open-circuit), respectively.

5.4 Analytical Modeling

5.4.1 Definition of Photocollected Currents

To define mathematically what I_1 and I_2 in Fig. 5.5 are, we use our numerical results for the electric field, E(x) and the carrier recombination lifetimes, τ_n and τ_p, to separate the currents into photocollected and back-injection components. For a given generation profile the electron (hole) photocollected current results from the photogenerated electrons (holes) that cross the cell, under the influence of the numerically calculated electric field E(x) and lifetime τ_n (τ_p), and become collected by the electron (hole) contact. On the other hand, the back-injection electron (hole) current is the current that would flow in the dark if the electric field were E(x) and the lifetime τ_n (τ_p). In calculating the photocollected and back-injection currents the recombination velocities at the ohmic contacts retain the values assigned in the introduction, S_n and S_p.

In more analytical terms the electron photocollected current J_n' is the solution of the system of the equations:

$$J_n' = e\,\mu_n\, n'\, E + e\, D_n\, dn'/dx \qquad (5.11(a))$$

$$dJ_n'/dx = -\, e(G - n'/\tau_n). \qquad (5.11(b))$$

The boundary condition for (5.11) at the P^+ ohmic contact is represented by the recombination velocity for electrons S_n, $J_n'(0) = eS_n n'(0)$, while at the N^+ ohmic contact is $n'(W)=0$. On the other hand, the equations

$$J_{bin} = e\,\mu_n\, n''\, E + e\, D_n\, dn''/dx \qquad (5.12(a))$$

$$dJ_{bin}/dx = e\ n''/\tau_n, \tag{5.12(b)}$$

define the electron back injection component, J_{bin}. The boundary conditions for (5.12) at the P^+ ohmic contact are represented by the same recombination velocity for electrons S_n, while at the N^+ ohmic $n''(W) = N(W) = 10^{16}\ cm^{-3}$, where N(W) is the equilibrium electron density at the electron ohmic contact. In (5.11) and (5.12), E and τ_n are the numerically calculated electric field and electron lifetime. Equations similar to (5.11) and (5.12) hold for holes also.

Based on the apparent linearity of the carrier transport equations, we can see that under optical and terminal excitation the electron (hole) current is the sum of the photocollected and back-injection components:

$$J = J_{ph} + J_{bi}. \tag{5.13}$$

We emphasize that this separation of currents does not imply that the superposition principle holds for a-Si:H p/i/n solar cells. The dependence of the electric field and carrier lifetimes on bias invalidates this principle. The separation of currents attempted here only seeks to clarify the concept of the limiting carrier.

According to the model shown in Fig. 5.5 the carrier with the least photocollected current is the limiting carrier and determines the cell photocurrent. The photocurrent is defined as the algebraic difference between the terminal current under illumination and the terminal current in the dark at the same voltage. To support the predictions of this model we present in Fig. 5.12(a,b) numerical results on the cell terminal, photocollected and back-injection

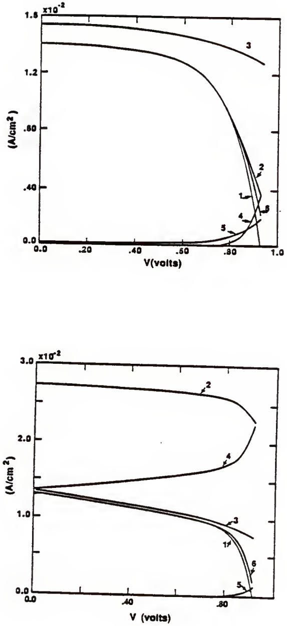

Fig. 5.12 Current-Voltage characteristics. (a) Strongly absorbed light. (b) Uniformly absorbed light. Curves 1, 2, 3, 4, 5, 6 are the terminal current, electron photocollected current, hole photocollected current, electron back-injection current, hole back-injection current and cell photocurrent, respectively.

current densities for strongly and weakly absorbed light. As discussed in the previous section, for strongly absorbed light the carriers (electrons) associated with the nonilluminated contact are the limiting carriers. This is illustrated in Fig. 5.12(a), where the electron photocollected current is shown to be very close to the terminal current and even closer to the terminal photocurrent. The higher hole photocollected current forward biases the p/i interface and creates the hole back-injection current. The electron back-injection current is negligible at low terminal voltage, where the i/n interface is reverse biased, and increases at voltages near V_{oc}, where both interfaces are forward biased. The hole back-injection current and the back diffusion of photogenerated electrons compensate for the difference between the two photocurrents. This difference is small resulting in high internal quantum efficiency (≈ 85%) for the strongly absorbed light. For uniformly absorbed light (Fig. 5.12(b)) the large difference between the electron and the hole photocollected currents reduces drastically the cell photocurrent and the internal quantum efficiency (≈ 45%). At low voltages the small difference (≈.5 mA) between the hole photocollected current and the cell photocurrent is due to the back diffusion of photogenerated electrons in the P+ layer. At voltages near V_{oc} this difference becomes larger due to the disturbance of the electric field in the P^+ layer. The high electron back-injection current implies the strong forward bias of the i/n interface.

Figure 5.13 shows the same currents for AM1.5 light. Holes are here the limiting carriers because their photocollected current is

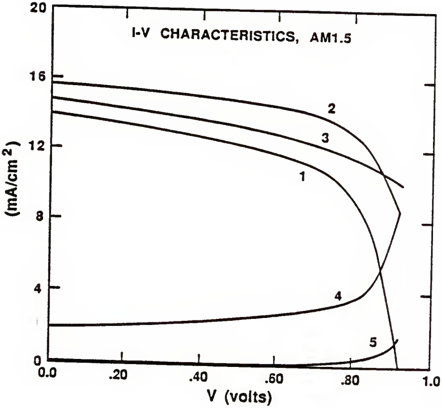

Fig. 5.13 Current-Voltage characteristics for AM1.5 light. Curves 1, 2, 3, 4, 5, 6 are the terminal current, electron photocollected current, hole photocollected current, electron back-injection current, hole back-injection current and cell photocurrent, respectively.

less than the electron photocollected current. The difference between the two currents, however is small since the high generation rate near the P^+ layer compensates for the smaller hole collection length. For the device under study the AM1.5 short-circuit current, open-circuit voltage, fill factor and conversion efficiency were 13.93 mA, 0.922 V, 0.614 and 8.2%, respectively.

5.4.2 Analytical Solutions for Strongly Absorbed Light

Based on the above discussion, we can write the cell photocurrent as

$$J_{ph} = J_L + J_{bd}, \tag{5.14}$$

where J_L is the limiting carrier photocollected current, calculated at the respective ohmic contact, and J_{bd} is a correction term to include the back diffusion of photogenerated minority carriers near the same contact. To be able to derive closed form expressions, the electric field and carrier lifetimes are assumed spatially independent. The limitations of this assumption are discussed later in this and the last section. Under these assumptions and for strongly absorbed light shining through the P^+ layer the expression for the cell photocurrent becomes, as derived in Appendix B,

$$J_{ph} = J_n = e\,F \quad \frac{2\alpha[1/L_E^2 + 1/L^2]^{1/2}}{\alpha^2 + 2\alpha/L_E - 1/L^2} \quad \frac{\exp(W/L_2)}{1 - \exp[W(1/L_2 - 1/L_1)]}, \tag{5.15}$$

where $L_E = 2(kT/e|E|)$, L is the diffusion length, $L = (D\tau)^{1/2}$, F is the photon flux density and L_1 and L_2 are defined as

$$L_1 = [1/L_E + (1/L_E^2 + 1/L^2)^{1/2}]^{-1}, \quad L_2 = [1/L_E - (1/L_E^2 + 1/L^2)^{1/2}]^{-1}. \tag{5.16}$$

In (5.15) the cell photocurrent was set equal to the electron photocollected current since the hole back-diffusion current near the N^+ contact is negligible. If the electron collection length l_c satisfies the relation $l_c \gg 4kT/(e|E|)$, which is normally satisfied for voltages below V_{oc}, then (5.15) can be simplified to

$$J_{ph} = e\ F \frac{e|E|/kT}{\alpha + e|E|/kT} \exp(-W/l_c). \tag{5.17}$$

In the drift only approximation $\exp(-W/l_c)$ is the probability that an electron generated at $x = 0$ is collected by the electron ohmic contact located at $x = W$. Therefore, if there were no diffusion, the photocurrent would be $J_{ph} = e\ F \exp(-W/l_c)$ since almost all carriers are generated near $x = 0$ because of the strong absorption. The term $e\ E\ /(\alpha + e\ E\ /kT)$ accounts for the back diffusion of electrons generated near the hole contact [43]. To make (5.15) and (5.17) better correspond to the actual field distribution, we introduce in these equations the field magnitude at the p/i interface, E_p, and the field magnitude in the i-layer bulk, E_b. Equation (5.15) now becomes

$$J_{ph} = e\ F \frac{2\alpha[1/L_{Ep}^2 + 1/L^2]^{1/2}}{\alpha^2 + 2\alpha/L_{Ep} - 1/L^2} \frac{\exp[W(1/L_2)]}{\exp[W(1/L_2 - 1/L_1)]}, \tag{5.18}$$

where $L_{Ep} = 2kT/(eE_p)$, $L_{Eb} = 2kT/(eE_b)$, and L_1, L_2 are given by (5.16) where now L_{Eb} replaces L_E. Similarly, (5.17) becomes

$$J_{ph} = e\ F \frac{e|E_p|/kT}{\alpha + e|E_p|/kT} \exp(-W/l_c), \tag{5.19}$$

where in (5.19) $l_c = \mu_n E_b \tau$. In this model we assume that only E_p and

E_b change with terminal voltage. The value of the field at the p/i interface is of the order of 10^5 V/cm and exhibits a weak bias dependence (Fig. 4(a)). A suitable expression for the field dependence on the terminal voltage V is

$$E_p = 0.8\text{x}10^5 \ (V_p - V)/V_p, \tag{5.20}$$

where V_p is a parameter to be determined by the numerical fitting. The field in the intrinsic layer is expressed as

$$E_b = (V_o - V)/W, \tag{5.21}$$

where V_o is a characteristic voltage defined by the property that $V = V_o$ makes the average field zero in the intrinsic layer. This characteristic voltage normally assumes values in the vicinity of V_{oc}. The best fitting was obtained for $V_p = 1.2$ V and $V_o = 0.88$ V. Figure 5.14 shows the numerical and analytical photocurrent calculations for strongly absorbed light. We can see that there is good agreement between numerical and analytical results. The parameter to which the fitting is most sensitive is the limiting carrier $\mu\tau$ product. The value of $\mu_n\tau_n$, $1.4\text{x}10^{-7}$ cm^2/V, used in Fig. 5.14 agrees with the numerical results for $\mu_n\tau_n$. Therefore, by fitting experimental I-V characteristics for strongly absorbed light to the analytical expression (5.19), one can extract the limiting carrier $\mu\tau$ product.

5.4.3 Analytical Solutions for Uniformly Absorbed Light

For uniform absorption holes are the limiting carriers. Under the assumptions of uniform field and lifetimes the hole photocollected

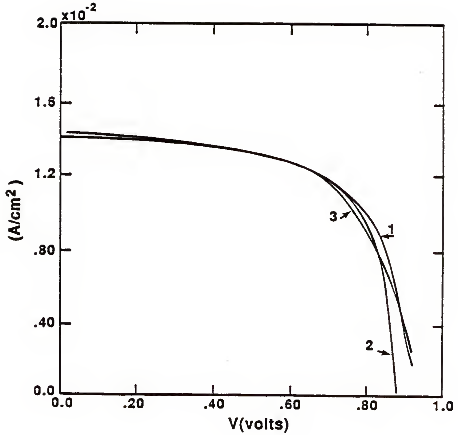

Fig. 5.14 Numerical and analytical photocurrents versus forward bias, for strongly absorbed light. Curves (1) and (2) are derived from (5.18) and (5.19), respectively, and curve 3 is the numerically calculated photocurrent.

current density can be expressed, as shown in Appendix B, as

$$J_p = eG \frac{L^2[(1/L_2 - 1/L_1)\exp(W/L_2) + 1/L_1 - \exp(W/L_2 - W/L_1)/L_2]}{1 - \exp(W/L_2 - W/L_1)}, \quad (5.22)$$

where L_1 and L_2 are given by (5.16), G is the generation rate per unit volume, and L is now the hole diffusion length. If l_{cu} is the limiting carrier (holes) collection length, $l_{cu} = |E|\mu_p\tau_p$, and if $l_{cu} \gg 4kT/e|E|$, a condition satisfied for voltages below V_{oc}, then (5.22) can be written as

$$J_p = qG[l_{cu}(1 - \exp(-W/l_{cu})) - (kT/q|E|)(-1 + 2\exp(-W/l_{cu}))]. \quad (5.23)$$

The first term in the square bracket in (5.23), $l_{cu}(1 - \exp(-W/l_{cu}))$, dominates and is the same as the expression for the internal quantum efficiency in the Hecht formula, also derived by Crandall [44]. We emphasize that in (5.23) l_{cu} is the collection length of the carrier with the least photocollected current and not the sum of the electron and hole collection as concluded in [44]. Since the Hecht formula is based on the drift approximation, we can consider the second term in (5.23) as a correction to include diffusion. If l_c is the electron collection length, then, based on (5.23), the electron back-diffusion current near the P^+ contact can be written as

$$J_{bd} = -qG(kT/q|E|)(-1 + 2\exp(-W/l_c)). \quad (5.24)$$

From (5.14) the cell photocurrent density becomes

$$J_{ph} = eG[l_{cu}(1 - \exp(-W/l_{cu}) - (kT/e|E|) \times$$

$$(-2+2\exp(-W/l_{cu})+2\exp(-W/l_c))]. \qquad (5.25)$$

The dominant term in (5.25) is $l_{cu}(1 - \exp(-W/l_{cu}))$ because of the high value of $|E|$. The two other terms represent diffusion losses. As we have seen in the numerical results section, under uniformly absorbed light a total generation rate of 1.88×10^{17} cm^{-2} s^{-1} strongly perturbs the electric field the minimum of which near the i/n interface is slightly affected by a small forward bias. Such a bias mainly drops at the p/i interface. Therefore, to account for the field nonuniformities in distance and bias, we introduce in (5.25) a quadratic dependence of the field strength on the bias:

$$|E| = [V_{bi} - V(V/V_N)]/W, \qquad (5.26)$$

where V_{bi} is the built-in barrier height and V_N a normalization parameter accounting for the field nonuniformities. The best fit between analytical and numerical results were obtained for $V_N = V_{bi} =$ 1.16 V. Figure 5.15 shows numerical and analytical calculations for the photocurrent density as a function of the voltage. Curve 1 corresponds to (5.25) while curve 2 is the plot of the Hecht formula $J_{ph} = qGl_{cu}[1 - \exp(W/l_{cu})]$. These analytical formulas are in good agreement with the numerical photocurrent (curve 4) for voltages up to V_{oc}. The value of the hole $\mu\tau$ product used to generate curves 1 and 2 is 1.5×10^{-9} cm^2/V, a value close to the numerical results. At voltages near V_{oc} the strong perturbation of the field in the P^+ layer causes a strong electron current towards the P^+ contact. This is not predicted

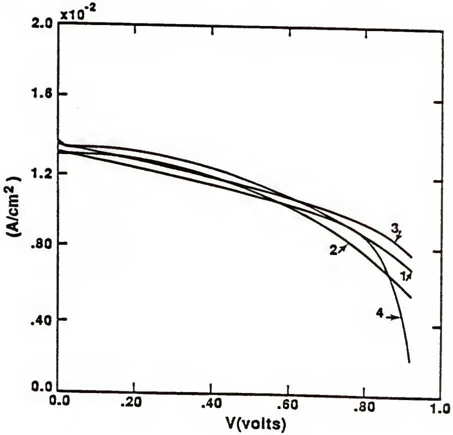

Fig. 5.15 Numerical and analytical photocurrents versus forward bias, for uniformly absorbed light. Curves (1) and (2) are derived from (5.22) and the Hecht formula, respectively, curve 3 is the hole photocollected current and curve 4 is the numerically calculated photocurrent.

by (5.25). We think this is the reason for the disagreement between numerical and analytical results near V_{oc}. This view is supported by the good agreement among curves 1,2 and curve 3 which is the numerically calculated hole photocollected current density. Note that if the total generation rate were much smaller ($\approx 10^{14}$ $cm^{-2}s^{-1}$) the field would be more uniform and we could model the field dependence on the bias by simply setting $|E| = (V_{bi} - V)/W$. In Appendix B an analytical formula is presented for the photocurrent under AM1.5 illumination.

5.5 Discussion and Critical Review of the Literature

A basic concept used in the modeling of a-Si:H is the concept of the limiting carrier [42], [44], [45], [46]. Determination of the limiting carrier provides insight about mechanisms that constrain the quantum efficiency and open-circuit voltage as well as about the asymmetric performance of the cell when illuminated from different sides. Crandall [44] and Okamoto [45] conclude that the cell performance is determined by the sum of the hole and the electron collection lengths, respectively. Hence, they conclude, the carrier with the longest collection length is the limiting carrier. Similar results have been reached by Sichanugrist [46]. In the above models electric field and carrier lifetimes were assumed spatially independent. To understand why the above conclusions are incorrect we have to reconsider the legitimacy of the constant field approximation.

To do so we introduce a phenomenological way of thinking and follow the sequence of events that take place after a sudden application of an optical excitation to a short-circuited cell. We assume a uniform optical generation and that electrons have higher mobility and lifetime than holes. Immediately after the excitation photogenerated electrons and holes will move towards their respective contacts. Because electrons have higher mobility and lifetime than holes, the electron photogenerated current collected at the N^+ layer is higher than the hole photogenerated current collected at the P^+ layer. Since in one dimension the total current is spatially uniform and since the P^+ layer cannot inject electrons in the i-layer, there must be a mechanism that compensates for the difference in the two photogenerated currents. This mechanism is the distortion of the electric field which forward biases the i/n interface and reverse biases the p/i interface. The forward biasing of the i/n interface causes an electron back-injection current that compensates for the difference between the two photocurrents and reduces the total electron current at the N^+ layer to the same level as the hole current at the P^+ contact. The reverse biasing of the p/i causes a negligible hole back injection current.

The conclusion is that the assumption of the constant electric field can be applied only to the carrier with the least photocollected current. If we apply the constant field approximation to the other carrier, we ignore its back-injection current which could be comparable to the photocollected current. Field nonuniformities do affect the current of the carrier with the least photocollected current but their effect is much more severe on the carrier with the higher photocollected current.

We stress here the difference between a bipolar device, like a p/i/n solar cell, and a device like an n/i/n photoconductor. In an a-Si:H p/i/n solar cell the hole current at the P^+ contact must be about the same as the electron current at the N^+ contact. This forces the carrier with the smaller collection length to determine the performance of the device under illumination. On the contrary, the carrier collection of a n/i/n photoconductor, where both ohmic contacts inject the same type of carrier, is based on different principles. To facilitate the discussion, we can imagine an n/i/n photoconductor under terminal bias and uniform optical excitation. Again we assume that the hole collection length is less than the electron collection length. Here, as opposed to the p/i/n case, for every photogenerated hole trapping event in excess of photogenerated electron trapping, an electron will be injected from the negative contact to compensate the charge of the trapped hole. Hence, the current is proportional to the total distance, per unit time, covered by all photogenerated carriers before they recombine. Thus, in a n/i/n photoconductor, the carrier with the longer collection length indeed determines the current. On the contrary, in the p/i/n structure the P^+ contact cannot inject electrons and the continuity of the total current is preserved through forward biasing the i/n interface and subsequent electron back injection.

The conclusion derived here, that the limiting carrier in the p/i/n structure is the carrier with the smaller collection length, has also been reached by other workers [47], [48], [49]. They based their conclusion on the minority-carrier concept borrowed from single-crystal transport theory. However, this concept is not particularly applicable to a-Si:H p/i/n cells since low injection prevails only in the heavily doped layers.

Hack and Shur [42] arrived also at a similar conclusion regarding the limiting carrier. They show, by using numerical solutions, that the short-circuit current decreases when the limiting carrier mobility decreases. In general, their numerical solutions are among the most complete in the literature. They have taken into account the continuous spectrum of trapped states and have presented numerous data on the dependence of internal device parameters on absorption coefficient and band mobilities. Their numerical results agree with ours. The new element in our work is the physical interpretation of the numerical solutions, based mainly on the equivalent circuit model of Fig. 5.5, and the subsequent analytical formulation presented in Section 5.4.

Numerical solutions have also been presented by Swartz [50], Manfredotti [51], Schwartz [52], where the amphoteric nature of the dangling bonds was taken into consideration, and Chen [53]. Their solutions added valuable insight into device understanding. At the same time, each of these solutions is based on different assumptions and device structures. Thus no unifying view of these numerical results is possible, which prevents informed general conclusions for the device operation. It is, therefore, important that consistent numerical solutions are developed that will enable computer experiments designed to reveal the approximations and insight needed for the development of analytical models and other related tools such as equivalent-circuit models. All this, interwoven with experimental assessment, will lead to informed design.

5.6 Conclusions

There are two major results in this Chapter: the equivalent-circuit model of Fig. 5.5, which clarifies the concept of the limiting carrier, and the derivation of analytical expressions, 5.19 and 5.25, for the cell photocurrent density. A central point in our analysis was the separation of currents into photocollected and back-injection components. The carrier with the least photocollected current is the limiting carrier and determines the performance of the device. For strongly absorbed light the limiting carrier is the carrier associated with the non-illuminated contact. Equation (5.19) expresses the photocurrent density in terms of the interfacial field and the limiting carrier collection length. For uniformly absorbed light the limiting carrier is the carrier with the shortest collection length. The Hecht formula can be used in the case of uniformly absorbed light, if a proper assessment of the field dependence on terminal voltage is made. The equivalent circuit of Fig. 5.5 can have practical ramifications. When designing the cell care should be taken that I_1 and I_2 are not only large but, also, about equal. Therefore, the tailoring of the thin film composition, either in terms of alloying to change the band gap or in terms of doping to change the field profile, should focus on increasing the limiting carrier collection probability.

CHAPTER SIX
CRYSTALLINE VERSUS AMORPHOUS SILICON: PHYSICS AND MODELING

6.1 Introduction

Although the fundamental chemical structure (tetrahedrally bonded silicon) is the same in both the crystalline and amorphous silicon, the electronic and optical properties of the two materials are entirely different. The major differences include intrinsic and extrinsic dark conductivity and photoconductivity, optical absorption coefficients, photoluminescence spectrum, Hall effect and thermopower. All of these different properties originate in the nature of the electronic states in the two materials and can be traced back to the methods used to fabricate them.

In single crystal silicon, either crystallized from molten silicon or obtained through epitaxial methods, most of the native atoms are relaxed in their minimum energy position. The high temperature during fabrication, above 1200 °C, gives the silicon atoms the ability to minimize the free energy of the lattice. Well defined point and line defects or metal impurities give rise to discrete energy levels in the band gap. On the other hand, amorphous silicon is deposited in thin films, either by decomposition of silane gases or by sputtering, at relatively low temperatures, 200 - 500 °C. The silicon atoms are "frozen" in metastable equilibrium sites and, although the short range order of tetrahedral bonding is still observed, the bonds between nearest neighbors are stretched. The new lattice has no long range order, and a continuous spectrum of defect states is introduced in the mobility gap. The disruption of lattice periodicity relaxes the crystal momentum conservation rules for optical transitions. This increases the a-Si:H absorption coefficient by about an order of magnitude above the absorption coefficient of crystalline silicon, which is known to be an indirect-gap material, and enables the use of a-Si:H for thin film solar cells. The lack of long range order makes questionable for amorphous silicon both the applicability of Bloch's theorem and the nearly free electron approximation, which is the basis of the charge transport theory in crystalline semiconductors.

This Chapter does not provide answers to the theoretical questions raised above concerning amorphous silicon. We will assume, as we implicitly did in Chapter 5, that the free electron approximation is still a valid hypothesis and that the charge is transferred through drift and diffusion of extended carriers. Section 6.2 focuses on the charge transport mechanisms in the two materials and explains the differences in terms of device dimensions and influence of localized states. Section 6.3 compares the modeling of devices and discusses the applicability to amorphous silicon of concepts such as low injection and minority carrier borrowed from silicon device modeling.

6.2 Charge Transport in Crystalline and Amorphous Silicon Devices

An excellent example that illustrates the difference in the charge transport mechanisms in the two devices is the celebrated time of flight experiment. In crystalline silicon this experiment is usually referred to as Haynes-Shockley experiment. Haynes and Shockley [54] through this experiment proved the existence of excess carriers in semiconductors and measured the minority-carrier mobility and lifetime. In this experiment a light pulse excites a silicon bar (the original experiment was done on germanium) from one end . A blocking contact exists near the other end while two other contacts and an external bias create an electric field, E, across the device. The injected pocket of minority carriers drifts under the influence of the field and at the same time spreads, because of diffusion, and forms a Gaussian function in space. The voltage at the blocking contact will rise when the package of the minority carriers arrives at this contact. Closed form expressions for the time delay between input and output are used to extract the minority-carrier diffusion coefficient and lifetime. That the carrier Debye length is much less than the length of the bar and that the carrier dielectric relaxation time is much less than the transit time is critical to this behavior, and is related to the quasi neutrality condition.

In amorphous silicon the time of flight experiment is done on thin film p-i-n devices similar to the one analyzed in Chapter 5. The device is reverse biased, to increase the field in the i-region and make it more uniform, and a pulse of strongly absorbed light excites the cell, usually through the P^+ layer. The output that is monitored is the transient current through the cell. When the light pulse strikes, a pocket of electrons and holes is generated at the p/i interface. The holes are immediately swept in the P^+ layer, while the electrons drift toward the N^+ layer. One important point that distinguishes this experiment from the previous Haynes-Shockley experiment is that there is no delay between input and output: the output current raises to its maximum right after the excitation, stays practically flat or decays slowly until the electrons arrive at the N^+ layer and then drops to zero with a short time constant. This results from the fact that in the i-layer the transit time is less than the dielectric relaxation time, and the displacement current is communicated at the speed of light because of the absence of carrier screening. The large band gap and the numerous free carrier traps result in low carrier densities and relatively long dielectric relaxation times. The excess photogenerated electrons cross the i-layer before the holes can neutralize their charge. During the transient the current in most of the i-layer is displacement current caused by the space charge of the moving electrons.

In crystalline silicon the minority carriers are transferred through a quasi-neutral region the transit time of which is much longer than the dielectric relaxation time due to the numerous majority carriers. The majority carriers shield the minority-carrier charge and the two pockets move together until they arrive at the junction of the blokcing contact where the strong field separates the carries and causes a current to flow in the external circuit. In a thin-film amorphous silicon cell the whole i-layer is a space-charge region, a strong electric field ($\geq 10^4$ V/cm) extends throughout the device and the separation of photogenerated carriers begins immediately following excitation.

Returning to the time of flight experiment, we identify the time interval between excitation and the fast output current decay with the transit time, t_T, of the device [55]. If E is the average field and W the device thickness, then one could write the relation

$$\mu_e = \frac{W}{E\ t_T} \tag{6.1}$$

for the electron mobility. However, this not the free-carrier mobility but, rather,it is an effective drift mobility. To extract the free carrier mobility we would have to take into account the temporary trapping of the carriers especially in the tail states. This trapping delays the carriers, makes μ_e in (6.1) less than the actual extended mobility and can lead to dispersive transport [55]. The derivation of the mobility and the lifetime from the time of flight experiment depends on the particular model for the interaction between free electrons and localized states or phonons [56,57,58]. Elaboration on these models is beyond the scope of this Chapter. We would only like to stress that in crystalline silicon the transport properties of the free carriers can be extracted directly from transient experiments, as was done in Chapter four. This can be contrasted with the model-dependent interpretation of transient experiments in a-Si:H devices.

6.3 Modeling Aspects of Crystalline and Amorphous Silicon Solar Cells

From a mathematical viewpoint analytical modeling of a bipolar device is equivalent to decoupling the original six Shockley equations into a system of linear differential equations which are independent and related only through boundary conditions. This linearization of the system allows derivation of analytical formulas that enable interpretation of experimental results, allow understanding of the charge-transport mechanisms and enable derivation of equivalent-circuit models.

In single crystal silicon almost all the modeling is based on Shockley's concept of considering a device as consisting of quasi-neutral and space-charge regions. Under low injection the field and the minority- carrier lifetime are bias independent in the quasi-neutral regions and the minority-carrier density can be described by a linear second-order differential equation (3.15). A similar equation can be derived in high injection by using the ambipolar transport equation. This makes possible the calculation of recombination currents and carrier densities in the quasi-neutral regions. The recombination in the space-charge region is treated by making the usual assumptions of the depletion layer approximation, for reverse bias, or the quasi equilibrium approximation for forward voltages. For low or high injection in the quasi-neutral regions, the linear nature of carrier transport in silicon solar cells allows use of the superposition principle to separate the current into independent dark recombination and photogenerated components.

The situation is quite different in a-Si:H p-i-n solar cells. Here the carrier lifetimes and electric field are bias (terminal or optical) dependent. We can still derive (3.15) but now the coefficients will depend on the carrier densities, which renders the system nonlinear despite the apparent linearity of (3.15). It is clear, therefore, that the superposition principle is not valid in a-Si:H solar cells and this is pictorially illustrated in the equivalent-circuit model for amorphous silicon solar cells shown in Fig. 5.5. Although a separation of currents into photocollected and back-injection components is still possible, as was pointed out in Chapter 5, the two currents are not independent: the back- injection component depends on the generation profile and also the cell photocurrent depends on the applied bias.

The nonlinear nature of the system of equations that describe carrier transport in a-Si:H solar cells makes necessary introduction of simplifying approximations, like the constant field and lifetime approximation. Under these approximations we can derive closed form expressions for the cell photocurrent. Such expressions were presented in Chapter 5, where it was emphasized that these assumptions should be applied only to the limiting carrier to avoid neglecting the back-injection current of the non-limiting carrier.

In a device like an a-Si:H p/i/n solar cell the only regions that can be thought as being in low injection are the heavily doped P^+ and N^+ layers. From (5.2) and (5.3) follows that an n(p)-type region is in low injection if $n(p) \gg Cp(n)$. This inequality guarantees that the electric field and the minority carrier lifetime are bias independent. The numerical solutions of Chapter 5 suggest that this is the case for N^+ layer under reasonable bias. This is a result of the high ($\approx 10^{16}/cm^3$) equilibrium electron density in the N^+ layer. Therefore, the recombination losses in the N^+ layer can be modeled as $I_n(\exp(F_{np}/kT)-1)$, where F_{np} is the separation of the two Fermi levels at the i/n interface and I_n the saturation recombination current of the N^+ layer. In the P^+ layer, because of the low ($\approx 5x10^{12}$) equilibrium hole density, the strong generation rate under AM1.5 light and the relatively high electron lifetime, the space charge can change with bias. Therefore, despite the fact that in this layer the holes outnumber the electrons and the electron lifetime is nearly bias independent, the electric field can change with illumination or electrical bias. Thus, the P^+ layer is not really in low injection unless the light is reduced and the electrical bias is kept low.

6.4 Conclusions

The transient and the steady-state experimental and theoretical analysis of crystalline and amorphous silicon photovoltaic devices reveals different charge-transport mechanisms. The interaction between free carriers and traps or tail states determines the experimental behavior of amorphous silicon devices especially during transients. In crystalline silicon devices the carriers are transferred mainly through quasi-neutral regions and the separation of charges takes place at the p/n junction space-charge region. In amorphous silicon thin film devices the transit time is shorter than or is comparable to the dielectric relaxation time and the concept of quasi-neutrality is not applicable.

CHAPTER SEVEN
SUMMARY

Analytical models, computer solutions and optimal design for solar cells were the major contributions of this research. Analytical models and optimum design principles were developed for crystalline silicon solar cells. Computer solutions were obtained for amorphous silicon solar cells to understand the physics of the device and to enable analytical modeling.

In silicon solar cells the effects of certain three-dimensional geometries were assessed. Texturizing the emitter to increase the base absorbance results in the same base recombination as in the one-dimensional device with planar emitter. Also, partitioning the emitter in a base-limited solar cell leaves the open-circuit voltage unchanged. The analysis about three-dimensional effects was extended to bipolar diodes and transistors. It was shown that for certain planar devices the transit time and transport factor can be expressed in terms of the same parameters of corresponding one-dimensional devices. These results have implications in device characterization since they allow measuring the recombination velocity of the front surface of a planar device.

Optimum design principles for silicon solar cells were derived by focusing on the minimization of recombination losses. Lower bounds for the recombination current were obtained in terms of minority-carrier bulk transport and surface parameters. An optimized emitter structure was proposed that minimizes recombination under the metal contact and maximizes current collection in the uncovered areas.

Concluding the modeling of silicon solar cells, a new method was presented and demonstrated that allows determination of the minority-carrier lifetime and diffusivity in the base of the device. The method exploits the Fourier transforms of transient responces caused by pulsed optical excitation to derive the frequency responce of the base.

Thin film solar cells made of amorphous silicon were also modeled. Contact-to-contact computer solutions of the a-Si:H p/i/n solar cell were presented and treated as computer experiments designed to reveal the approximations and insight needed for the development of analytical models. The numerical results allowed study of many aspects of internal variables such as electric field, carrier densities, current densities and recombination rates versus position, terminal voltage, and photon flux density. Strongly absorbed, weakly absorbed and AM1.5 light were studied to gain insight needed for the analytical modeling. The resulting analytical and equivalent-circuit models support each other and explain the physical origin of interdependencies among such variables as quantum efficiency, electric field and recombination rate profiles and their relation to current-voltage characteristics. The concept of the limiting carrier was mathematically treated by separating the current into photocollected and back-injection components. This leads to analytical expressions for the cell photocurrent in terms of the limiting-carrier collection length. The limiting carrier is the carrier with the least photocollected current.

Finally, the physics and the modeling of crystalline and amorphous silicon photovoltaic devices were compared. The differences in the transport properties of the two materials are interpreted in view of the Haynes-Shockley and time of flight experiments. In silicon solar cells the transit time is much longer than the dielectric relaxation time, the device is mostly quasi neutral and a photogenerated carrier has to arrive at the junction to contribute to the terminal current. In amorphous silicon solar cells the transit time is comparable to the dielectric relaxation time, the space charge region extends throughout the device and a photogenerated carrier can contribute to the external current by causing displacement current.

APPENDIX A
PROOF OF (3.18) AND (3.19)

From (3.8) and $R_s = 0$ we have

$$\frac{dR_{op}}{dx} = \frac{1}{N_{eff}\tau}\left(1 - \frac{R_{op}^2}{R_b^2}\right) > \left(\frac{1}{N_{eff}\tau}\right)_m \left(1 - \frac{R_{op}^2}{R_{bm}^2}\right), \qquad (A.1)$$

since if $R_s < R_{bm}$ then $R_{op} < R_{bm} < R_b$. The solution of the following differential equation

$$\frac{dy}{dx} = \frac{1}{(N_{eff}\tau)_m}\left(1 - \frac{y^2}{R_{bm}^2}\right) \qquad (A.2)$$

subject to the boundary condition of $y(0)=0$, is

$$y = R_{bm} \tanh\left(\frac{x}{l_m}\right), \qquad (A.3)$$

where $l_m = R_{bm}/(1/N_{eff}\tau)_m$. From (A.1) and (A.2)

$$R_{op}(x, R_s=0) > y = R_{bm} \tanh\left(\frac{x}{l_m}\right). \qquad (A.4)$$

Both functions $R_b(N_1) \tanh(x/L(N_1))$ and $R_{bm} \tanh(x/L(N_2))$ are greater than $R_{op}(x,R_s=0)$ since they are the functions for the normalized recombination current of a uniform region having $R_s = 0$, $N = N_1 = N[(1/N_{eff}\tau)_m]$ and $N = N_2 = N(R_{bm})$, respectively. By definition, $R_{op}(x,R_s=0)$ is less than either one of these two functions. This proves (3.18). In a similar way one could prove (3.19) by using the relation

$$\frac{dR_{op}(x,R_s=\infty)}{dx} = \frac{1}{N_{eff}\tau} - \frac{N_{eff}}{D} R_{op}^2(x,R_s=\infty) >$$

$$\left(\frac{N_{eff}}{D}\right)_M (R_{bm}^2 - R_{op}^2(x,R_s=\infty)). \tag{A.5}$$

APPENDIX B
DERIVATION OF PHOTOCURRENT RELATIONS

Here we apply the reciprocity theorem of section 2.2 to derive the expression for the photocurrent of an one-dimensional uniform region. Let L be the minority-carrier (electrons) diffusion length and S the back surface ($x = W$) recombination velocity S. The expression for the minority-carrier density is

$$n(x) = A \exp(-x/L) + B \exp(x/L). \tag{B.1}$$

The boundary condition at $x = W$ is,

$$J_n(W) = e\ D\ dn/dx = -\ e\ S\ n(W). \tag{B.2}$$

Coefficients A and B are determined from (B.2) and from the normalization condition which requires $n(0) = 1$. Thus,

$$A = \frac{1}{2} \frac{\exp(W/L) + (LS/D)\exp(W/L)}{\cosh(W/L) + (LS/D)\sinh(W/L)},$$

$$B = \frac{1}{2} \frac{\exp(-W/L) - (LS/D)\exp(-W/L)}{\cosh(W/L) + (LS/D)\exp(W/L)}. \tag{B.3}$$

Using (2.9), the collection probability at point x is

$$P_c(x) = n(x) = \frac{\cosh((W-x)/L) + (LS/D)\sinh((W-x)/L)}{\cosh(W/L) + (LS/D)\ \sinh(W/L)}. \tag{B.4}$$

Equation (B.4) can be extended to the sinusoidal steady state by replacing L with $L'(\omega) = L/(1 + j\omega\tau)^{1/2}$, where τ is the lifetime. For a uniform generation rate G, the photocurrent in the frequency domain becomes

$$J_{sc}\ (\omega) = e\ G \int_0^W P_c(x,\omega)\ dx = e\ G \int_0^W n(x,\omega)\ dx =$$

$$e\ G\ L' \ \frac{\sinh(W/L') + (SL'/D)\cosh(W/L') - SL'/D}{\cosh(W/L') + (SL'/D)\sinh(W/L')}. \qquad \text{(B.5)}$$

The last relation proves (4.1). Equation (4.2) can also be derived by setting $F'(\omega)$ equal to $P_c(W,\omega) = n(W,\omega)$.

Focusing now on a-Si:H p/i/n devices let us assume that the carriers not only diffuse but also drift under the influence a spatially uniform electric field E. Then, from the continuity equation and the expression of the current in terms of drift and diffusion, we have for the limiting carrier

$$D\ \frac{d^2n}{dx^2} + \mu\ E\ \frac{dn}{dx} - \frac{n}{\tau} = 0. \qquad \text{(B.6)}$$

The general solution of this equation can be written as

$$n(x) = A'\ \exp(x/L_1) + B'\ \exp(x/L_2), \qquad \text{(B.7)}$$

where

$$L_1 = [1/L_E + (1/L_E{}^2 + 1/L^2)^{1/2}]^{-1}\ ,\ L_2 = [1/L_E - (1/L_E{}^2 + 1/L^2)^{1/2}]^{-1}.$$

Here L_E=-2kT/qE and E>0. For infinite recombination velocity at x = W, n(W) = 0 and for n(0) = 1 (normalization condition), A' and B' become

$$A' = \frac{-\exp(W/L_2 - W/L_1)}{-\exp(W/L_2 - W/L_1) + 1}, \qquad B' = \frac{1}{-\exp(W/L_2 - W/L_1) + 1}. \tag{B.8}$$

If strongly absorbed light, $\exp(-\alpha W) \ll 1$, shines from the back surface, then the photocurrent becomes

$$J_{ph} = e\,F\,\alpha \int_0^W \exp\alpha(x - W)\; P_c(x)\; dx =$$

$$eF\alpha \int_0^W \{[A'\exp(x/L_1) + B'\exp(x/L_2)]/\exp(-qEx/kT)\}\exp[\alpha(x-W)]dx, \tag{B.9}$$

where $\exp(-qEx/kT)$ is proportional to the equilibrium electron density of a region having spatially uniform electric field E. From (B.9), (B.8) and $\exp(-\alpha W) \ll 1$ (5.15) can be derived. Equation (5.22) can be derived from (B.8) and the following expression for the photocurrent for uniformly absorbed light:

$$J_{ph} = e\,G \int_0^W P_c(x)\; dx =$$

$$e\,G \int_0^W \{[A'\exp(x/L_1) + B'\exp(x/L_2)]/\exp(-qEx/kT)\}\; dx. \tag{B.10}$$

For an arbitrary generation profile, G(x), like the one created by AM1.5 light, the photocurrent is given by

$$J_{ph} = e \int_0^W G(x)\{[A'\exp(x/L_1) + B'\exp(x/L_2)]/\exp(-qEx/kT)\}\; dx. \tag{B.11}$$

APPENDIX C
MINORITY-CARRIER ACCUMULATION AT THE BASE EDGE OF A JUNCTION SPACE-CHARGE REGION UNDER SHORT-CIRCUIT CONDITIONS

The purpose of this appendix is to set forth accurate boundary conditions for a short-circuited p/n junction solar cell under illumination. These boundary conditions pertain to the base edge of the junction space-charge region (SCR). The usual assumption is that the excess electron and hole densities vanish at $x = W$. This corresponds to an assumed infinite effective surface recombination velocity S. Chapters 1 through 4 implicitly used this assumption. Another approximation consists in setting S equal to the kinetic limit or unilateral thermal velocity $S_{KL} = U_{th}/(6\pi)^{1/2}$, where U_{th} is the root mean square thermal velocity of the electrons considered as a Boltzmann gas [59].

Here we derive and demonstrate more accurate boundary conditions. For low injection, we define S as the ratio of the minority-carrier diffusivity to the extrinsic Debye length. For moderate or high injection we derive a nonlinear expression for the excess hole and electron densities. The same expression for S holds also as the boundary condition at the collector edge of a quasi-neutral base (QNB) of a transistor in the forward-active mode. The new value of S is a factor of six smaller than S_{KL} for lightly doped ($\approx 10^{14}$ cm^{-3}) silicon, which has practical consequences particularly for transient experiments used in determining carrier lifetimes and diffusion coefficients. For higher doping densities the derived expression for S converges to S_{KL} and the effect of the accumulation of minority carriers at the SCR edge of the base is found negligible. The results, therefore, reached in the first four Chapters are still valid since they were derived for regions in low injection, which implies at least a moderate doping density ($\geq 10^{15}$ cm^{-3}). Thus, the expressions derived here become important only for lightly doped regions in high injection.

Figure C.1 shows an illuminated n/p junction solar cell under short-circuit conditions. The equation for the electron current is

$$J_n(x) = e\, D_n(x) dn(x)/dx + e\, \mu_n(x) E(x) n(x), \qquad (C.1)$$

a first-order linear differential equation for n(x). By integrating this equation [60] we can express the electron density in the SCR in terms of the electric field and electron current as follows:

$$n(x) = \exp[-\textstyle\int_0^x (e/kT)E(x')dx']\{n(0) + \int_0^x (J_n(x')/eD_n(x'))\exp[\int_0^{x'} (e/kT)E(x'')dx'']dx'\}, \qquad (C.2(a))$$

where the Einstein relation was used.

As shown in Fig. C.1, the point x = 0 is the emitter edge of the SCR and n(0) is the majority carrier density at x = 0. Taking V(x) to be the electrostatic potential in the electron energy scale referenced to V at x = 0, we can write (C.2(a)) as

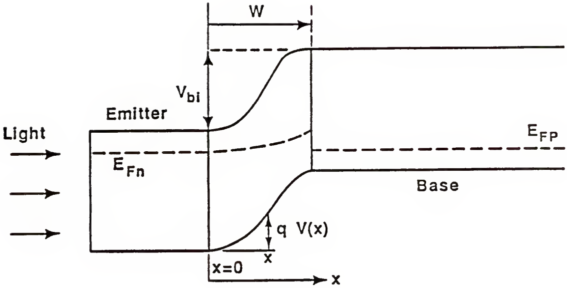

Fig. C.1 An illuminated solar cell under short-circuit conditions. The electron accumulation at x = W is emphasized through the separation of the quasi-Fermi levels, $E_{Fn} - E_{Fp}$.

$$n(x) = \exp(-eV(x)/kT)[n(0) + \int_0^x (J_n(x')/eD_n(x'))\exp(eV(x')/kT)dx']. \qquad (C.2(b))$$

If W is the SCR thickness and V_b is the SCR barrier height, then from (C.2(b)) the electron density at the edge of the base becomes

$$n(W) = \exp(-eV_b/kT)n(0) + \exp(-eV_b/kT) \int_0^W (J_n(x)/eD_n(x))\exp(eV(x)/kT)dx. \qquad (C.3)$$

We now examine separately the low injection and the moderate or high injection cases in the base. The emitter is heavily doped and is in low injection for any level of excitation. First we deal with low injection.

If low injection prevails in the base and if we neglect series resistance, then in (C.3) V_b becomes V_{bi}, where V_{bi} is the SCR built-in voltage in equilibrium. Since $n_o(W) = \exp(-eV_{bi}/kT)n(0)$ is the equilibrium minority-carrier density at the base edge of the SCR, the excess minority-carrier density at this edge becomes

$$\delta n(W) = \exp(-eV_{bi}/kT) \int_0^W (J_n(x)/eD_n(x))\exp(eV(x)/kT)dx. \qquad (C.4)$$

Since the term $\exp(eV(x)/kT)$ increases dramatically with x for $0 < x < W$ while $J_n(X)$ and $D_n(x)$ are much weaker functions of x, the integrand in (C.4) has the qualitative shape pictured in Fig. C.2. Here, δx is a small distance in the vicinity of $x = W$ where $\exp(eV(x)/kT)$ stays relatively constant. Therefore, (C.4) becomes

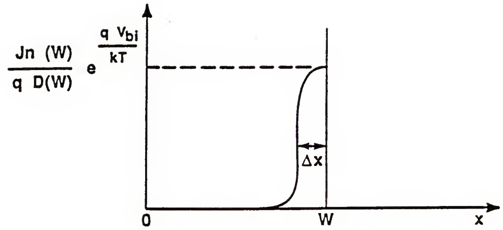

Fig. C.2 The quantity $(J_n/eD)\exp(eV/kT)$ as a function of the distance in the space charge region.

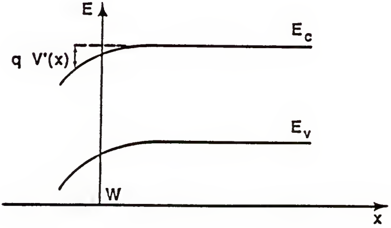

Fig. C.3 Band diagram near the base edge of the space charge region.

$$\delta n(W) \approx \exp(-eV_{bi}/kT)(J_n(W)/eD_n(W))\exp(eV_{bi}/kT)\delta x,$$

$$\delta n(W) \approx (J_n(W)\delta x/eD_n(W)), \qquad (C.5(a))$$

and the effective recombination velocity can be written as

$$S = D_n(W)/\delta x. \qquad (C.5(b))$$

We now prove that δx equals the extrinsic Debye length in base at $x = W$. We define the SCR edge of the base as the point where the space charge density is one-tenth of the net doping density. Let $V'(x)$ be the difference between the electrostatic potential at $x = W$ and that at any point in the bulk of the base (Fig. C.3). Since at $x = W$ the density of the majority holes is nine-tenths of the bulk value (the net doping density is assumed to vary negligibly within an extrinsic Debye length L_D in the quasi-neutral base) then $V'(W)$ will obey

$$0.9 = \exp(-eV'(W)/kT) \rightarrow V'(W) \approx 0.1\ kT/e, \qquad (C.6)$$

where nondegenerate statistics have been used. Since $V'(W)$ is very small it changes exponentially with distance for a few Debye lengths. Hence near $x = W$

$$V'(x)/V'(W) \approx \exp[-(x-W)/L_D] \qquad (C.7)$$

and the potential $V(x)$ as used in (C.2(b)) becomes

$$V(x) = V_{bi} - V'(x) = V_{bi} - V'(W)\exp[-(x-W)/L_D], \qquad (C.8)$$

in the vicinity of W. From (C.6) and (C.8), we write $\exp(eV(x)/kT)$ as

$$\exp(eV_{bi}/kT)[1 - \exp(-(x-W)/L_D)(eV'(W)/kT)] \approx$$

$$\exp(eV_{bi}/kT)[1 - 0.1\exp(-(x-W)/L_D)], \qquad (C.9)$$

near $x = W$. Therefore, $\exp(eV/(x)/kT)$ remains substantially constant over a Debye length at $x = W$. Consequently $\delta x \approx L_D$ and from (C.5(b) the boundary condition becomes

$$S \approx D_n/L_n. \qquad (C.10)$$

If the base was n-type having a Debye length L_D' then the recombination velocity for holes would become $S = D_p/L_D'$. Equation (C.10) holds also under reverse bias if $\delta n(W)$, as given by (C.5), is much higher than the equilibrium minority carrier density at $x = W$.

We now switch our attention to high injection. Under moderate or high injection the electric field in the base changes and causes the SCR barrier height to alter by an amount $\delta V_{bi} = V_{bi} - V_b$. Using the analysis presented in the low injection case, we can write (C.3) as

$$\delta n(W) = n(W) - n_o(W) = n_o(W)[\exp(e\delta V_{bi}/kT) - 1]$$

$$+ J_n(W)L_D/(eD_n), \qquad (C.11(a))$$

where $n_o(W)$ is the equilibrium electron density at $x = W$. In (C.11(a)) L_D is given, for Boltzmann statistics, by

$$L_D = \sqrt{[kT\epsilon/(p(W) + n(W))]} / e, \qquad (C.11(b))$$

where $p(W)$ and $n(W)$ are the hole and electron densities at the SCR edge of the base and e is the dielectric constant. Equation (C.11(b)) serves as an accurate nonlinear boundary condition for an illuminated short-circuited p/n junction solar cell for which the base is in moderate or high-level injection. It relates the hole and electron densities and the electron current density at the space-charge-region edge, $x = W$, through a variable, δV_{bi}, that accounts for all electric potential variations in the quasi-neutral base and for series resistance effects in the heavily doped emitter.

Returning now to low injection, equation (C.10) resembles the expression $S = D/W$ for a uniformly doped short-base region of thickness W, defined by the absence of bulk recombination and terminated by an ideal ohmic contact. For both (C.10) and for $S = D/W$, the excess minority-carrier density is forced to vanish within a short distance characteristic of the problem under study. In the case of the short base region, this distance W separates the injecting boundary from the ideal ohmic contact. In the case of (C.10), this distance L_D separates the space-charge-region edge of the quasi-neutral base from the high field part of the space-charge region. Equation (C.10) holds only if $D_n/L_D < S_{KL}$; otherwise $S = S_{KL}$.

Here we emphasize that, provided $D_n/L_D < S_{KL}$, the effective recombination velocity is not the kinetic-limit velocity. Rather it is determined by the rate at which the minority carriers diffuse toward the high-field region of the junction, a rate measured by the velocity D_n/L_D.

Equations (C.10) and (C.11) serve as a boundary condition for an illuminated solar cell. They also apply to the collector edge of quasi-neutral base of a transistor in the forward-active mode, provided the collector is in the low-current regime defined by $J/e \ll N_c V_{sat}$ which is the product of the collector doping and the saturated velocity.

If p is the majority-carrier density at the edge of the quasi-neutral base then, for Boltzmann statistics and low injection (C.10) becomes

$$S \approx eD_n\sqrt{[p/kT\epsilon]}, \qquad (C.12)$$

for electrons. A similar equation holds for holes in an n-type base. For moderately doped silicon, the value of S in (C.12) is about the same as the kinetic limit velocity S_{KL} for electrons, $S_{KL} \approx 5\text{x}10^6$ cm/s, or holes, $S_{KL} \approx 3\text{x}10^6$ cm/s, [61]. For doping densities higher than 10^{17} cm^{-3} the kinetic limit velocity imposes an upper bound on S. For light doping densities, $N_A \approx 10^{14}$ cm^{-3}, (C.12) yields a value six times less than S_{KL}. Also, at low temperatures the ratio $S/S_{KL} \ll 1$ since S_{KL} and D decrease according to power laws while deionization causes the majority hole density to decrease exponentially with temperature.

We now investigate the effect that a finite value of S has on the short-circuit current of a solar cell. The excess minority-carrier density at the space-charge region edge of the quasi-neutral base is $\delta n = I_{SC}/eS$. This particle accumulation forces a component of current to flow in a direction opposite to that of the photocurrent,

$$\delta I = I_{oB}\delta n/n_o = I_{oB}I_{SC}/(eSn_o), \qquad (C.13)$$

where I_{oB} is the saturation value of the base recombination current.

Let I_{SC}' be the short-circuit current of the same cell when $S = \infty$. Low injection implies linearity and the superposition principle allows I_{SC}' to be expressed as

$$I_{SC}' = I_{SC} + \delta I = I_{SC}\,[1 + I_{oB}/(eSn_o)]. \qquad (C.14)$$

Therefore, the fractional loss in short-circuit current arising from the finite value of S is

$$I_{oB}/(eSn_o) = (I_{oB}/en_i^2)N(W)/S, \qquad (C.15)$$

where N(W) is the doping density at the space-charge region edge of the quasi-neutral base.

In present silicon solar cells the ratio I_{oB}/en_i^2 is at least 10^{-13} cm^4/s. Thus, even if N(W) becomes 5×10^{17} cm^{-3} equation (C.15) indicates that the relative current loss of no more than 1%. Similar results hold for GaAs solar cells. Consequently, the implicit assumption of infinite S that was used in Chapters 1-4 is a realistic one.

Using the formula $\delta n/n_o = I_{SC}N(W)/(eSn_i^2)$ and realistic values for I_{SC} and N(W), then for silicon under one-sun illumination and short-circuit conditions the separation of the quasi-Fermi potentials at the space-charge-region edge of the base is about 0.44 V ≈ 17 kT/e at T = 300 K. For a GaAs cell this separation is about 0.7 V ≈ 27 kT/e. It is likely, therefore, that the recombination in the space-charge region will be more important than the back injection into the base especially at low temperatures. Thus, the effect discussed could appreciably decrease the short-circuit current of polycrystalline silicon, GaAs or other solar cells having a large density of recombination centers in the junction region.

REFERENCES

1. C. Donolato, Appl. Phys. Lett., 46, 270 (1985).

2. W. Shockley, M. Sparks, and G.K. Teal, Phys. Rev., 83, 151 (1951).

3. H. J. De Man, M.Y.Ghannam, and R.P.Mertens, IEEE Trans. Electron Devices, ED-31, 1720 (1984).

4. J. A. del Alamo and R. M. Swanson, IEEE Trans. Electron Devices, ED-31, 1878 (1984).

5. J. Pietzsch, Solid State Electron., 25, 295 (1982).

6. J. Dziewior and W. Schmid, Appl. Phys. Lett., 31, 346 (1977).

7. D. E. Ioannou and R. J. Gledhill, J. Appl Phys., 56, 1797 (1984).

8. M. S. Tyagi, J.F. Nijs, and R.J. Van Overstaeten, Solid State Electron., 25, 411 (1982).

9. H. Holloway and A.D. Brailsford, J. Appl. Phys., 55, 446 (1984).

10. L. M. Sander, J. Appl. Phys., 57, 2057 (1984).

11. M. D. Lammert and R. J. Schwartz, IEEE Trans. Electron Devices, ED-24, 377 (1977).

12. J. G. Fossum, A. Neugroschel, and F. A. Lindholm, Solid State Electron., 23 1127 (1980).

13. R.M. Swanson, S.K. Beckwith, R.A. Crane, W.D. Eades, Y. H. Kwark, R. A. Sinton, and S.E. Swirhun, IEEE Trans. Electron Devices, ED-31, 661 (1984).

14. H. Holloway and A. D. Brailsford, J. Appl. Phys., 54, 4641 (1983).

15. W. Shockley and H. J. Queisser, J. Appl. Phys., 32, 510 (1961).

16. C. H. Henry, J. Appl. Phys., 51, 449 (1980).

17. P. Baruch, J. Appl. Phys., 57, 1347 (1985).

18. T. Tiedje, E. Yablonovitch, G. D. Cody and B. G. Brooks, IEEE Trans. Electron Devices, ED-31, 711 (1984).

19. D. A. Bowler and M. Wolf, IEEE Trans. Electron Devices, 31, 1878 (1984).

20. K. G. Svantesson and N. G. Nillson, Solid State Electron.,21, 1603 (1978).

21. J. A. del Alamo, S. Swirhun, and R.M. Swanson, Solid State Electron., 28, 47 (1985).

22. E. L. Ince, Ordinary Differential Equations, Dover Publications, New York (1956).

23. A. Rohatgi and P. Rai-Choudhury, IEEE Trans. Electron Devices, 31, 569 (1984).

24. J. A. del Alamo and R. M. Swanson, Proc. 17th IEEE Photovoltaic Specialist Conf., New York (1984).

25. M. A. Shibib, F. A. Lindholm, and F. Therez, IEEE Trans. Electron Devices, 26, 959 (1979).

26. J. S. Park, A. Neugroschel and F. A. Lindholm, IEEE Trans. Electron Devices, 33, 240 (1986).

27. H. J. Hovel, Solar Cells, 11, Semiconductors and Semimetals Series, Academic Press, New York (1975).

28. M.A. Green, Z. Jianhua, A. W. Blakers, M. Taouk, and S. Narayanan, IEEE Electron Dev. Lett., EDL-7, 567 (1986).

29. R. A. Sinton, Y. Kwark, J. Y. Gan, and R. M. Swanson, IEEE Electron Dev. Lett., EDL-7, 567 (1986).

30. C. T. Sah, Tech. Rep., DOE/JPL-956289-84-1, JPL (1984).

31. V. E. Lowe and A. C. Day, IEEE Trans. Electron Devices, 31, 626 (1984).

32. A. Neugroschel, M. Arienzo, Y. Komen and R. D. Isaac, IEEE Trans. Electron Devices, 32, 807 (1985).

33. M. A. Green, A. W. Blakers, J. Shi, E. M. Keller and S. R. Wenham, IEEE Trans. Electron Devices, 31, 679 (1984).

34. E.S. Rittner, A. Meulenberg and J. F. Allison, J.Energy, 5,9 (1984).

35. A. Rohatgi, T. W. O'Keefe and D. L. Meier, Final Report, XB-3-02090-4, SERI, Golden Colo., (1984).

36. P. T. Landsberg and G. S. Kousik, J. Appl. Phys., 56, 1696 (1984).

37. T. W. Jung, F. A. Lindholm, and A. Neugroschel, IEEE Trans. Electron Devices, ED-31, 588, (1984).

38. B. H. Rose, IEEE Trans. Electron Devices, ED-31, 559, (1984).

39. W. R. Thurber, R. L. Mattis, Y. M. Liu, and J. J. Filliben, J. Elecrochem. Soc., 127, 1807, (1980).

40. J. Dziewior and D. Silber, Appl. Phys. Lett., 42, 170 (1979).

41. A. Neugroschel, IEEE Electron Device Lett., EDL-6, 425 (1985).

42. M. Hack and M. Shur, J. Appl. Phys., 58, 997 (1985).

43. A. E. Delahoy and R. W. Griffith, J. Appl. Phys., 52, 6337 (1981).

44. R. S. Crandall, J. Appl. Phys., 53, 3350 (1980).

45. H. Okamoto, H. Kida, S. Nonomura and Y. Hamakawa, Solar Cells, 8, 317 (1983).

46. P. Sichanugrist, M. Konagai and K. Takahashi, J. Appl. Phys., 55, 1155 (1984).

47. D. J. Staebler, J. Non-Crystalline Solids, 35-36, 386 (1980).

48. R. W. Crandall, R. Williams and B. E. Tompikn, J. Appl. Phys., 50, 5506 (1979).

49. V. Dalal and F. Alvarez, J. de Physique, 42, C4, 491 (1981).

50. G. A. Swartz, J. Appl. Phys., 53, 712 (1983).

51. C. Manfredotti and M. Mussatti, J. Non-Crystalline Solids, 59-60, 1163 (1983).

52. R. J. Schwartz, J. L. Gray, G. B. Turner, D. Kanani and H. Ullal, Proceedings of the 17th IEEE Photovoltaic Specialist Conference, New York (1984).

53. I. Chen and S. Lee, J. Appl. Phys., 53, 1045 (1982).

54. J. R. Haynes and W. Shockley, Phys. Rev , 81, 835 (1951).

55. T. Tiedje, Semiconductors and Semimetals, Academic Press, Ch. 6, 21, Part C, New York (1984).

56. N. F. Mott, Adv. Phys., 16, 49, (1967).

57. D. Emin, Phus. Today, 35, 34 (1982).

58. D. Adler, Solar Energy Mat., 8, 53, (1982).

59. E. Spenke, Electronic Semiconductors, McGraw-Hill, New York (1958).

60. S. M. Sze, Physics of Semiconductor Devices, Wiley, New York (1981).

BIOGRAPHICAL SKETCH

Konstantinos Misiakos was born in Kalamata, Greece, on January 1, 1956. He received the B.S. degree in Electrical Engineering from the National Technical University of Athens in November 1978 and the M.S. degree in Electrical Engineering from Clemson University, Clemson, South Carolina, in May 1984. Since August 1984 he has been working toward the Ph.D. degree in Electrical Engineering at the University of Florida, Gainesville, Florida.

From January 1983 to May 1984 he was a research assistant in the solar cell reliability laboratory at Clemson University. His research at the University of Florida is on the modeling of solar cells and characterization of bipolar devices.

I certify that I have read this study and that in my opinion it conforms to acceptable standards of scholarly presentation and is fully adequate, in scope and quality, as a dissertation for the degree of Doctor of Philosophy.

Fred Lindholm

Fredrik A. Lindholm, Chairman
Professor of Electrical Engineering

I certify that I have read this study and that in my opinion it conforms to acceptable standards of scholarly presentation and is fully adequate, in scope and quality, as a dissertation for the degree of Doctor of Philosophy.

Arnost Neugroschel

Arnost Neugroschel, Cochairman
Professor of Electrical Engineering

I certify that I have read this study and that in my opinion it conforms to acceptable standards of scholarly presentation and is fully adequate, in scope and quality, as a dissertation for the degree of Doctor of Philosophy.

Peter T. Landsberg

Peter T. Landsberg
Graduate Research Professor of
Electrical Engineering

I certify that I have read this study and that in my opinion it conforms to acceptable standards of scholarly presentation and is fully adequate, in scope and quality, as a dissertation for the degree of Doctor of Philosophy.

Sheng San Li

Sheng S. Li
Professor of Electrical Engineering

I certify that I have read this study and that in my opinion it conforms to acceptable standards of scholarly presentation and is fully adequate, in scope and quality, as a dissertation for the degree of Doctor of Philosophy.

Samuel B. Trickey

Samuel B. Trickey
Professor of Physics

This dissertation was submitted to the Graduate Faculty of the College of Engineering and to the Graduate School and was accepted as partial fulfillment of the requirements for the degree of Doctor of Philosophy.

August 1987

Herbert A. Bevis

Dean, College of Engineering

Dean, Graduate School